CHEMISTRY OF MATERIALS

pubs.acs.org/cm

Review

Metastable Group IV Allotropes and Solid Solutions: Nanoparticles and Nanowires

Sven Barth,* Michael S. Seifner, and Stephen Maldonado

Cite This: *Chem. Mater.* 2020, 32, 2703−2741

Read Online

ACCESS | Metrics & More | Article Recommendations | Supporting Information

ABSTRACT: In the past decades, group IV nanowires and nanoparticles have been the subject of extensive research. Beside tremendous progress in morphological control and integration in advanced device architectures, research on allotropes and metastable compositions has gained considerable interest. Several new approaches now allow the controlled formation of specific allotropes in the nanostructured form as well as chemical compositions not attainable by traditional synthesis protocols. The conditions applied to form these metastable solid solutions and allotropes are usually far from thermodynamic equilibrium or rely on unconventional templates. The increased interest in the field of metastable group IV nanostructures arises from their altered physical properties, including tunable, direct bandgaps with energies equivalent to the near- to mid-infrared spectral region as described for materials such as $Ge_{1-x}Sn_x$ and hexagonal $Si_{1-x}Ge_x$. The implementation of these material characteristics in complementary metal oxide semiconductor (CMOS) processes are desirable for applications in electronics, optoelectronics, sensors, optics, etc. but also their use as nonsurface bound nanoparticles in sensing, nanobiotechnology and nanomedicine can offer additional opportunities. This review article highlights both the important advancements and still open questions for the continued development of these nanoscaled materials for next-generation device concepts.

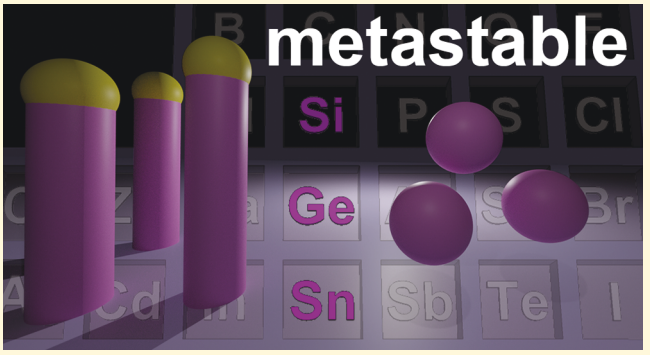

1. INTRODUCTION

Group IV elements, especially carbon and silicon, are essential for society and modern standards of life. Many present-day consumables and devices would not be possible without the science and technology based on group IV elements. Besides desirable properties, their natural abundance is an important factor from a future-oriented perspective. However, even in pure elemental forms, group IV allotropes require further understanding to exploit their full potential.

Carbon is a widely investigated group IV element with a large number of allotropes. The unique physical properties of the allotropes result in a wide range of applications including electronics, optoelectronics, photovoltaics, sensing, energy conversion, energy storage, *etc.*[1−3] The layered structure of graphite represents the thermodynamically most stable modification of carbon at standard temperature and pressure (*STP*). Graphite is a semimetal with anisotropic conductivity due to delocalization of electrons across the plane of carbon sheets. In contrast, the diamond cubic (*dc*) carbon allotrope is an insulator with a bandgap of 5.47 eV. Although diamond is slightly less stable than graphite by ∼2 kJ·mol^{-1}[4] a large high kinetic barrier prevents interconversion of diamond into graphite at *STP*. Diamond is the paragon for a metastable phase that is kinetically stable at ambient conditions. Another metastable carbon allotrope is lonsdaleite, which has a diamond hexagonal (*dh*) crystal structure and can only be obtained under extreme reaction conditions.[5] Allotropes of carbon in the nanometer regime include fullerenes,[6,7] carbon nanotubes,[8,9] graphene,[10−12] graphyne,[13−15] graphdiyne,[14−16] nanodiamonds,[17,18] molecular polyyne rings,[19] *etc.* and are actively considered for a wide range of applications. Since the field of nanoscale carbon allotropes is quite mature and diverse we refer to recent reviews summarizing the state-of-the-art of research on this topic.[1−3,6−10,12,14,15]

This text excludes carbon for the reasons stated above and lead, the heaviest group IV element. No metastable allotrope or solid solution containing lead has been observed at the nanoscale. This text instead highlights advances in realizing unusual crystal phases and properties of nanoscaled silicon, germanium, tin, and their binary solid solutions. Specifically, dimensionally confined morphologies such as nanoparticles (NPs) and nanowires (NWs) of structurally metastable phases

Received: October 30, 2019
Revised: March 16, 2020
Published: March 16, 2020

as well as unusual, metastable compositions are in the focus. For binary systems, only materials where element concentrations exceed the maximum solid solubility and metastable polymorphs are discussed. This text documents and details hyperdoped group IV materials. Hyperdoping results in metastable solid solutions but the content of the solute in the solvent matrix is limited. For clarity, the term "hyperdoping" refers to incorporation of solute in the range of <5% without the formation of a new crystal phase. Hyperdoping also requires that the solute atoms possess a significant activity. That is, physical properties of the base material are altered by hyperdoping. Hence, hyperdoped materials are also metastable solid solutions, but the content of the solute in the solvent matrix is limited. Planar thin films as well as two-dimensional allotropes are not accounted for in this review due to the abundance of reviews focusing on these specific morphologies.[20−24] Moreover, ion implantation is not considered due to the inherent concentration gradient of elements typically observed during implantation and thus inhomogeneous composition within the individual nanostructures.[25]

The experimental conditions for NW or NP synthesis of metastable materials often require extreme or delicate growth conditions and sometimes structure directing templates. Thus, a detailed discussion is required to illustrate the specific conditions for their formation and the altered physical properties. The most intriguing changes in the materials properties are related to semiconductor−metal transitions associated with an increased number of charge carriers, alteration of the electronic band structure and structural as well as compositional changes leading to the formation of low bandgap direct semiconductor behavior. Therefore, further introduction of the known allotropes and important binary solid solutions is provided *vide infra*.

1.1. Silicon Allotropes. Si is the next lightest homologue of carbon. The thermodynamically most stable allotrope of Si at *STP* possesses the *dc* lattice structure. The *dc*-Si is an indirect bandgap semiconductor with a bandgap energy of 1.12 eV and can possess an electron mobility of 1400 $cm^2 \cdot V^{-1} \cdot s^{-1}$ and a hole mobility of 450 $cm^2 \cdot V^{-1} \cdot s^{-1}$.[26] Nowadays, the overwhelming majority of fabrication processes in the semiconductor industry are designed for *dc*-Si, and thus implementation of new materials should be compatible with technologies based on it. Specifically, complementary metal−oxide−semiconductor (CMOS) technology is the dominant device structure and relies heavily on *dc*-Si.

The synthesis of various Si allotropes has proven to be very challenging. Despite demanding synthesis protocols, allotropes of Si can be accessed using high-pressure conditions,[27−44] kinetically controlled synthesis,[45−47] precursors with preformed Si networks,[48−51] and templates.[52−61]

In this context, high-pressure synthesis using diamond anvil cells is a conventional method to form metastable phases including a high number of Si allotropes.[27−29] The *dc*-Si (3*C*, space group $Fd\bar{3}m$, Si-I) phase is the most stable allotrope at *STP*, but at pressures up to 250 GPa (*β-Sn*)-Si (*β*-Sn structure, space group $I4_1/amd$, Si-II),[62−65] *sh*-Si (simple hexagonal, space group $P6/mmm$, Si-V),[63−65] *hcp*-Si (hexagonal close packed, space group $P6_3/mmc$, Si-VII),[63,66] *fcc*-Si (face-centered cubic, space group $Fm\bar{3}m$, Si-X)[67] and *Imma*-Si (body-centered orthorhombic, space group *Imma*, Si-XI)[65,68] can be obtained.[29] While the transformation upon pressure variation is generally reversible for metals, the decompression of (*β-Sn*)-Si leads to additional metastable phases including *bc8*-Si (body-centered cubic, space group $Ia\bar{3}$, Si-III),[30,69,70] *dh*-Si (lonsdaleite structure, typically 2H-Si, space group $P6_3/mmc$, or Si-IV),[30,71] Si-VIII (tetragonal, space group $P4_12_12$),[31,72] Si-IX (tetragonal, space group $P4_22$),[31] and *r8*-Si (rhombohedral/trigonal, space group $R\bar{3}$, Si-XII).[31,72] Among these phases, only *bc8*-Si and *dh*-Si can be stabilized at ambient conditions. Accordingly, these two phases are potential candidates for device applications.[71] In general, *dh*-Si is simply being considered as a structural analogue of lonsdaleite with the 2H polytype structure, thus also referred to 2H-Si. For *dh*-Si the differences in the sequence of the layers can result in 2H (AB), 4H (ABCB), and 6H (ABCACB) polytypes of Si, which have been predicted by theoretical calculations.[73−75] Recent results demonstrate that the high pressure synthesis of the lonsdaleite phase can also result in the 4H polytype.[76]

Nonequilibrium reaction conditions can also be obtained via shock waves induced by femtosecond lasers. This tactic has yielded new Si allotropes including *bt8*-Si (body-centered tetragonal, space group $I4_1/a$) and *st12*-Si (body-centered tetragonal, space group $P4_32_12$).[47] Another nonequilibrium based method to synthesize metastable Si allotropes is the use of high-energetic Si-containing precursor compounds. A topochemical approach of removing metals from silicide precursors can be used to obtain metastable phases such as *allo*-Si.[48] Among silicides, a large variety of Si clathrates are predicted to be suitable starting compounds[77] but to date only a small number of Si allotropes have been synthesized from Zintl salts.[49−51]

Additionally, silicene, the Si analogue of graphene, has been synthesized via the epitaxial growth on various surfaces including Ag(111),[52−56] Ag(110),[57,58] Au(110),[59] Ir(111),[60] and ZrB_2[61] showing high potential in tuning electronic states by chemical functionalization.[20,78] Detailed overviews concerning the realization of different Si allotropes have been published in recent literature.[20,79−81]

1.2. Germanium Allotropes. The third lightest group IV element is Ge. The assortment of Ge allotropes mirrors the case of Si; e.g., the thermodynamically favored allotrope is diamond cubic at *STP* and it is also an indirect semiconductor. The semiconductor industry is based on *dc*-Si predominantly because the chemistry of its oxide is more favorable than the corresponding oxide on *dc*-Ge. Nevertheless, *dc*-Ge has some significant advantages. *dc*-Ge has higher ceilings on the attainable electron and hole mobilities of 3900 and 1900 $cm^2 \cdot V^{-1} \cdot s^{-1}$, respectively, and the indirect bandgap energy of the L-point (0.66 eV) is only 140 meV smaller than the direct at the Γ-point.[26]

In addition to *dc*-Ge (*α*-Ge, diamond cubic, 3*C*, space group $Fd\bar{3}m$, Ge-I), several high-pressure allotropes of Ge are known and can be realized via compression and and subsequent decompression of *dc*-Ge.[64,82,83] Compression with pressures up to 190 GPa results in (*β-Sn*)-Ge (*β*-Sn structure, space group $I4_1/amd$, Ge-II),[64] *Imma*-Ge (body-centered orthorhombic, space group *Imma*),[82] *sh*-Ge (simple hexagonal, space group $P6/mmm$),[82,84] *Cmca*-Ge (base-centered orthorhombic, space group *Cmca*),[83] and *hcp*-Ge (hexagonal close packed, space group $P6_3/mmc$).[83] After decompression, the (*β-Sn*)-Ge either yields *st12*-Ge (simple tetragonal, space group $P4_32_12$, Ge-III)[64] or *bc8*-Ge (body-centered cubic, space group $Ia\bar{3}$, Ge-IV).[72]

Furthermore, *allo*-Ge[85−87] and (nearly) guest-free clathrates of Ge[88−90] have been synthesized using germanides as high-energetic precursor compounds. Microcrystalline *allo*-Ge

https://dx.doi.org/10.1021/acs.chemmater.9b04471
Chem. Mater. 2020, 32, 2703−2741

prepared by topotactic deintercalation can be converted to 4H-Ge (Ge-V) via subsequent annealing.[85−87]

Germanene, the atomically thin Ge analogue of graphene, has recently been prepared on Au(111),[21] Pt(111),[91] Al(111),[92] and hexagonal-AlN,[93] as well as MoS_2,[94] and demonstrates a buckled structure like silicene.[95]

1.3. Tin Allotropes. Sn is the heaviest group IV element considered in this review. The thermodynamically most stable allotrope at *STP* is β-Sn (β-Sn structure, tetragonal, space group $I4_1/amd$, Sn-I). However, below approximately 13 °C and atmospheric pressure α-Sn (diamond cubic, space group $Fd\bar{3}m$, Sn-II) is thermodynamically favored.[96] With the change in crystal structure, the physical properties change from metallic β-Sn to α-Sn being a semimetal due to its inverted bands separated by a bandgap.[97,98] The transition of α-Sn to β-Sn is accompanied by a decrease in volume; thus, the transition can also be initiated at lower temperatures by applying pressure.[99−101] Interestingly, the total energies of α-Sn and β-Sn are very similar over a wide temperature range, and the $\alpha-\beta$ transition is driven by the more rapidly increasing entropy term for the β-Sn allotrope caused by a softer average phonon mode of β-Sn.[102−104] The appearance/formation of the α-Sn phase beyond 13 °C strongly depends on crystal growth kinetics but also on thermodynamic influences have to be considered. The small Gibbs free energy difference between the α- and the β-phase (see Supporting Information) can be overcompensated by slight alterations of the conditions (e.g., pressure, template, doping, alloying, particle size, *etc.*) leading to a favored formation of the α-Sn phase. Furthermore, high-pressure phases of Sn are known and can be realized in a diamond anvil cell.[27−29] At approximately 9.2 GPa β-Sn transforms into *bct*-Sn (body-centered tetragonal, space group $I4/mmm$, Sn-III)[105] which converts into a *bcc*-Sn (body-centered cubic, space group $Im\bar{3}m$, Sn-IV)[106] at pressures between 40 and 50 GPa.[28]

Finally, stanene is the Sn version of graphene. Stanene has been prepared via the epitaxial growth on Bi_2Te_3(111),[107] Cu(111),[108] Ag(111),[109] and Au(111)[110] surfaces.

1.4. Binary Group IV Solid Solutions. The most prominent representatives of group IV alloys are $Ge_{1-x}Si_x$, $Ge_{1-x}Sn_x$, and $Ge_{1-x-y}Si_xSn_y$, which all crystallize in the *dc* crystal structure. All these solid solutions/alloys are isostructural with Si and thus compatible with CMOS processing. While the Si−Ge system reveals miscibility over the whole composition range,[111] the Ge−Sn binary phase diagram shows phase separation with a maximum solid solubility of approximately 1 atom % Sn in *dc*-Ge.[112] Similarly, the Si−Sn phase diagram contains a miscibility gap.[113] Therefore, the ternary group IV compound $Ge_{1-x-y}Si_xSn_y$ reveals only a small composition range where separation can be prevented.

The physical properties of *dc*-Si and *dc*-Ge can be altered by alloying. However, there are significant challenges that have to be overcome to achieve good to excellent crystal quality. High-quality Ge can be epitaxially grown on a Si substrate; however, due to the large lattice mismatch of approximately 4.2%[114] a $Ge_{1-x}Si_x$ buffer layer can be used to avoid an accumulation of defects and strain resulting in high quality Ge films.[115−118] In this respect, epitaxial Ge films on Si with low defect concentration have also been obtained by other approaches such as sequential growth strategies using different temperature profiles for the growth of individual Ge layers combined with specific annealing protocols.[119,120] In addition, $Ge_{1-x}Si_x$ alloys show distinct differences in carrier mobilities, bandgap energies, *etc.* dependent on their composition and are widely investigated for electronic and optoelectronic purposes[121] by either directly using $Ge_{1-x}Si_x$ as active material[122,123] or as buffer layer to implement high-quality Ge layers on a Si substrate.[124] Furthermore, $Ge_{1-x}Si_x$ can be used as a buffer layer acting as a substrate to grow a pseudomorphic film of tensile-strained Si.[125,126] The tensile strain in the Si layer leads to an increased carrier mobility for both electrons and holes which is caused by breaking the degeneracy of the valence bands and other effects.[127−129] These altered physical properties are key to performance enhancements of devices, and therefore this technology has been adopted by the semiconductor industry.[130,131]

The most dramatic changes are observed for alloying the *dc* allotropes of Si as well as Ge with Sn. In their pure form *dc*-Si and *dc*-Ge are indirect bandgap semiconductors and thus limited in optoelectronic devices. In contrast to direct bandgap semiconductors, radiative electron−hole recombination is very inefficient for indirect bandgap semiconductors due to the necessity of momentum change required for a photon emission (Figure 1a,b).[132] However, $Ge_{1-x}Sn_x$ and the ternary $Ge_{1-x-y}Si_xSn_y$ alloys are of great interest due to their direct bandgap energy in the near- to mid-IR range, when the incorporation of Sn exceeds the thermodynamic solid solubility by a large margin.[219] The incorporation of Sn in a Ge crystal lattice leads to changes in the band structure of the material causing the Γ-bandgap energy to decrease more significantly than the L-gap, which is illustrated in Figure 1c,d, showing the electronic band structure for different $Ge_{1-x}Sn_x$ compositions.[133] For pure *dc*-Ge and low concentrations of Sn in $Ge_{0.95}Sn_{0.05}$, the materials show an indirect bandgap with $E_{g\Gamma} > E_{gL}$ (Figure 1c). However, higher Sn content leads to an inversion of the effective energy gap values. Figure 1d illustrates this premise for $Ge_{0.85}Sn_{0.15}$ with $E_{g\Gamma} < E_{gL}$ being a direct bandgap semiconductor. The transition into a direct bandgap is observed for relaxed $Ge_{1-x}Sn_x$ thin films with a Sn content in the range of ∼8.5−11 atom % located at substitutional sites of the Ge host lattice (Figure 2a).[134−138] Thus, a significant increase in photoluminescence (PL) intensity can be observed when the Sn threshold in the metastable $Ge_{1-x}Sn_x$ is reached (Figure 2b). The direct transition recorded in the PL spectra thus shifts toward lower energies with increasing Sn content in $Ge_{1-x}Sn_x$ due to further decrease of the composition dependent bandgap energy (Figure 2b). Moreover, strain engineering of group IV semiconductors is part of the used methodology to tailor their physical properties.[139] Specifically the influence of compressive strain on the band structure of the here discussed $Ge_{1-x}Sn_x$ should be considered because Si as well as Ge possess significantly smaller lattice constants. Compressive strain leads to the opposing effect as the Sn incorporation on the electronic band structure, which means that higher compressive strain causes increased bandgap values for a given Sn concentration and can lead to the necessity of higher Sn contents for the indirect−direct transition.[140] In addition, applying strain causes the degenerate valence band at Γ to split, and the compressive strain shifts the heavy holes up in energy (vice versa, tensile strain shifts the light holes up in energy) which can be also visible in the emission spectra when the emission shows split signals.[141] Similarly, theoretical predictions indicate the indirect−direct bandgap semiconductor transition for relaxed $Ge_{1-x-y}Si_xSn_y$ alloys is reached when $y > 1.364x + 0.107$.[142] In general, the synthesis of these materials

https://dx.doi.org/10.1021/acs.chemmater.9b04471
Chem. Mater. 2020, 32, 2703−2741

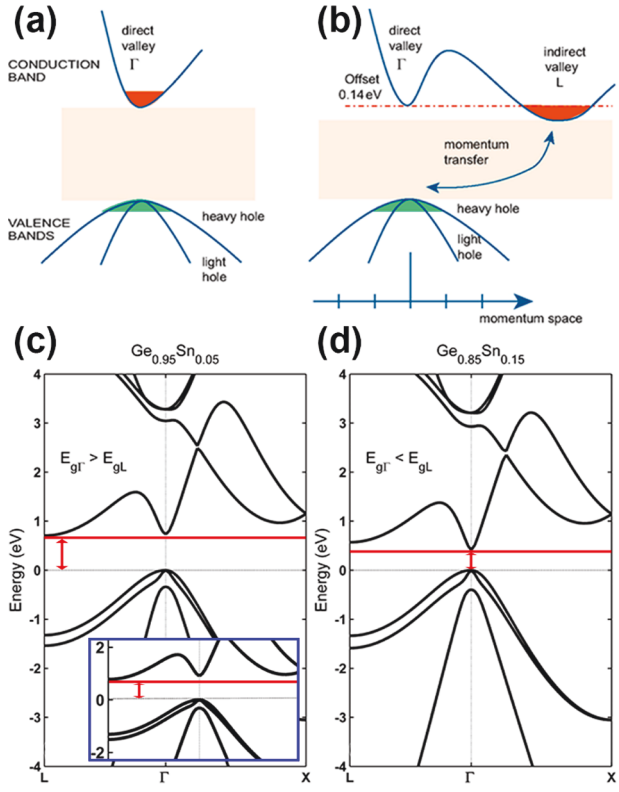

Figure 1. (a) In a direct bandgap semiconductor, the electron−hole recombination occurs in the Γ-point.[132] (b) Electrons occupy the states in the L-valley of the conduction band in an indirect bandgap semiconductor and thus require a change of momentum for radiative electron−hole recombination.[132] Reprinted from ref 132 by Geiger et al., licensed under CC BY 4.0 (https://creativecommons.org/licenses/by/4.0/). Published 2015 by Frontiers Media SA. The electronic band structures of (c) $Ge_{0.95}Sn_{0.05}$ and (d) $Ge_{0.85}Sn_{0.15}$ reveal significant alteration of the direct bandgap energy upon alloying Ge with Sn with a transition from indirect (c) to direct (d) bandgap material. The inset in (c) represents the electronic band structure of pure *dc*-Ge and reveals the energy difference between Γ- and L-valley minima.[133] The red lines have been added to guide the eye, and the inset is added from another image of the same reference. Adapted from ref 133 with the permission. Copyright 2013 AIP Publishing.

requires kinetically controlled growth processes to overcome the thermodynamic limits of solid solubility. The challenges associated with precisely controlling synthetic conditions and crystal quality are most likely reasons for slow progress over three and a half decades between the theoretical prediction of materials properties[143] and the first report on the micrometer scale[144] and the realization of optically pumped lasing from $Ge_{1-x}Sn_x$ being achieved.[145] In addition to potential optical applications, a strong increase in carrier mobilities can be expected for $Ge_{1-x}Sn_x$ high-speed electronics.[24,146−149] The altered physical properties make this material a very promising candidate for optoelectronics and optical devices operating in the infrared spectral region, such as lasers (Figure 2b),[145,150−152] photodetectors,[153,154] light emitting diodes,[155−157] or biological sensors.[158] Thin film growth of $Ge_{1-x}Sn_x$ by different strategies has been demonstrated on single crystals[134,159,160] as well as amorphous insulators,[161] with the most popular being epitaxial growth on group IV substrates.[22]

Theoretically, the incorporation of approximately 3.4 atom % Pb in Ge would be required for an indirect-direct semiconductor transition,[162] but is even harder to achieve due to the large difference in atomic radii.[163] Similarly, a transition of Si to a direct bandgap semiconductor material upon alloying with Sn has been predicted,[164,165] while different theoretical approaches exclude the presence of such a transition.[165] Experimentally, significant Sn incorporation in Si has been described and will be discussed below, but a transition to a direct bandgap material has not been observed.[166−171]

1.5. Nanostructure Synthesis. Control over the material's morphology is a highly desirable synthetic goal. Scaling down the dimensions of a material to the nanometer regime can result in very high surface-to-volume ratios. Therefore, surface effects are highly pronounced in these structures making them prime building blocks for applications in, e.g., catalysis and sensing.[172] Moreover, downscaling their size below their respective Bohr exciton radius leads to quantum confinement effects, which may lead to further new functionality and novel device concepts.[173,174] In this section we will briefly describe fundamental but simplified models for the formation of NPs and NWs.

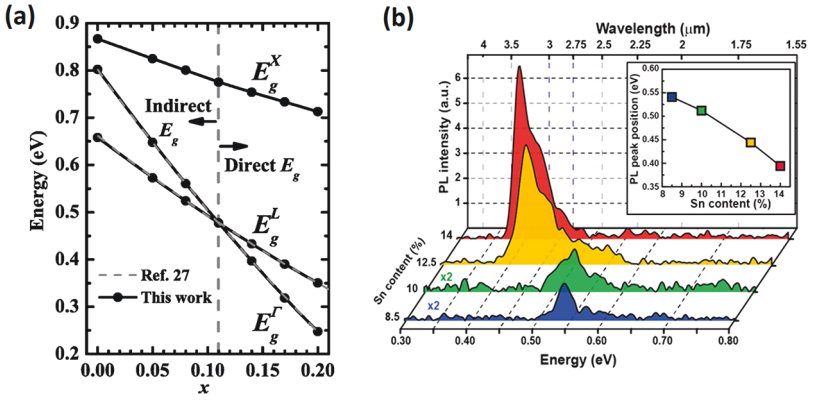

Figure 2. (a) Calculated bandgap energies of X, L, and Γ-point for various Sn compositions in $Ge_{1-x}Sn_x$. The bandgap energies of L and Γ-point agree with experimental data. According to this study an indirect to direct bandgap material transition is expected for Sn contents of 11 atom %.[137] Reprinted from ref 137 with permission. Copyright 2012 AIP Publishing. Room temperature photoluminescence (PL) spectra for thick $Ge_{1-x}Sn_x$ layers (750−1000 nm) with Sn contents between 8.5 and 14 atom % Sn. The inset illustrates the room temperature PL peak positions showing a shift toward smaller energies with increasing Sn content.[141] Reprinted with permission from ref 141. Copyright 2015 American Chemical Society.

https://dx.doi.org/10.1021/acs.chemmater.9b04471
Chem. Mater. 2020, 32, 2703−2741

1.5.1. Nucleation Theory for Particle Formation. The crucial steps for the formation of a crystal can be divided into nucleation and crystal growth. In classical nucleation theory, the initial formation of a nucleus is described via thermodynamics and reaction kinetics. For a cluster or nucleus to separate/form, there must be a driving force for the formation of a new thermodynamic phase. Initially, a solute must be supersaturated, i.e., dissolved at a level beyond the thermodynamic solubility, to initiate the formation of a new "solid" phase according to classical nucleation process. The nucleus is stable when the decrease in free energy that results from forming the new phase offsets the increased interfacial free energies at the phase boundaries with the solution. Since both effects are competing, stable nuclei only form above a critical size, which defines the free energy barrier for nucleation, for the supersaturation of the system. The maximum of the red curve highlighted in Figure 3 is the total free energy barrier and

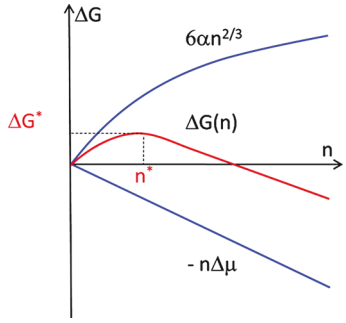

Figure 3. Critical thermodynamic effects observed during crystal growth allow the determination of a critical number of atoms forming the nucleus n*. Stable nuclei are observed beyond this threshold. The Gibbs free energy ΔG is plotted versus the number of atoms of the particle n whereby the supersaturation of the solution $\Delta\mu$ and the surface free energy α are important parameters. The critical Gibbs free energy ΔG^* equals the energy barrier which has to be overcome for the formation of a stable nucleus and is an important parameter for kinetic considerations.[176] Reprinted with permission from ref 176. Copyright 2010 American Chemical Society.

an important parameter for the crystal nucleation. Furthermore, the rate of nucleation also depends on the density of species in the solution or gas phase, the rate of the attachment of species/monomers to the nucleus, *etc.*[175−177] Once a stable nucleus is formed, supersaturation, which is equal to a higher chemical potential of the species in the vapor/liquid phase than in the solid, enables the growth of the stable nuclei in the crystallization step.[178−182] This simple model can describe some nucleation processes quite well but with limitations as demonstrated for alloy crystal formation[183] or nucleation of hydrocarbon droplets.[184]

Nonclassical descriptions for the initial stages of crystal growth have also been proposed. The prenucleation cluster pathway is a viewpoint not based on critical nucleus sizes but rather on dynamics. Besides thermodynamic considerations, this model argues kinetics play a major role and that dynamic processes enable the reorganization of the preformed clusters. A detailed discussion on nonclassical nucleation can be found in the literature.[185,186] The potential involvement of ionic cluster compounds with low molecularity was already mentioned by LaMer[187] before recently the actual description has been published.[188] In addition, a recent review on the often referenced LaMer model is highly recommended highlighting the shortcomings and well thought out ideas for the formation of monodisperse particle systems, but also referring to state-of-the-art models for crystal growth.[189] The shape control of nanoparticles is generally important and has been reviewed for several elements and compounds.[190−192] However, alterations concerning the surface energies at specific synthesis conditions[193] and preferential adsorption of surfactants are much less pronounced for the synthesis of group IV elements and alloys resulting in spherical or pseudospherical morphology. Only a small number of reports exist on shape-controlled synthesis protocols for tetrahedral,[194,195] cubic,[196−198] and cuboctahedral[199] group IV NPs, and often large particle dimensions of ∼100 nm can be encountered in these studies.

1.5.2. Metal-Assisted Nanowire Growth. NWs are representatives of quasi-one-dimensional structures with just one dimension exceeding the nanometer regime.[200−205] Among the vast number of different material compositions, group IV NWs are interesting building blocks for many technologies including electronics,[206] optoelectronics,[207,208] sensors,[209−213] and batteries.[214−218]

Several methods have been established for the morphological control including top-down and bottom-up approaches.[203,219] The most popular and often successful technique is the metal-assisted NW growth enabling control over the nucleation process as well as the NW's diameter and length as described in several review articles.[200−205] The earliest process description was provided by Wagner and Ellis considering a metal particle (Au) that enabled the formation of a Si NW.[220] In this process, schematically illustrated in Figure

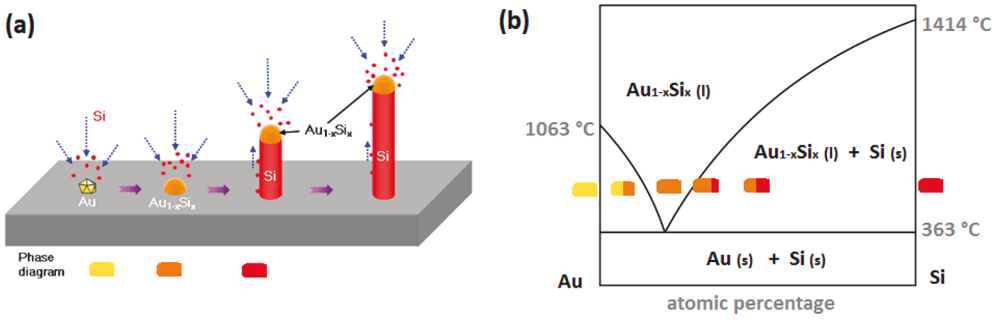

Figure 4. (a) Schematic of VLS growth mechanism of Si NWs. A $Au_{1-x}Si_x$ liquid alloy droplet is first formed above the eutectic temperature (363 °C) of the Au-Si system. The continued feeding of Si via the vapor phase into the liquid alloy causes its supersaturation, resulting in nucleation and NW growth. (b) Schematic binary phase diagram for Au and Si illustrating the important sections for the VLS mechanism. (b) Schematic is redrawn using ref 234 as reference.

https://dx.doi.org/10.1021/acs.chemmater.9b04471
Chem. Mater. 2020, 32, 2703−2741

4a, the metal particle forms a low melting alloy with the semiconductor and is eventually supersaturated causing the nucleation of a semiconductor crystal at the interface between the molten alloy and the supporting substrate. Supersaturation of a liquid metal alloy droplet and subsequent nucleation of the NW material can be easily understood by following the isothermal line in the binary phase diagram of the Au−Si system highlighted in Figure 4b. Since the crystal forms at the solid−liquid interface, the molten alloy particle remains at the tip region and enables further growth of the crystal underneath the particle. Thus, the NW's diameter is controlled by the size of the initial metal particle and the length by the process duration.[200−205] In reference to the state of the NW material, this growth is referred to as the vapor−liquid−solid (VLS) mechanism. Additionally, related but distinct growth modes are now distinguished by the aggregate state of the surrounding medium in which the process is carried out and the metal particle under growth conditions. Different abbreviations such as vapor−solid−solid (VSS),[221−223] solution−liquid−solid (SLS),[224,225] solution−solid−solid (SSS),[226,227] supercritical fluid−liquid−solid (SFLS),[228−230] and supercritical fluid−solid−solid (SFSS)[231−233] denote the phase state of the reactant supply, crystal growing medium, and crystal.

Here, supersaturation relates to an accumulation of the solute and subsequent crystal forming material in the liquid metal droplet. Supersaturation levels can exceed the thermodynamic solubility by orders of magnitude, which is caused by a large nucleation barrier for initiation of the next forming layer. The actual sequential growth of NWs has been visualized by TEM, which illustrates the oscillating solute content in the metallic growth seed upon layer formation.[235,236] These subtle but important facts show how different aspects of even the "simple" VLS mechanism for NW growth can influence the resultant nanostructure. In addition, the speed of crystal growth can vary over several orders of magnitude for the same material combinations, greatly influenced by external parameters, such as precursor concentration, pressure, temperature, *etc.*[237,238] In the very simple models additional contributions, such as surface diffusion *etc.*, are neglected. We refer to a recent review focused on NW growth for specifics.[205]

The term self-seeding of NWs refers to a metallic particle that acts as a seed both facilitating the nucleation and the growth of the NW and at the same time the metal is part of the NW material formed and was first described for III−V semiconductor growth with group III metal seeds.[239,240] For the successful incorporation of "impurity" atoms beyond the thermodynamic limit some important aspects must be considered which include growth rate, temperature, and growth promoter. However, the temperature not only influences the growth rate but also determines the mobility of the trapped heteroatom. Therefore, the goal to achieve efficient incorporation is to obtain high growth rates at low temperatures.[241] The chosen temperature is typically limited by the melting point of the growth promoter and decomposition kinetics of the precursors. In general, at elevated temperatures the mobility of the atoms is too high which supports the formation of the thermodynamically stable product. In conclusion, not every metal is suitable for classical VLS or self-seeding of a metastable material.

2. METASTABLE GROUP IV NANOSTRUCTURES

In this review, approaches to synthesize and stabilize zero- and one-dimensional metastable Si-, Ge-, and Sn-based materials are discussed in detail. This includes allotrope formation and uncommon, metastable solid solutions associated with incorporation heteroatoms beyond the thermodynamic limit. Often kinetically controlled *in situ* processes and the use of templates to enable the formation of a metastable phase are required, while for NPs changes of surface termination or a matrix can also support the formation of allotropes.

2.1. Si-Based Metastable Nanostructures. *2.1.1. Si Nanoparticles. 2.1.1.1. Si NPs: Allotropes.* Among the large number of Si allotropes, only the thermodynamically most favorable *dc*-Si as well as the metastable phases *fcc*-Si, *bc8*-Si, and *r8*-Si have been described being accessible as Si NPs that are stable at room temperature and atmospheric pressure. The interest in these phases is related to advantageous physical properties and applications such as higher solar energy conversion efficiency forecast by theoretical studies.[242] However, the synthesis of these particles appears to be very challenging.

The formation of *fcc*-Si NPs by plasma-enhanced CVD using silane,[243] laser ablation of Si,[244] magnetron sputtering of silica,[245] electron[246] or ion beam[247] irradiation of SiO_x films, and rapid thermal annealing of SiC_x layers[248] has been reported. While these examples show that an external energy input is required for the formation of the predominantly matrix-embedded *fcc*-Si NPs, additional effects including the presence of concave surfaces[249] and increased pressure due to synthesis conditions[250] have been suggested to contribute to the crystallization of this allotrope. In addition, a chemical solution-based approach can result in the formation of *fcc*-Si NPs by the reaction of silicon tetrachloride with sodium cyclopentadienide at room temperature leading to Si NP formation most likely due to the instability of putative Si cyclopentadienide.[251] Chemical stabilization was suggested as a reason for the observed metastable *fcc*-Si allotrope. According to a theoretical study on the properties of *fcc*-Si, metal-like behavior is expected;[252] however, PL emission in the blue[245] or green[251] region of the visible spectrum suggests semiconductor-like properties.

Similarly to the formation of NPs in the matrices described above, the rapid thermal annealing of layered amorphous Si/SiO_2 heterostructures is described to form *bc8*-Si NPs embedded in an amorphous matrix. The formation of the metastable Si allotrope NPs in this particular case can be caused by a large compressive strain within the formed heterophased system.[253] Furthermore, the pressure-induced formation of *bc8*-Si and *r8*-Si nanocrystal mixtures in a Si-based matrix has been observed during doping of Si with femtosecond laser irradiation sending shock waves through the material[254] as mentioned before and face grinding carried out on a Si(100) surface using diamonds.[255] While there is no report on phase pure *r8*-Si NP synthesis or its separation from matrices, nonstrain related synthesis of matrix-free, colloidal *bc8*-Si NPs has been realized via the reduction of SiI_4 with *n*-butyllithium and annealing at 280 °C.[256] The initial chemical reaction should lead to the alkylsilane, which is converted to the metastable material at higher temperatures under the applied conditions. The average NP size is determined to be 5.5 ± 1.1 nm by XRD and TEM analyses, and the formation of the metastable *bc8*-Si phase is confirmed. Even though the

https://dx.doi.org/10.1021/acs.chemmater.9b04471
Chem. Mater. 2020, 32, 2703−2741

authors refer to an oxide bond on the surface having an impact on the formation for the stabilization of the phase, these alkoxide groups terminating the NPs should not have any impact on the *bc8*-Si crystal being formed. Although it is well-known that energetic considerations as illustrated in Figure 5

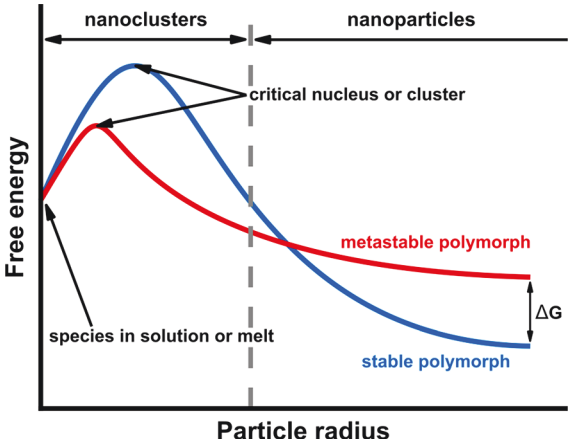

Figure 5. Schematic presentation of the free energy for different polymorphs plotted versus the particle radius (both axes do not have numerical values) illustrates differences in the critical nucleus size and the activation energy as well as a potential crossover in stability of the phases. Schematic is redrawn using ref 257 as reference.

and the growth mechanism are crucial issues for the successful synthesis of metastable phases via colloidal synthesis, the actual cause for the formation of the *bc8*-Si NPs is still unknown.[257] In Figure 5 the free energy for different polymorphs has been plotted versus the particle radius and shows schematically differences in the critical nucleus size and the activation energy as well as a potential crossover in stability of the phases. In case a metastable phase forms smaller stable nuclei with lower free energy required, this phase will be formed preferentially and can still exist for bigger particle sizes even though it would be energetically less favorable as a bulk material. This graph clearly points out the importance of both thermodynamics and kinetics for the formation of a metastable phase.

A similar result was obtained by a solution-based reduction process using tetraethyl orthosilicate as precursor either in the presence of molten Na or by addition of $NaBH_4$.[258] A small fraction of the formed 2−6 nm Si NPs reveals interplanar spacing expected for the *bc8*-Si allotrope.

Furthermore, the accessibility of high-pressure phases in Si NPs is reported for Si NPs obtained after the dissociation of silane via room temperature plasma synthesis. The alkane functionalization Si NPs are dissolved in an organic solvent and loaded into a diamond anvil cell under inert atmosphere. By this approach *sh*-Si and *hcp*-Si are observed at higher pressures but could not be stabilized at ambient pressure resulting in amorphous material.[259]

The limited number of reports on allotropes beyond *dc*-Si illustrates an area of opportunity. Establishing a reliable process for other matrix-free and phase-pure metastable Si allotrope NPs is needed.

2.1.1.2. Si NPs: Solid Solutions. On another note, Si NPs have been successfully hyperdoped with a wide range of different elements including transitions metals,[260−263] Li,[264] Au,[265] and Er,[266−269] as well as group III[270−281] and group V[265,272,275−278,280,282−287] elements. However, reports on impurity concentrations exceeding the thermodynamic limit in Si nanocrystals are very rare. In general, we refer to a binary, metastable Si phase where the maximum solid solubility of the specific element in Si is exceeded according to information extracted from the bulk binary phase diagram. However, elemental concentrations that are thermodynamically stable at the synthesis/annealing temperature but not at room temperature are not considered as hyperdoped due to the higher solid solubility of a solute/impurity at elevated temperatures. Therefore, metastable phases obtained by exceeding the overall thermodynamic solubility limit during crystal growth or by maintaining the composition at low temperatures that was incurred during high temperature synthesis should be distinguished. Table 1 illustrates the maximum solid solubility and the maximum contents described to be incorporated in Si NPs discussed in this section

2.1.1.2.1. Solid Solutions of Transition Metals in Si NPs. Mn[260] and Fe[261] have been successfully incorporated in Si NPs in a solution-based process using Zintl salts as single-source precursors. For instance, $Si_{1-x}Mn_x$ NPs form by addition of NH_4Br to $NaSi_{1-x}Mn_x$ in a polar solvent of low vapor pressure. Stabilization of the NPs in solution is achieved by *in situ* hydrosilylation with an alkene. Elemental analysis reveals a maximum of 5 atom % Mn while a phase-pure product has been observed by XRD analyses. However, an additional amorphous phase is present in the XRD pattern and thus an accumulation of Mn atoms in the noncrystalline part of the sample cannot be ruled out. Thus, the Mn content in the Si

Table 1. Maximum Thermodynamic Limit of Element Incorporation in Si According to the Corresponding Binary Phase Diagram and Observed Contents in Si NPs

	maximum thermodynamic limit			content in Si NPs			
element	(atom %)	(cm^{-3})	ref	(atom %)	(cm^{-3})	characterization technique	ref
As	3.5	1.75×10^{21}	288	n-doped		electrical and PL	287
Au	2×10^{-4}	1×10^{17}	234	0.06	3×10^{19}	controlled implantation and PL	265
B	3	1.5×10^{21}	289	∼1/42	$\sim 5 \times 10^{20}/2.1 \times 10^{22}$	APT/ICP-OES	280, 290
Co	2.6×10^{-5}	1.3×10^{16}	291	0.10	5×10^{19}	ICP-OES	263
Cu	1×10^{-4}	5×10^{16}	292	0.7	3.5×10^{20}	EDX	262
Er	2×10^{-7}−2×10^{-5}	10^{14}−10^{16}	293	4	2×10^{21}	EDX	269
Fe	3×10^{-5}	1.5×10^{16}	294	0.90	4.5×10^{20}	ICP-MS	261
Li	0.14	67.0×10^{19}	295	0.2−2	10^{20}−20^{21}	NDP	264
Mn	up to 0.80	up to 4×10^{20}	296	5	2.5×10^{21}	elemental analysis	260
Ni	1.4×10^{-3}	7.0×10^{17}	297	0.6/0.18	$3 \times 10^{20}/9 \times 10^{19}$	EDX/ICP-OES	262, 263
P	2.4	1.2×10^{21}	298	∼5	$\sim 2.5 \times 10^{21}$	EDX/ICP-AES	284, 299

https://dx.doi.org/10.1021/acs.chemmater.9b04471
Chem. Mater. 2020, 32, 2703−2741

NPs might be overestimated by the simple elemental analysis. Nevertheless, electron paramagnetic resonance (EPR) measurements and transient absorption spectroscopy confirm the successful incorporation of Mn in the Si lattice.[260] An identical approach can be used for $Si_{1-x}Fe_x$ NPs using an Fe-containing Zintl salt.[261] The maximum Fe content of these small Si NPs with diameters of ∼3 nm has been determined by inductively coupled plasma mass spectrometry (ICP-MS) to be 0.90 ± 0.10 atom % and reveals a quantum yield of 10.0 ± 1.5% as determined by photoluminescence (PL) measurement. EPR measurements as illustrated in Figure 6 and Mössbauer

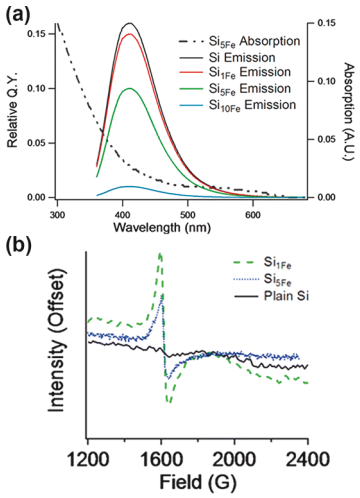

Figure 6. (a) Relative quantum yield for the emission of amine-terminated water-soluble Si and Fe doped Si NPs have been determined.[261] (b) X-band EPR spectra of amine-terminated Si and Fe doped Si NPs acquired at 10 K indicate the presence of isolated high-spin Fe(III) centers under rhombic distortion in Fe containing samples.[261] Adapted with permission from ref 261. Copyright 2012 American Chemical Society.

spectroscopy suggest the presence of Fe^{3+} in the Si crystal lattice while Fe clustering has been excluded.[261] For the sample Si_{1Fe} with an Fe content of 0.60 ± 0.20 atom % the quantum yield is quite similar to that of undoped Si NPs. Higher Fe contents result in a decrease in the quantum yield which has been attributed to the presence of byproducts (Figure 6). However, magnetic resonance imaging experiments using Si NPs doped with 0.90 atom % Fe reveal a high contrast confirming the alteration of magnetic properties by incorporating paramagnetic ions.[261] The described methods to change the magnetic properties of biocompatible Si NPs while at the same time retaining a reasonable value of the PL quantum yield are of great interest due to the possibility of combining optical detection with magnetic resonance imaging or magnetic separation.[260,261]

2.1.1.2.2. Solid Solutions of Lithium in Si NPs. Extensive Li incorporation in Si NPs has been observed by an electrochemical approach.[264] A brightly luminescent Si NP layer with crystal sizes between 2.5 and 3 nm can be obtained by electrochemical etching of a Si substrate. The 3−4 μm thick Si NP layer is used as an electrode in combination with a Pt counter electrode and a LiCl-based electrolyte. After the electrochemical process the Si NP sample is characterized by neutron depth profiling (NDP), X-ray diffraction (XRD), and time-resolved PL. XRD shows an expansion of the Si lattice due to Li insertion while retaining the crystal structure. Quantification by NDP reveals a Li content of 10^{20}−10^{21} cm^{-3} (0.2−2 atom %) in the Si NP film. The PL spectra show a blue-shifted emission, which can be attributed to tensile strain caused by Li insertion, while the signal intensity for Li doped Si NPs decreased slightly.[264] In general, the incorporation of Li in group IV elements is a highly interesting field of research due to their high capacity qualifying them as efficient anode materials for Li ion batteries.[214] However, the targeted incorporation of high amounts of Li is accompanied by changes in the crystallographic phase and is therefore not further discussed.[300]

2.1.1.2.3. Solid Solutions of Erbium in Si NPs. Rare earth metals with large atomic radii can be incorporated in the crystal matrix of Si NPs. Pyrolysis of disilane and volatile metal−organic Er precursors in a gas-phase process at 1000 °C yield Si NPs containing high Er concentrations.[266,267,269] While Er beta-diketonates allow the incorporation of ∼2 atom %,[266,267] Er amidinates enable higher hyperdoping levels of 4 atom % Er in the Si NPs most likely due to the energetically favored cleavage of the Er−N bonds.[269] Er hyperdoped Si NPs exhibit excellent emission of light in the near-IR range due to the presence of Er^{3+} centers in the Si host lattice.[301] However, quenching effects regarding the PL intensity have been obtained for Er contents exceeding approximately 0.4 atom % (2×10^{20} cm^{-3}) in the Si NPs.[301]

2.1.1.2.4. Si NPs Containing Group III or V. Nonmetal hyperdoping of Si NPs by B or P beyond the thermodynamic limit is of great interest to alter surface plasmon properties by tuning the charge carrier concentration.[302] In contrast to bulk Si where B and P atoms reside typically at substitutional sites in the Si host lattice, the heteroatoms in NPs should be enriched on the surface.[307] The importance to control elemental distribution is pointed out in a theoretical study on P doped Si NPs showing the dependence of the dopant location on the optical properties of this nanomaterial.[308] A growth of metastable materials by nonthermal plasma synthesis has been suggested due to the selective heating of NPs up to very high temperatures while the gas temperature remains close to room temperature.[303] Si NPs with high B contents up to 31 atom % have been reported in the literature, which is far above the solid solubility.[277−279,281] The electrically active B concentration in Si NPs with incorporation of 31 atom % B is estimated to be only 0.98 atom % (4.9×1020 cm^{-3}) based on Fourier transform infrared (FTIR) spectroscopy results that are related to a shift of the localized surface plasmon resonance (LSPR)-induced absorption.[281] The active B content is very close to B doped Si NPs embedded in an oxide matrix prepared by thermal annealing of a codeposited layer of Si, silica, and boron oxide (B_2O_3).[274,280] The B content in Si NPs synthesized by this approach is determined by atom probe tomography (APT) to be 1.0 atom %[280] which is in good agreement with the electrically active B concentration of 0.98 atom % observed for highly B doped Si NPs.[281] Therefore, clustering of B can be mostly excluded in this latter case while a potential limitation of electrically active B sites in Si NPs and an accumulation/clustering of B at the NP's surface must be considered for high B contents. In this respect, there are several studies on the preferred incorporation of B in the core of Si NPs,[278,299] while other reports suggest accumulation on the surface.[304] This raises the question whether B is clustering in the Si NP lattice or is a homogeneous distribution and thus a solid solution can be expected. Very recently, Si NPs with B contents up to 42.5 atom % and an average diameter of

https://dx.doi.org/10.1021/acs.chemmater.9b04471
Chem. Mater. 2020, 32, 2703−2741

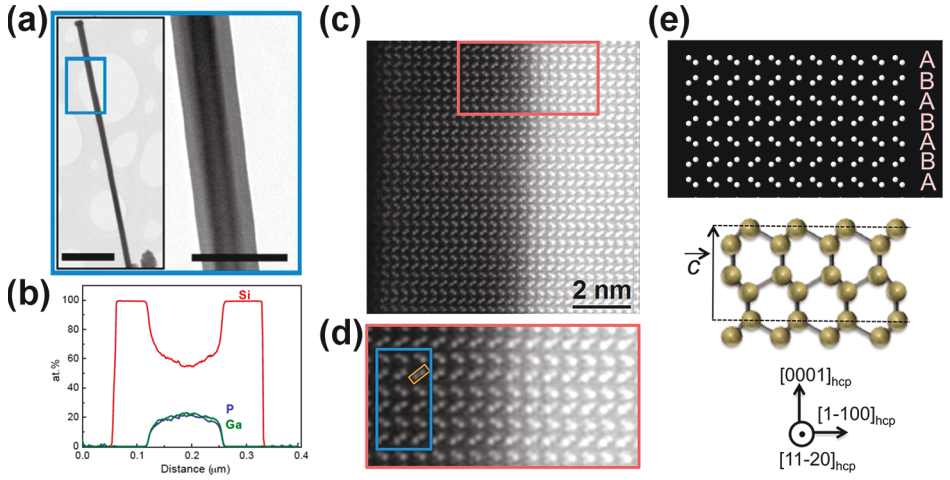

Figure 7. (a) TEM images of a GaP/Si core−shell nanowire showing the conformal growth of Si on the GaP NW template. (b) The elemental distribution of Ga, P, and Si across the core−shell NW is illustrated by an EDX line scan. (c) HR-HAADF STEM is used to image the GaP/Si interface obtained in the $[11\bar{2}0]$ zone axis. (d) The red box marked in (b) is magnified. (e) An atomic model of 2H-Si grown in the (0001) direction and imaged in the $[11\bar{2}0]$ zone axis is in good accordance with results from (c) showing the ABABAB... stacking sequence. Furthermore, Si dumbbells from the atomic model shown on the bottom of (e) can, e.g., be found in the orange box in (d).[335] Reprinted with permission from ref 335. Copyright 2015 American Chemical Society.

approximately 25 nm were synthesized via laser-induced pyrolysis of a silane/diborane mixture.[290] The B distribution and content are determined using several complementary methods including energy dispersive X-ray spectroscopy (EDX), electron energy loss spectroscopy (EELS), and ICP-OES. EDX maps confirm the homogeneous distribution of B in the Si NPs and EELS suggests the formation of Si−B bonds. In addition, etching experiments in combination with ICP-OES exclude the accumulation of B on the surface of the Si NPs by this approach. Characterization via XRD reveals the presence of *dc*-Si and absence of additional crystalline phases. Optical characterization of the B hyperdoped Si NPs is performed via Raman spectroscopy showing a clear redshift of the Si−Si vibration peak for all B concentrations due to strain effects. Furthermore, the presence of Si−B vibrational peaks is reported which is in good agreement with the EELS measurements. LSPR-induced absorbance is measured via FTIR and suggests the formation of free holes in the Si matrix. A blue shift of the LSPR peak upon increasing the B content is observed. A free carrier concentration of approximately 4.3×10^{20} cm^{-3} has been determined for hyperdoped Si NPs with 42.5 atom % B[290] which agrees well with the limit of the electrically active B concentration discussed before and therefore suggests the presence of electrically neutral interstitial clusters[305] above this limit of ∼1 atom %.

Similarly, nonthermal plasma synthesis allows the preparation of Si NPs with very high P contents.[277,278,284,299] In a preliminary study 5.6 atom % P, determined by inductively coupled plasma atomic emission spectroscopy (ICP-AES), was incorporated into Si NPs.[299] X-ray photoelectron spectroscopy (XPS) studies confirm the accumulation of P near/on the surface of these Si NPs[278] which is in good agreement with previous reports.[299,306]

In general, the main questions concerning highly doped Si NPs include the spatial distribution of incorporated heteroatoms in the Si host lattice, the possibility of cluster formation, the crystallinity, the size distribution, the oxide/amorphous shell, the accumulation at the surface, and the origin of the absorption/emission. Complementary analysis methods are required to clarify the remaining questions enabling the controlled alteration of synthesis procedures to obtain a more efficient incorporation of metal and nonmetal atoms in the Si crystal lattice of NPs.

2.1.2. Si Nanowires. 2.1.2.1. 2H-Si NW Formation. Several successful approaches to synthesize metastable Si NWs are reported. It can be differentiated between methods based on doping beyond the thermodynamic limit and metastable Si obtained by a template-assisted or metal-induced growth process.

In terms of Si allotropes, the most prominent phase investigated is the 2H-Si which has been reported for NWs and segmented heterostructures.[309−320] According to theoretical studies, 2H-Si reveals advantageous optical and electronic properties when compared to its *dc*-Si counterpart for applications in photovoltaics, quantum photonics, and optoelectronics.[321,322] However, the characterization of the 2H-Si phase is complicated due to the lack of appropriate samples and difficulties to stabilize this Si allotrope once it is synthesized. Therefore, it is very important to develop synthesis strategies taking also stability issues of 2H-Si into account. To date, physical properties are primarily known from theoretical studies predicting an indirect bandgap for 2H-Si with a lower bandgap energy than its dc counterpart.[75,321,322] Furthermore, the transition into a direct bandgap semiconductor with a bandgap energy below 1 eV by applying high biaxial tensile strain of ∼4% is reported in the literature.[321] In addition, 2H-$Si_{1-x}Ge_x$ solid solutions are direct bandgap materials for $x > 0.65$ with a tunable bandgap dependent on the composition as recently demonstrated and discussed *vide infra*.[323] The majority of the literature reports provide the evidence for the presence of the 2H phase in Si NWs and heterostructures via high-resolution transmission electron microscopy (HRTEM), electron diffraction, and Raman analyses.[309−319]

However, several studies describe the data from electron diffraction patterns that were initially assigned to 2H-Si as a double diffraction of superposed twinned crystals.[324−329] Moreover, the Raman peak shifts toward the expected value

https://dx.doi.org/10.1021/acs.chemmater.9b04471
Chem. Mater. 2020, 32, 2703−2741

for the 2H-Si can be caused by defects and therefore are not necessarily a clear evidence for the presence of the metastable Si allotrope.[328] Nevertheless, several reports describe the presence of 2H-Si using characterization methods capable of an unequivocal identification.[319,320] For instance, it is highly recommended/vital to use the $[110]_{3C}/[1\bar{2}10]_{2H}$ zone axis to distinguish between double diffraction caused by twins and 2H-Si when using HRTEM/electron diffraction for the characterization.[319] In addition, atomic resolution high-angle annular dark-field scanning transmission electron microscopy (HAADF STEM) imaging along the $[1\bar{2}10]$ zone axis can be used to confirm the presence of 2H-Si by interpretation of the Si dumbbells expected in this orientation.[320]

The diffusionless shear (martensitic) transformation by microindentation in the temperature range 400−500 °C is well-known to transform *dc*-Si into 2H-Si.[330−332] Similarly, epitaxial 2H-Si nanoribbons are obtained from *dc*-Si fin structures.[333] Gaps in between the initially etched *dc*-Si fins are filled with SiO_2, while high temperature annealing and the associated densification leads to mechanical stress with the highest values close to the fin−substrate interface. In this highly strained region, a martensitic phase transformation to the 2H-Si phase can be observed which is confirmed by HR-HAADF STEM analyses. Similarly, segmented *dc*-Si/2H-Si NW heterostructures can be prepared by the shear stress in the radial direction by densification of a SiO_2 matrix embedding the Si NWs.[334]

Furthermore, pure and stable 2H-Si has been realized by the epitaxial growth on wurtzite GaP NWs acting as templates.[335] The GaP NW substrate's crystal structure is transferred to the Si layer crystallizing at the sidewalls of the III/V template forming a conformal shell as illustrated in Figure 7a. The expected elemental distribution for a GaP/Si core−shell NW is confirmed by an EDX line scan in the radial direction (Figure 7b). The crystal structure of the Si shell is determined by HR-HAADF STEM (Figure 7c,d) and Raman spectroscopy analyses confirming the presence of the metastable 2H-Si phase. The simulated atomic model of the 2H-Si phase in the imaged zone axis (Figure 7e) perfectly agrees with the observed TEM data.[335] Recently, tetrasilane has been used for the epitaxial growth of 2H-Si on the sidewalls of GaP NWs at moderate temperatures, which is vital to gain control over the thickness and uniformity of the 2H-Si shell and to prevent incorporation of Ga and P impurities by diffusion processes at high synthesis temperatures of 900 °C when monosilane is used as precursor.[336] This approach paves the way to grow hexagonal diamond 2H-$Si_{1-x}Ge_x$ and 2H-Ge which are expected to be direct bandgap semiconductors[337] and will be discussed *vide infra*.

Moreover, the formation of the 2H-Si in VLS grown NWs has been observed and attributed to the small diameter, the Sn growth promoter, and the plasma-assisted CVD process for their synthesis.[319] The metastable 2H-Si allotrope in NWs is stable at ambient conditions and withstands thermal annealing at 700 °C. In contrast to this highly selective template synthesis, the formation of the 2H phase in the kinked part of the Si NWs can be traced back to high defect densities in these regions.[320] More detailed investigations are required to elucidate the diameter dependence of the 2H-Si NW growth and a potential role of the Sn growth promoter.

Studies concerning the impact of doping on 2H-Si NWs reveal a higher stability upon B doping, while P doping leads to a higher portion of *dc*-Si NWs.[317,318,338] An optical bandgap of 1.5 eV is determined for B doped Si NWs which is attributed to the 2H-Si phase.[317,318] In addition, a theoretical study supports the energetically preferred incorporation of group III dopants in 2H-Si due to a stronger tendency to stabilize a 3-fold coordination around the heteroatom.[338] Clear evidence for the formation of 2H-Si as proposed *vide supra* is missing in these studies, and therefore the origin of the results obtained via optical and optoelectronic measurements are vague. However, XRD data support the assignment to the 2H-Si phase at least for a portion of the material.

2.1.2.2. Hyperdoping of Si NWs. The metal-supported growth of Si NWs is an approach suitable for the *in situ* incorporation of heteroatoms in the Si host lattice. Therefore, it must be distinguished between a self-seeding process, where the metal growth promoter is consumed during the growth due to incorporation in the growing crystal lattice, and processes where the metal particle merely mediates the incorporation of dopants and anisotropic crystal growth. Au-assisted formation of Si NWs is a popular technique and widely investigated in literature.[203,204,339,340] Au is mostly regarded as an inert VLS growth promoter in terms of oxidation under ambient conditions and formation of stable binary compounds, thus enabling the growth of NWs with various compositions.[341] The incorporation of $\sim 1 \times 10^{17}$ cm^{-3} Au atoms during the Au-supported VLS growth of Si NWs[342] is a minor effect for the hyperdoped samples which usually contain orders of magnitude higher dopant levels. The direct incorporation of the seed material will be discussed in more detail *vide infra*. Significant B[343−346] and P[347−352] doping of Si NWs grown from Au is achieved by separate gaseous precursors. This is an important strategy to achieve a very desirable p- and n-type doping for the realization of NW-based electronic devices.[200]

At low growth temperatures and low partial pressures Si NWs reveal an incorporation-limited growth regime, while at high temperatures and partial pressures a crystallization-limited growth regime is observed. Further, the diameter of the Si NWs has a strong impact on the growth rate.[353] The targeted control over the doping concentration and profile has stimulated several studies on the limits of dopant incorporation and the importance of kinetics for such a process.[347−349,351,352] Moreover, several methods have been presented to accurately determine dopant concentration, distribution, and enrichment including electrical measurement on single NW devices,[343,354] Kelvin probe force microscopy,[355] scanning photocurrent microscopy,[348,355] nanoprobe scanning Auger microscopy,[348] APT,[241,356] EDX,[357,358] EELS,[358] secondary ion mass spectrometry (SIMS),[359] electron microscopy,[241,360] and associated morphological effects such as encoded NW growth and appearance through VLS and etching.[361]

2.1.2.2.1. Incorporation of Groups III and V in Si NWs. To date, despite extensive understanding of the kinetics of incorporation, adding B and P beyond the maximum thermodynamic solid solubility limit has not been reported. The Au-assisted VLS growth of Si NWs reveals maximum B contents of approximately 10^{20} cm^{-3} (0.2 atom %), which show the highest electrically active doping level of 4.5×10^{19} cm^{-3} (9.0×10^{-2} atom %).[352] Incorporation of B beyond the thermodynamic limit at this synthesis temperature is attributed to solute trapping in combination with a substantially lower barrier for B incorporation into the liquid Au catalyst compared to Si.[352] Furthermore, doping VLS-grown Si NWs with up to 5.0×10^{20} cm^{-3} (1.0 atom %) P by the supply of phosphine during growth has been observed by EDX analyses.

https://dx.doi.org/10.1021/acs.chemmater.9b04471
Chem. Mater. 2020, 32, 2703−2741

The determined value is far beyond the thermodynamic limit[298] at the chosen growth temperature of 480 °C but below the overall solubility limit.[352] In a previous study, an electrically active P concentration of 1.5×10^{20} cm^{-3} (0.3 atom %) in Si NWs produced by a similar attempt has been determined by electrical characterization of a single NW device.[347] These Si NWs reveal extremely low resistivity values down to 6×10^{-4} Ω·cm, but the actual chemical composition has not been determined by any other analysis technique. However, a much higher P content is considered for those Si NWs due to the well-known partial incorporation of electrically inactive P species in the Si crystal.[347]

2.1.2.2.2. Incorporation of the Seed Material in Si NWs. In a typical VLS growth of NWs, the transport of atomic species plays a crucial role highlighting the importance of kinetics beside thermodynamic considerations. A schematic presentation of some essential processes during the VLS growth of Si NWs is shown in Figure 8a. According to reports in literature,

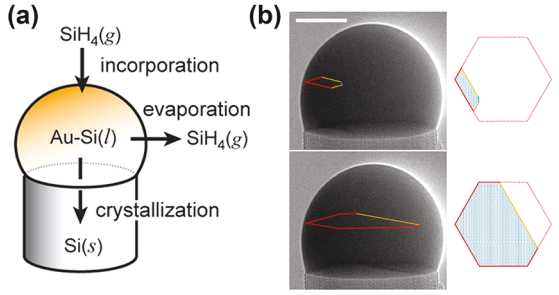

Figure 8. (a) The schematic illustration highlights crucial processes during the VLS growth of Si NWs including incorporation, evaporation, and crystallization.[353] Reprinted with permission from ref 353. Copyright 2014 American Chemical Society. (b) Step-flow growth is also observed in GaAs NWs using *in situ* TEM, and the propagation of the GaAs monolayer is schematically reproduced to illustrate the layer-by-layer growth of a NW.[362] Reprinted with permission from ref 362 Copyright 2018 by the American Physical Society.

the crystallization of group IV[363,364] but also of III–V compound[362] NWs by the VLS mechanism proceeds by the nucleation of individual (bi)layers and subsequent step-flow growth (see Figure 8b). During this (bi)layer formation, atoms of the growth promoter can be incorporated in the Si host lattice by an *in situ* solute trapping[365] at edges, which is well-described in the literature.[366−372] The lateral velocity of the step propagation is a critical parameter for solute trapping and strongly depends on thermodynamics and kinetics of the given binary system.[371] A tapered morphology of a NW grown via the VLS mechanism can hint toward incorporation of metallic atoms from the seed or being a combination between the axial extension of the NW and radial growth via a layer deposition by vapor–solid (VS) growth. While this layer growth is a coating process typically not including any doping via a gaseous source, dopant diffusion on the sidewalls of the NW[371] and unstable growth conditions leading to surface diffusion[373] have to be taken into account. Thus, an accurate characterization of the material is essential to gain information concerning the growth mechanism. Furthermore, segregation of heteroatoms at grain/twin boundaries[374] and incorporation of clusters in the Si NW matrix[375,376] must be excluded to confirm the formation of a solid solution. Several metal seeds have been applied as growth promoter for Si NWs including Ag,[377,378] Al,[379−384] Au,[220,385−387] Bi,[307,388,389] Co,[390] Cu,[310,386,391] Dy,[392] Fe,[392,393] Ga,[394−397] Gd,[398] In,[380,394,399,400] Mn,[398] Ni,[220,378,401,402] Pb,[374,378] Pd,[363] Pt,[375,403] Sn,[166,404−406] Ti,[407,408] Zn,[409,410] and binary alloys[241,388,411−414] of these elements.[347] Among these metal seeds, only a few examples exist that facilitate the VLS/SLS growth of Si NWs and simultaneously lead to hyperdoping of the Si crystal (Table 2). Furthermore, information on the maximum (electrically active) dopant level achieved for each system is listed. According to the data collected in Table 2, the efficient incorporation of heteroatoms beyond their maximum solid solubility via the growth promoter in a self-seeding process has been achieved for a rare number of systems.

Reports describing surface accumulation and clustering without any sign of homogeneous incorporation or proper determination of heteroatomic species in the Si lattice are omitted, even though conductivities and electrical properties have been determined.[374] In other studies the incorporation of high amounts of metal atoms from the seed in the Si NW host lattice can be expected on the basis of follow-up papers describing successful incorporation, but metal incorporation

Table 2. Summary of Metal Facilitating Si NW Growth via the VLS/SLS Mechanism

	maximum solid solubility			maximum element incorporation				maximum electrically active doping level			
metal	(atom %)	(cm^{-3})	ref	(atom %)	(cm^{-3})	method	ref	(atom %)	(cm^{-3})	resistivity (Ω·cm)	ref
Al	1.6×10^{-2}	8×10^{18}	415	4.5	2.3×10^{21}	EDX	371	4.8×10^{-2}	2.4×10^{19}	1.6×10^{-2}	416
Au	2×10^{-4}	1×10^{17}	234	$\sim 1.0 \times 10^{-3}$–3.0×10^{-3}	$\sim 5.0 \times 10^{17}$–1.5×10^{18}	MS	417	-	-	$0.02/2.6 \times 10^{-3}$	418/419
Bi	1.8×10^{-3}	9.0×10^{17}	420	-	-	-	-	level unknown/n-doped			307, 389
Cu	1×10^{-4}	5×10^{16}	292	-	-	-	-	-	-	0.1	391
Ga	0.2	10^{20}	421	-	-	-	-	level unknown/p-doped			389
In	8×10^{-4}	4×10^{17}	422, 423	5.43×10^{-2}	2.72×10^{19}	APT	241	-	-	-	-
Sn	0.1	5×10^{19}	111	2.12×10^{-1}	1.06×10^{20}	APT	241	-	-	-	-
Zn	1.2×10^{-4}	6×10^{16}	421	-	-	-	-	-	-	31.9	419
Au + B_2H_6	3	1.5×10^{21}	289	~0.2	$\sim 10^{20}$	EELS and XPS	424	9.0×10^{-2}	4.5×10^{19}	2.08×10^{-3}	424
Au + PH_3	2.4	1.2×10^{21}	298	1.0	5×10^{20}	EDX	352	0.30	1.5×10^{20}	6×10^{-4}	347

https://dx.doi.org/10.1021/acs.chemmater.9b04471
Chem. Mater. 2020, 32, 2703−2741

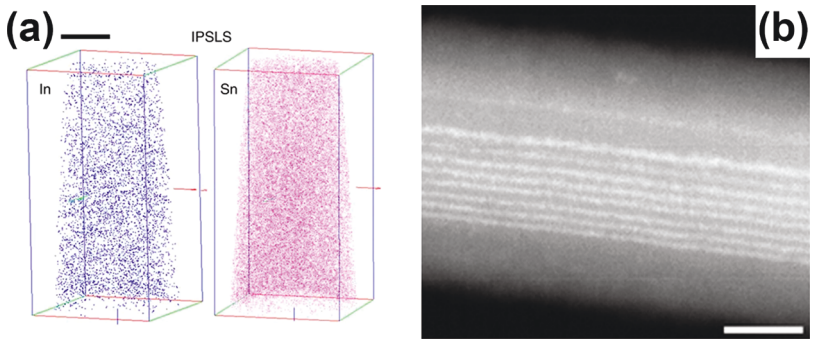

Figure 9. (a) Si NWs grown via an in-plane solid−liquid−solid mechanism using an In−Sn alloy as a seed reveal a homogeneous distribution of both species according to APT measurements.[241] Reprinted with permission from ref 241. Copyright 2014 Springer Nature. (b) A Z-contrast STEM image along the Si NW axis reveals the enrichment of Au at planar defects in Au-seeded Si NWs.[360] Reprinted with permission from ref 360. Copyright 2012 American Chemical Society.

has not been discussed and direct proof via quantitative characterization methods is missing in these reports.[379,389,396,397,416,425]

The incorporation of Au in Si from the seed is also not mentioned in most reports, even though Au concentrations in Si NWs can be in the range of the solid solubility of $\sim 1 \times 10^{17}$ cm^{-3} ($\sim 2 \times 10^{-4}$ atom %)[234] which is significant for the electronic performance since Au introduces deep-level traps.[342] A report on doping of Si NWs with Au slightly beyond the expected thermodynamic limit via self-seeding can be found in literature.[417] In addition to the VLS growth with homogeneous distribution, higher concentrations can be found when Au is trapped at defects along the Si NW axis[360,417] and when surface diffusion/wetting can lead to incorporation of Au in the shell region of core−shell NWs.[426−428] Furthermore, it has to be differentiated between metal seed incorporation in the NW body and metal spreading by surface wetting and subsequent diffusion which can give the impression of incorporation in the Si host lattice. For instance, during shell formation in Si/Ge core−shell NW growth, surface/interface accumulation of Au occurs without the determination of where the Au is actually located.[428] The spreading can be assigned to surface wetting of Au on the Ge NW core and subsequent Si shell growth. However, this effect can be prevented by controlling the surface termination and thus wettability for Au by the growth of a Si segment terminated by Cl.[426,427]

2.1.2.2.2.1. Direct Al Hyperdoping of Si NWs. Nevertheless, incorporation of heteroatoms far beyond the thermodynamic solubility limits is reported for Al-seeded Si NWs.[371,381−383] For instance, conductive atomic force measurements provide a clear evidence for p-doping of these structures and thus suggest successful incorporation of Al in the Si lattice.[382] An electrically active dopant concentration of 6×10^{18} cm^{-3} (1.2×10^{-2} atom %) has been observed for self-seeded Si NWs using Al growth promoters.[381] However, incorporation of Al far beyond the thermodynamic solubility limit is reported in subsequent studies.[371,382,383] In a vapor-phase process performed far below the eutectic temperature of the Al−Si system, monosilane is used as the precursor, and incorporation of up to 4.5 atom % (2.3×10^{21} cm^{-3}) Al in the Si host lattice is reported.[371] Although the growth rate of these NWs is quite moderate, which would in theory counteract solute trapping of such high amounts of heteroatoms, the authors suggest a large incubation time required for the nucleation of a new bilayer. Once a nucleus is formed, the step-flow growth of the bilayer can proceed quite quickly across the whole NW diameter enabling efficient Al incorporation via solute trapping. Furthermore, a strong dependence of the Al incorporation on the growth temperature is reported leading to a decrease from 4.5 atom % to 0.4 atom % (2.0×10^{20} cm^{-3}) when the temperature is decreased from 470 to 410 °C. Therefore, many parameters including the activation energy of atomic jumps, the required time for the formation of a bilayer, *etc.* must be considered when targeting the efficient incorporation of heteroatoms via a metal growth seed.[383] However, a further study on the Al-assisted Si NW growth confirms the incorporation of a high amount of Al in the Si host lattice but also reveals a strong accumulation of Al at twin domains,[429] which are natural sinks for the enrichment of impurities.[241,360]

2.1.2.2.2. Incorporation of Sn in Si NWs. According to the binary phase diagram, the solid solubility of Sn in Si is very low (0.10 atom %; 5.1×10^{19} cm^{-3}).[111] The first strong hint toward successful Sn incorporation in the Si nanowire host lattice via self-seeding was reported for Si NWs in a plasma-enhanced CVD process including the *in situ* reduction of SnO_2 to form metallic Sn seeds.[166] The produced Si NWs reveal a strong lattice expansion of 1.6% according to XRD and 2% in HRTEM analyses. However, no specific Sn content has been determined in this study, and the density and morphology of the Si NWs material is rather poor.[166] Therefore, additional characterization would be required to provide more insight and the actual reason for the lattice expansion. An even higher incorporation of 2.15 atom % (1.08×10^{21} cm^{-3}) Sn in the Si NW lattice is reported for SFLS growth at 490 °C, which is well above the eutectic temperature.[168] This value is boosted to 10 atom % (5.01×10^{21} cm^{-3}) as determined by STEM-EDX by an exchange of the Si precursor from monophenylsilane to the more thermolabile trisilane.[167] The higher Sn incorporation/trapping efficiency could be explained by the increased thermal decomposition rate of the Si precursor, thus resulting in a higher growth rate and more efficient solute trapping. *In situ* TEM studies using these Si NWs with high Sn content reveal increased lithiation rates when compared to intrinsic Si NWs.[430] However, the difference in atomic size equals an increase of 25.2% from the Si covalent atomic radius to Sn[163] and makes an efficient alloying in the aforementioned concentrations unlikely. Hence, more detailed analyses would be required to validate the homogeneous composition and crystal quality of the obtained Si NW material. Indeed, in the solution-based synthesis, strong hints can be observed that the determined amount of Sn is not homogeneously incorporated

https://dx.doi.org/10.1021/acs.chemmater.9b04471
Chem. Mater. 2020, 32, 2703−2741

in the Si crystal lattice but rather segregation/cluster formation has been initiated during or after the growth.[167,168,430]

2.1.2.2.2.3. Hyperdoping with Sn and In in Si NWs Using Bimetallic Seeds. Self-seeding and an associated efficient catalyst trapping is also reported for In and Sn by using an In−Sn alloy as the growth promoter for Si NW synthesis.[241] The maximum In/Sn incorporation is 2.72×10^{19} cm^{-3} (5.43×10^{-2} atom %)/1.06×10^{20} cm^{-3} (2.12×10^{-1} atom %) for in-plane solid−liquid−solid (IPSLS) grown Si NWs according to the very accurate APT (Figure 9a). Interestingly, the concentration of In is only slightly beyond the overall thermodynamic limit, while for Sn the limit is not exceeded. However, the incorporation of both metals in the Si crystal should be considered as a specific case since both atomic species are much larger than the Si atoms forming the host lattice resulting in high amounts of strain upon incorporation. The authors attribute the increased concentrations in the solid solution to the high growth rates of Si NWs. It should be mentioned that the solid solubility limits for In and Sn in the ternary Si−In−Sn system are not described in the literature. Nevertheless, the authors describe similar In and Sn concentrations when using the pure metals as the growth promoter, which confirms their achievement of heteroatom incorporation beyond the thermodynamic solubility limit at the growth temperature via a self-seeding process and high growth rates. In addition to the incorporation in the crystal lattice, enrichment of impurities on twin planes can be observed. For instance, Si NWs grown via the IPSLS mechanism and with high growth rate of 18 $nm \cdot s^{-1}$ show both the random/statistical incorporation of In and Sn in the crystal lattice as well as enrichment of In at twin defects.[241] As discussed before, similar results have been observed for Au-seeded, VLS-grown Si NWs as illustrated by Z-contrast in STEM perpendicular to and along the Si NW axis with the accumulation of the larger Au atoms at the twin boundaries (Figure 9b).[360]

2.2. Ge-Based Nanostructures of Metastable Composition. *2.2.1. Ge-Based Nanoparticles. 2.2.1.1. Ge NPs: Metastable Allotropes.* Reports on the synthesis of metastable allotropes of Ge are limited to the simple tetragonal *st12*-Ge phase, which can be derived by annealing of sputtered ZnO/Ge multilayer films,[431] cluster-beam gas-phase techniques,[432] thermal evaporation under argon,[433] laser ablation of Ge in liquids,[434] and naphthalide-mediated reduction of $GeCl_4$ at ambient temperatures.[435] Moreover, *st12*-Ge has been observed during delithiation in batteries; however, the high Li content in the material also suggests a layered structure of Ge and Li and thus not an allotrope nor a solid solution in this case.[436] An explanation for the formation of *st12*-Ge NPs has been proposed based on theoretical calculations showing small energetic differences when compared to the most stable *dc*-Ge phase for nanocrystals, which can be overcompensated by the NP morphology and surface termination while rendering the st12 phase more favorable.[437]

Theoretical band structure studies predict *st12*-Ge is a direct band semiconductor with a 1.47 eV energy gap, thus making it an attractive material for optoelectronics applications.[73] However, more recent experimental data reveal an indirect bandgap of ∼0.6 eV and a direct bandgap of ∼0.74 eV for *st12*-Ge single crystals, which is quite similar to *dc*-Ge.[438]

2.2.1.2. Ge Nanoparticle Solid Solutions. 2.2.1.2.1. Hyperdoping of Ge NPs with Groups III and V. Incorporation of group III and V atoms in a Ge nanocrystal can be achieved by a solution-based synthesis route.[439] Iodides of Ge and the dopants have been mixed prior to initiating an *in situ* salt elimination by adding butyllithium and subsequent ramping to the growth temperature for thermal decomposition. The synthesized products with diameters in the range of 3−5 nm are characterized via TEM, and the elemental composition has been quantified via elemental analysis using inductively coupled plasma optical emission spectroscopy (ICP-OES) as well as X-ray fluorescence (XRF) spectroscopy for the heavier elements. According to the binary phase diagrams, the maximum solubility limits of Al (1.1 atom %),[440] Ga (1.1 atom %),[441] In (0.02 atom %),[442] P (0.16 atom %),[443] As (0.18 atom %),[444] and Sb (0.035 atom %) in Ge have been reported in literature. The composition for the doped Ge NPs with Al (0.51 atom %; 2.25×10^{20} cm^{-3}) and Ga (0.46 atom %; 2.03×10^{20} cm^{-3}) exceed the solid solubility at the synthesis temperature of 300 °C but not the overall solid solubility. All other compositions represent hyperdoping of Ge with incorporation of In (1.1 atom %; 4.85×10^{20} cm^{-3}), P (1.1 atom %; 4.85×10^{20} cm^{-3}), As (1.2 atom %, 5.3×10^{20} cm^{-3}), and Sb (1.4 atom %; 6.18×10^{20} cm^{-3}) exceeding the maximum solid solubility.[439] However, no free charge carriers are observed by optical absorption and EPR spectroscopy, which could be expected by the doping with group III and V atoms in Ge NPs as demonstrated in the literature for other semiconductors.[445,446] The absence of the expected effects has been attributed to a ligand bonding to the dopants at the surface and surface/bulk defects according to the authors. Another explanation of the absence of the aforementioned effects could be a low effectiveness in the actual incorporation in the Ge lattice and accumulation at the surface since no in depth structural/chemical characterization has been carried out.[439] Nevertheless, superlattice films were cast from capped NPs after an exchange of surfactants demonstrated improved conductivities up to 10^{-3} $S \cdot cm^{-1}$, illustrating suitability for electronic devices.

Gas phase plasma synthesis of P hyperdoped Ge NPs by the decomposition of PH_3 and germane precursors under a H_2/Ar atmosphere has been reported.[447] According to ICP-MS measurements, the determined P content of 0.9−4.8 atom % (3.97×10^{20} cm^{-3}−2.12×10^{21} cm^{-3}) is always exceeding the maximum solid solubility of 0.16 atom % (7.06×10^{19} cm^{-3}) P in Ge according to the phase diagram.[443] The dopant activation efficiency is very low in the range of $4-6 \times 10^{-4}$ for activated dopants when relating the P content to the electrical data from transfer measurements using NP-based thin film samples. An additional protective Al_2O_3 coating applied by ALD in order to passivate surface defects improves these values; however, the highest activation efficiency is still very low at 2.7×10^{-3} and decreases for higher P levels.[447]

Ge nanocrystals in the size range 5−12 nm have been hyperdoped with up to 2 atom % (8.83×10^{20} cm^{-3}) Bi in a microwave-assisted solution-based approach,[448] which significantly exceeds the maximum solid solubility of 1.6×10^{-4} atom % (7.06×10^{16} cm^{-3}) Bi in Ge.[449] A strong indication for the successful incorporation of Bi in the Ge lattice is the shift of Ge reflections toward smaller 2θ values in XRD analyses. Additionally, resistance measurements on films obtained by Bi hyperdoped Ge NPs show increased conductivity values, which has been assigned to additional free charge carriers and lowering of the bandgap energies by incorporation of Bi in the Ge lattice.[448]

https://dx.doi.org/10.1021/acs.chemmater.9b04471
Chem. Mater. 2020, 32, 2703−2741

2.2.1.2.2. Solid Solutions of Transition Metals in Ge NPs. The incorporation of transition metals in the Ge semiconductor to form $Ge_{1-x}M_x$ has been predominantly an attempt to prepare dilute magnetic semiconductors based on group IV. DMS materials are interesting due to their uniqueness in exhibiting spin-dependent magneto-electro-optical properties including an electric field control of the ferromagnetic transition.[450] The anticipated outcome of preparing substitutional solid solutions is based on the fact that the transition elements occupying substitutional sites help to enhance the spin-dependent transport, which in turn increase both the magnetization and the Curie temperature of the semiconductor system.[451]

The incorporation of germanide forming transition metals including Ni, Co, Mn, and Cu has been described in a similar solution-based study as the Bi incorporation using a borohydride as the reducing agent and Ge halides as well as transition metal halides as precursors.[452] The conductivities increased the most for Ni doped Ge NPs, which showed the largest measured conductivities of 2.98×10^{-8} S·cm^{-1} and 10.37×10^{-8} S·cm^{-1} in the 2.05 atom % (9.05×10^{20} cm^{-3}) and 6.71 atom % (2.96×10^{21} cm^{-3}) Ni samples, while annealing of the particle based films used for the electronic measurements improved the overall conductivity. The incorporation of the metallic transition metals evidently affected the optical absorption and emission of the materials showing red shifts in the Tauc plots and PL emission. However, clustering and inhomogeneities should not be ruled out when the elemental maps are considered even though no indications are observed in the XRD pattern. In addition, the successful formation of $Ge_{0.95}Mn_{0.05}$ NPs on single crystalline Si substrates has been described via MBE synthesis at low temperatures showing ferromagnetism at low temperatures that cannot be attributed to other alloy phases;[450,453] however, a large number of reports show rather a spinoidal decomposition and the formation of defined Ge_yMn_z alloy phases.[450,454] Given the very low solid solubility of Mn in Ge of $\sim 10^{-6}$ atom %, these compositions are clearly metastable.[455] Similarly, $Ge_{0.98}Fe_{0.02}$ NPs on Si surfaces have been prepared showing ferromagnetism up to ~130 °C, while the synthesis temperature during MBE growth is reported to be 450 °C.[456]

2.2.1.2.3. NPs of $Ge_{1-x}Sn_x$ Solid Solutions. The formation of solid solutions of Ge with high amounts of Sn to alter the materials properties is an interesting field of research as described above. In order to achieve this goal of preparing the metastable composition required to obtain a direct bandgap material, vapor- and solution-based approaches have been applied. Due to the direct bandgap nature of the binary semiconductor, theoretical studies predicted efficient nanoscale light sources from epitaxially grown $Ge_{1-x}Sn_x$ NPs on Ge or Si substrates.[457,458] The growth of $Ge_{1-x}Sn_x$ NPs with sizes below 10 nm and Sn contents close of 12−15 atom % on thin silica/Si layers by MBE containing a Ge NP seed layer has been described.[459] The noteworthy pseudomorphic growth on Si leads to strain relaxation in upper layers and an absence of misfit dislocations, which indicates efficient dilatation in the small $Ge_{1-x}Sn_x$ NPs, while the contact to the Si substrate is enabled through pinholes in the silica layer. Besides the lattice spacing in the TEM images, no distinct determination of the Sn content or physical properties has been presented. These structures have been investigated by scanning tunneling spectroscopy (STM) and size-dependent separation between the valence and the conduction bands has been observed for particles in the range of 5−35 nm.[460] The larger $Ge_{1-x}Sn_x$ NPs exhibit a band offset of ~0.56 eV, which is close to an expected bulk value for this material composition. In addition, STM-photoabsorption spectroscopy on single NPs confirms the data obtained from STM.[461] The influence of Sn composition in such $Ge_{1-x}Sn_x$ NPs covered with a protective Si layer on the PL is negligible in terms of the peak shift upon higher alloying levels since all spectra show peak values at ~0.8 eV.[462] The study demonstrated that radiative defects in the Si layer are responsible for the PL signals in these structures with no/minor effect of the $Ge_{1-x}Sn_x$ material. The latest results on the direct growth of $Ge_{1-x}Sn_x$ NPs on single crystal surfaces demonstrated a successful conversion of Sn particles to form epitaxially grown $Ge_{1-x}Sn_x$ NPs.[463] However, no further physical properties of these structures are reported to date.

Another strategy is the formation of $Ge_{1-x}Sn_x$ NPs in a Ge-based matrix by thermal annealing of $Ge_{1-x}Sn_x$ thin films leading to phase segregation which yields Sn-rich precipitates.[464,465] The resulting $Ge_{1-x}Sn_x$ NPs are described to exhibit a Sn content of up to 50−80 atom % according to TEM analysis and the corresponding FFTs.[464] In addition, a diffusion of excess Sn in a thin amorphous $Ge_{0.98}Sn_{0.02}$ layer forming NPs of ~5 nm with 13.6 atom % Sn according to TEM and Raman spectroscopy has been reported.[466] The nucleation of the $Ge_{0.87}Sn_{0.13}$ NPs from the amorphous $Ge_{0.98}Sn_{0.02}$ layer is attributed to lowering of the overall Gibbs free energy upon incorporation of Sn in a forming crystal.

Alternatively, the bottom-up direct growth of big $Ge_{1-x}Sn_x$ NPs on the tips of Si nanorods has been described.[467−469] However, high temperature annealing leads to Sn segregation on the surface and generally a low Sn content in the crystal.[467] A slight increase in Sn content to 1.4 atom % shifts the PL signal of the direct transition from 0.8 eV for pure Ge to 0.72 eV.[469] Sn enrichment in the top layer by segregation was capped by another Ge coating leading to the observation of a low energy emission at ~0.55 eV at low temperatures.[468] It should be noted that the Si nanopillars are also emitting close to this value due to radiative defects in Si, and therefore assigning this emission to $Ge_{1-x}Sn_x$ is not possible beyond a doubt.

Pure $Ge_{1-x}Sn_x$ NPs are produced by the laser-induced reaction of tetramethyl germanium and tetramethyl tin resulting in Sn contents up to 40 atom %.[436] For higher Sn contents the forming $Ge_{1-x}Sn_x$ NPs are accompanied by metallic β-Sn according to XRD data. These Sn/$Ge_{1-x}Sn_x$ heterostructures have shown some promise for Li ion battery anodes in terms of cycle stability and capacity retention, but a determination of their semiconducting properties has not been reported.

The most prominent synthesis methods for $Ge_{1-x}Sn_x$ NPs are solution-based.[466,470−474] The presence of the reducing agent which includes primary amine functions on the high-boiling solvent as well as Li-organyles or hydrides and surface-active agents stabilizing the nanocrystals is vital for a successful synthesis. In a typical approach, Ge and Sn precursors, including group IV amides and/or halides, are mixed with high-boiling solvents at temperatures of approximately 300 °C to initiate a batch reaction that is often supported by a metathesis reaction using butyllithium.[471,472] The obtained $Ge_{1-x}Sn_x$ NP sizes depend on the growth duration, temperature, and concentration of the precursors. Thus, very small NPs in the range 1.5−2.2 nm[475] or 3.3−5.9 nm[473] have been

https://dx.doi.org/10.1021/acs.chemmater.9b04471
Chem. Mater. 2020, 32, 2703−2741

prepared with different compositions and Sn contents up to 23.6 atom %.[473] Slightly bigger $Ge_{1-x}Sn_x$ NPs have been described to contain up to 42 atom % Sn,[471] while a very recent report illustrates the accessibility of the whole composition range x = 0−0.95 for 7−16 nm NPs (Figure 10).[470] The incorporation of Sn in the Ge crystal lattice has

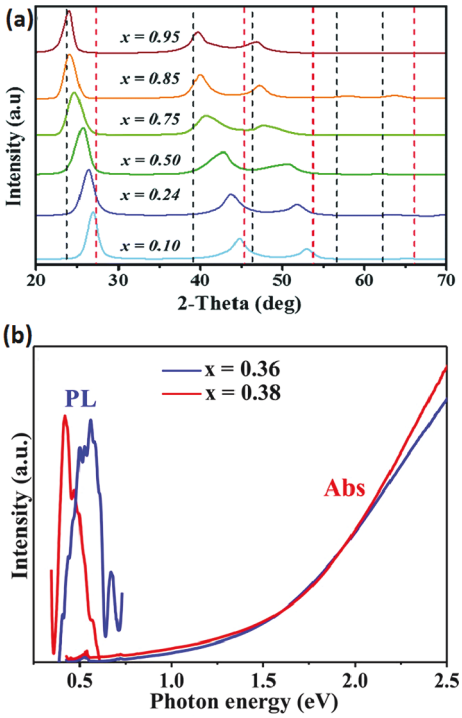

Figure 10. (a) XRD patterns of $Ge_{1-x}Sn_x$ NCs with x between 0.10 and 0.95. The red and black dotted lines correspond to the positions of reflections related to pure *dc*-Ge and *α*-Sn.[470] Reproduced from ref 470 with permission. Copyright 2019 The Royal Society of Chemistry. (b) PL and corresponding absorption spectra (normalized linear scales) of 10 nm $Ge_{1-x}Sn_x$ NCs.[471] Reprinted with permission from ref 471. Copyright 2015 American Chemical Society.

been confirmed by complementary methods including XRD, Raman spectroscopy, and scanning transmission electron microscopy energy-dispersive X-ray analysis (STEM-EDX). Especially XRD is a simple but yet powerful analysis method, because Vegard's law can be applied to the unstrained $Ge_{1-x}Sn_x$ system without requiring correction with a bowing factor.[476]

Another intriguing synthesis is based on the conversion of presynthesized *β*-Sn NPs reacting with Ge halogenides.[466] The *β*-Sn particle can be converted to $Ge_{1-x}Sn_x$ NPs with x = 0.18−0.62. Rising reaction temperature and time of annealing increases the Ge content in the binary alloy. Phase pure $Ge_{1-x}Sn_x$ has been observed for Sn contents below 27 atom % with this methodology. The retention of the NP diameter and changes in chemical composition are indications of a reduction−oxidation reaction leading to the formation of $Ge_{1-x}Sn_x$ NPs via diffusion, which is a thermodynamically ruled process and should in theory not lead to the metastable $Ge_{1-x}Sn_x$ alloy. This is a strong indication that this process is not as simple as it appears at first glance. Moreover, the indirect nature of the bandgap and the location of the absorption does not support the formation of high quality $Ge_{1-x}Sn_x$ crystals. Similarly, the conversion of pure Sn to form $Ge_{1-x}Sn_x$ nanorods with Sn contents in the range of 15−28 atom % has also been reported in a solution-based process.[477] In contrast, a similar procedure using Sn NPs as the source and thermal decomposition of Ge silylamide as the precursor leads to heterodimers with merely 4.3 atom % Sn incorporated in the Ge segment.[474]

Considering calculated bandgaps and thin film data for $Ge_{1-x}Sn_x$, most of the bandgaps of the respective NP systems determined from absorption data are quite high. To date, no report has described bulk values, which could be expected for the emission of $Ge_{1-x}Sn_x$ NPs with particle sizes > 10 nm (Table 3). Since quantum effects are dominating the

Table 3. Comparison of Published Absorption and Emission Energies Related to Size and Sn Content in $Ge_{1-x}Sn_x$ and Data Reported for Pure Ge NPs for Comparison

composition (atom % Sn in $Ge_{1-x}Sn_x$)	particle size [nm]	absorption onset/ optical bandgap (A = absorption; T = Tauc plots) [eV]	emission [eV]	ref
27−18	11.4	0.51−0.72 (T; indirect)		466
42−10	9	0.77−0.84 (T; indirect)		471
10	11.6−7.7	0.72−0.93 (T; indirect)	0.45−0.6 (broad, weak)	471
38−36				471
11.6−3.3	4.6−4.1	0.95−1.53 (T; direct)/ 0.75−1.23 (T; indirect)		472
23.6−18	3−2	1.56−2.05 (A)	1.72−2.00	478
23.6−5.5	3−1		1.7−1.9	475
20.6−1.5	6−3			473
9.1−1.5		0.84−1.72		473
5.6−1.5			1.32−1.62	473
$Ge_{0.986}Sb_{0.014}$	3.7	1.3 (T; indirect)		439
$Ge_{0.988}As_{0.012}$	3.7	1.3 (T; indirect)		439
$Ge_{0.989}In_{0.011}$	4.1	1.3 (T; indirect)		439
dc-Ge	3.8	1.3 (T; indirect)	∼1.03 broad, weak)	439
dc-Ge	5.4−1.1		2.5−3.7	479
dc-Ge	11.3−2.3		0.7−1.6	480
dc-Ge	10.2; 6.8; 4.8		0.77; 0.93; 1.03	481
dc-Ge	5.3; 0.9		0.88; 1.54	482

theoretical values for small NPs with increasing importance of the actual NP's diameter in the sub 5 nm regime on the calculated bandgap. In addition, values for the $Ge_{1-x}Sn_x$ NPs are always doubtful when no pure Ge reference can be provided with the same surface functionalization and particle sizes.

Surface related factors, e.g., defects, should be considered for the interpretation of the optical properties for hyperdoped and metastable Ge-based NPs. For instance, considering the diminishing direct bandgap values upon increasing Sn content in $Ge_{1-x}Sn_x$, very small bandgap values should be expected for $Ge_{1-x}Sn_x$ NP compositions sufficient for a transition to a direct bandgap behavior in bulk film samples (>∼8.5−11 atom % Sn).[135−138,140] Thus far, only one report on $Ge_{1-x}Sn_x$ describes the emission spectra reasonably close to an expected range <∼0.55 eV, but with weak intensity and blue-shifted by >∼0.2 eV to emissions expected for this composition (Figure 10b).[471] Other reports present mostly absorption data indicative of indirect bandgaps above 0.55 eV, which in turn points toward an indirect bandgap material even though their nominal

https://dx.doi.org/10.1021/acs.chemmater.9b04471
Chem. Mater. 2020, 32, 2703−2741

composition is far beyond the critical Sn content.[466,472] In addition, high energy PL emission or absorption features are most certainly a recombination mechanism related to the influence of higher energy states being populated and/or defect/surface related emission.[483,484] As illustrated in Table 3, also data from pure *dc*-Ge show a broad range of reported emission energies; however, studies on Ge NPs excluding surface effects or ligand exchange on the surface demonstrate only a smaller effect on the bandgap, and size-related bandgap broadening does not exceed 1.6 eV.[480,481,485,486]

2.2.2. Ge Nanowires of Metastable Composition/Phase. 2.2.2.1. Stress Induced Phase Transformations for Segmented Allotropes in Ge NWs. The alteration of physical properties by the formation of anisotropic, metastable Ge-based structures can be divided into three categories, including template-assisted growth, the metal-supported formation by the simultaneous supply of atoms resulting in the metastable alloy, and the self-seeding, as general topics.

In order to synthesize hexagonal 2H-Ge NWs, a few successful approaches have been described in the literature resulting in segmented NWs containing cubic and hexagonal allotropes. Segments of hexagonal 2H-Ge have been obtained by a strain-induced martensitic phase transformation in Ge NWs under external shear stresses leading to quasi-periodic NW heterostructures of Ge polymorphs.[487,488] The strain applied perpendicular to the growth direction of the NWs causes sliding of lattice planes and forms sawtooth morphologies from former straight NWs (Figure 11a). The NWs are imaged in the $[110]_{3C}/[1\bar{2}10]_{2H}$ zone axis to illustrate the formation of the heterostructure beyond any doubts of formation of potential twinning superstructures. Both the *dc*-Ge (3C) and 2H-Ge are identified in high resolution STEM images (Figure 11b–d). The 2H-Ge phase does not convert back to the *dc* allotrope at temperatures below 500 °C, which simplifies the structural investigations where energy input has to be considered.[487] According to theoretical calculations the 2H-Ge should reveal a band offset of 0.32 eV while being a direct bandgap material.[489] For a $Si_{0.6}Ge_{0.4}$, which is close to the transition from the indirect to the direct semiconductor material by increasing the Ge content, a bandgap of 0.52 eV has been calculated, which is important since 2H-Si is an indirect bandgap material.[490] Unfortunately, no experimental evidence of a direct bandgap semiconductor behavior for these 2H-Ge segments formed by this strain related mechanism has been observed to date.

2.2.2.2. Template Assisted Growth. 2.2.2.2.1. 2H-Ge NWs on III–V Templates. A popular strategy for the growth of anisotropic nanostructures is the use of nanoscale templates such as GaP NWs as described above for the synthesis of GaP/2H-Si core–shell NWs.[335] These core–shell structures can be used for additional layer growth to create GaP/2H-Si/2H-$Si_{1-x}Ge_x$.[491] The maximum stoichiometry achieved for defect-free smooth layer thin film growth on NW substrates was at 77 atom % Ge, significantly above the predicted direct bandgap transition at 65 atom % Ge.[491] Bandgaps can be probed by PL and absorption studies; however, these analyses have proven to be nontrivial in terms of experiment and interpretation in NWs involving crystal structures not existing in the bulk.[492] The determination of bandgaps in 2H-Ge, 2H-Si, and 2H-$Si_{1-x}Ge_x$ appear to be particularly challenging, because merely theoretical optical studies are reported despite the availability of high quality NW samples.[491] Very recently these materials have been realized with compositions of the 2H-$Si_{1-x}Ge_x$ alloy

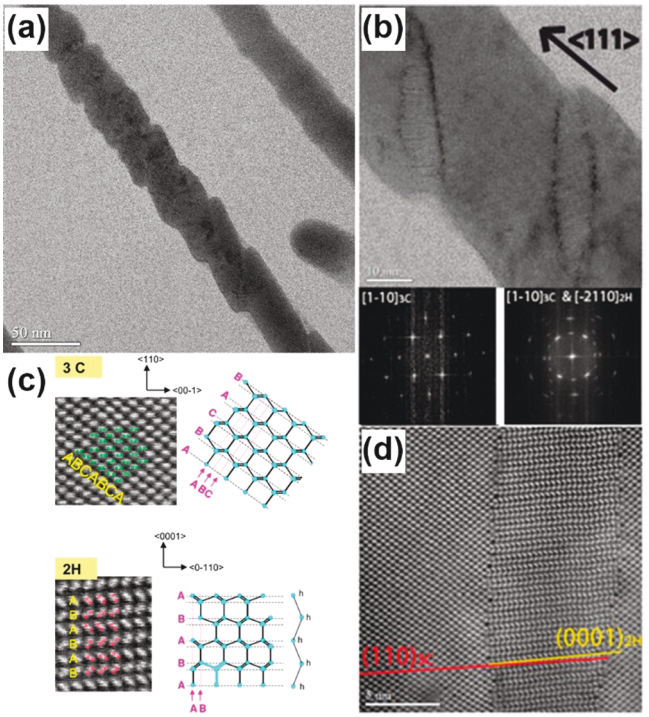

Figure 11. (a) TEM micrograph of a heterostructured Ge NW in a SiO_2 matrix showing a sawtooth shape with almost periodic steps. (b) High resolution bright-field STEM image of the heterostructured Ge NWs. The image is taken along a $[110]_{3C}$ zone axis. Allotrope domains are located at each alternating section. Fast Fourier transforms (FFT) are related to the micrograph subsections. New Bragg spots (on the right) with respect to the cubic matrix (on the left) are associated with the 2H phase. The individual FFT evidence the following relation between both phases: $[1\bar{1}0]_{3C}//[\bar{2}110]_{2H}$ and $(110)_{3C}//(0001)_{2H}$. (c) Enlarged views of nanodomains shown in (d) (with the same orientations evidenced by the orthogonal spatial system) and the sketch of the stacking sequence respectively for 3C (*dc*) and 2H polytypes. (d) HAADF-STEM image of one nanodomain showing the 2H phase with an ABABA stacking sequence.[487] Reprinted with permission from ref 487. Copyright 2014 American Chemical Society.

in the range $x = 0.65–1.0$. The first PL signals have been recorded for GaAs/2H-$Si_{1-x}Ge_x$ and GaAs/2H-Ge core/shell NWs[323,493] revealing tunable, direct bandgap materials in the energy range 0.3–0.7 eV. This is a very significant finding since the optical properties are comparable with III/V semiconductors, and thus applications including optical interconnect in computing,[494] optical sensing,[495] and silicon-based quantum photonic circuits[496] can be envisioned.[497]

2.2.2.2.2. NWs of $Ge_{1-x}Sn_x$ Solid Solutions via Templates. Besides the growth of the 2H-Ge allotrope, template approaches can be used for the growth of Ge/$Ge_{1-x}Sn_x$ core–shell NWs (Figure 12a,b).[498,499] In these processes, the simultaneous supply of Ge and Sn by the decomposition of precursors in a metal organic CVD process results in the epitaxial growth of $Ge_{1-x}Sn_x$ on the sidewalls of preformed *dc*-Ge NW templates with diameters of 20–50 nm. The obtained core–shell Ge/$Ge_{1-x}Sn_x$ NWs exhibit Sn contents up to 13 atom % Sn in a composition gradient along the layer (112)-oriented facets, while the ⟨110⟩-oriented sections contain merely <5 atom % Sn (Figure 12c,d).[498] These resulting star-striped patterns in NW cross sections have also been observed for core–shell structures containing lower Sn contents.[499] An

https://dx.doi.org/10.1021/acs.chemmater.9b04471
Chem. Mater. 2020, 32, 2703–2741

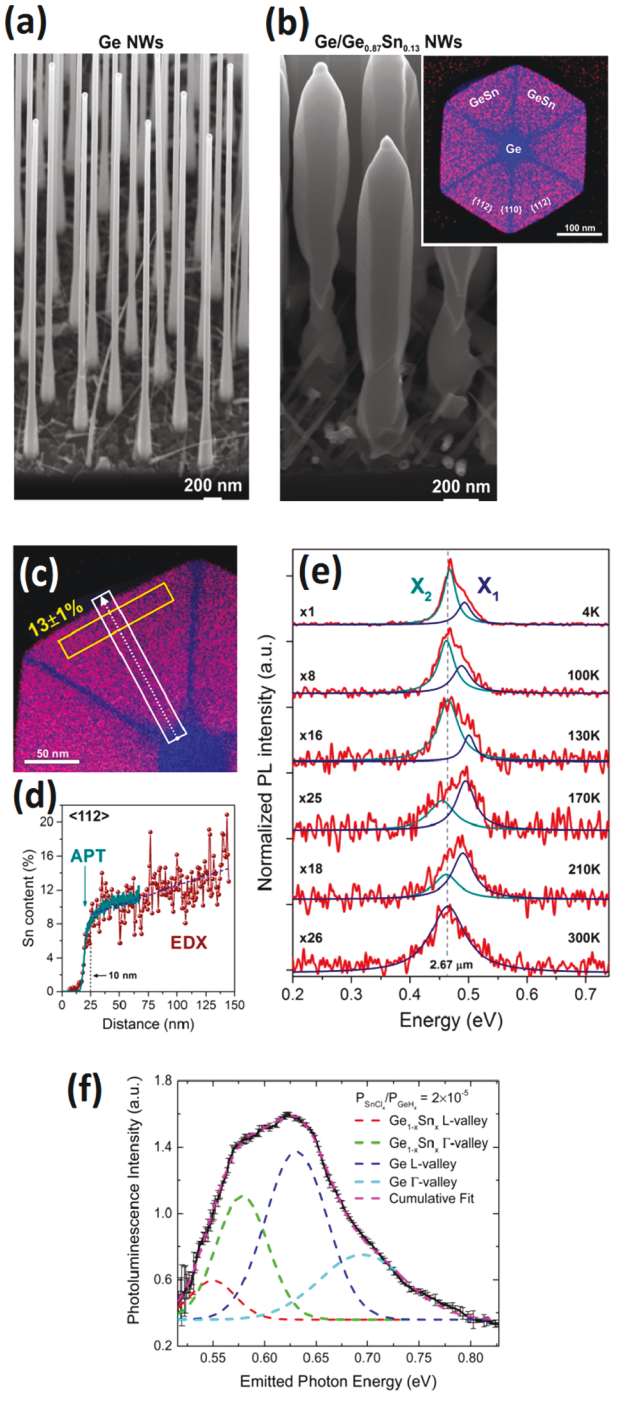

Figure 12. SEM picture of (a) the *dc*-Ge NW template and (b) Ge/$Ge_{0.87}Sn_{0.13}$ core/shell NW arrays (tilting angle 30°). Cross-sectional EDX compositional maps showing an ∼120 nm thick $Ge_{1-x}Sn_x$ shell, with enhanced Sn incorporation on the {112} side -facets compared to {110}. (c) The integrated tangential composition profile in the yellow rectangle provides an average Sn content of 13 ± 1 atom %, while the radial line profile (white dashed arrow) is shown in (d). (e) PL spectra of Ge/$Ge_{0.87}Sn_{0.13}$ core/shell NWs in the temperature range 4−300 K. Measurements are performed using an excitation power density of 8 W/cm^2.[498] (a−e) Reprinted with permission from ref 498. Copyright 2017 American Chemical Society. (f) PL peak fitting and deconvolution for core−shell Ge/$Ge_{0.96}Sn_{0.04}$ NWs at 60.0 kW cm^{-2} pump fluence showing signals from the Ge substrate and $Ge_{0.96}Sn_{0.04}$ shell.[499] Reprinted with permission from ref 499. Copyright 2016 American Chemical Society.

explanation for the strain-related formation of the star−stripe pattern and straining of the *dc*-Ge NW core has been provided by theoretical calculations, which also consider changes in shell formation upon increases in Ge NW diameter.[500,501] Synthesized Ge/$Ge_{0.87}Sn_{0.13}$ heterostructures show emission with direct bandgap characteristics at room temperature and a strong enhancement of light absorption. The reported emission maximum of 0.46 eV (Figure 12e) is in good agreement with theoretical and experimental results for Ge/$Ge_{0.87}Sn_{0.13}$ thin films and illustrates the formation of a direct bandgap material.[498,502] Sn contents below the concentration for a direct−indirect transition show multiple transitions in the PL spectra, which can be related to the direct and indirect bandgaps in the shell material as well as a strained Ge NW core (Figure 12f).[499] Changes in the precursor ratio has a large effect on the growth kinetics and affect the composition and morphology of the $Ge_{1-x}Sn_x$ shell.[503] Under a higher precursor concentration a transition from the prior described hexagonal cross section to a dodecahedral morphology can be observed with the (112)-oriented facets revealing still a higher Sn content than the (110)-oriented surfaces. However, assigning the surfaces to the described growth directions from the cross sections is based on simplifications since pronounced faceting of these surfaces along the NW axis can be observed in the SEM images. The shells grown with the highest Sn precursor ratio do not show any PL signals, which could be related to a decrease in crystal quality and/or the presence of segregated, metallic Sn. The location of emission maxima can be related to strain effects and increased Sn content with counteracting effects, while significant quenching has been observed when the temperature for the PL acquisition is raised to 100 K. This effect indcates the limited optical properties of these core/shell NWs when compared to the previously described core−shell NWs on thin Ge NWs and lower Sn content.[498,503]

2.2.2.3. In Situ Impurity Incorporation via Inert Growth Promoter. 2.2.2.3.1. Ge NW Hyperdoped with Groups III and V and Mn via Inert Seeds. As already mentioned before, metal-supported growth of anisotropic nanostructures is a viable approach. Potential metallic growth promoters for metastable Ge NWs must show a binary phase diagram with the absence of germanides at the chosen synthesis temperature and melt at moderate temperature. In this subsection, the formation of binary alloy NWs *via* a classic VLS mechanism based on an inert growth seed acting as a collector, growth promoter, and nucleation vessel is described.

Manganese incorporation in the Ge semiconductor to form $Ge_{1-x}Mn_x$ is an approach to prepare dilute magnetic semiconductor based Ge as shortly described *vide supra*.[504] The incorporation of significant Mn contents of up to 1 atom % in the Ge lattice without the formation of generally known Ge_yMn_z alloy phases has been demonstrated using Au growth promoters in SFLS synthesis.[505] Both precursors have been supplied in a constant precursor feed solution for the simultaneous thermal decomposition allowing the incorporation between 0.3 and 1 atom % Mn in the $Ge_{1-x}Mn_x$[505,506] and thus exceeding the solubility limit of $\sim 10^{-6}$ atom % by several orders of magnitude.[455] These nanostructures showed ferromagnetic behavior above room temperature as desired for a dilute magnetic semiconductor for electronics and spintronics applications. Similarly, the evaporation of the metallic constituents is described to form such $Ge_{0.92}Mn_{0.08}$ NWs without the formation of another phase using Au seeds.[507]

https://dx.doi.org/10.1021/acs.chemmater.9b04471
Chem. Mater. 2020, 32, 2703−2741

Hyperdoping with nonmetallic elements has been demonstrated using Au-seeded Ge NW growth using diborane and phosphine as additional gaseous sources.[359] The concentration of heteroatoms has been determined by SIMS revealing the incorporation of 0.45 atom % (2×10^{20} cm^{-3}) P and 0.52 atom % (2.3×10^{20} cm^{-3}) B. Even though signatures for a successful incorporation on substitutional sites, such as a shift in the Raman signal and a shift in the XRD pattern, have been observed, no data on the electronic properties of the hyperdoped Ge NWs have been reported. Therefore, no indication of the electrically active dopant concentration exists for such high dopant levels.

2.2.2.3.2. NWs of $Ge_{1-x}Sn_x$ Solid Solutions Using Inert Seeds. Initial experiments showing the CVD synthesis of $Ge_{1-x}Sn_x$ alloy NWs using an inert growth promoter by the VLS mechanism is based on Au as well as $Au_{0.90}Ag_{0.10}$ NPs.[508] The simultaneous decomposition of Ge and Sn precursors provides the components for the binary semiconductor similar to thin film CVD approaches. $Ge_{1-x}Sn_x$ NWs with Sn contents up to 9.2 atom % have been grown at temperatures of 440 °C and an additional postgrowth annealing at 230 °C was described to provide the best results and highest Sn contents. However, thermodynamic considerations and experimental results showing metal-induced degradation of $Ge_{1-x}Sn_x$ dependent on composition and temperature should not lead to the incorporation of higher Sn contents upon annealing of a crystalline $Ge_{1-x}Sn_x$ NW.[477] The Sn incorporation is ascribed to the high step velocity and thus impurity/heteroatom trapping during the crystal growth. The growth seed composition has been described to influence the Sn incorporation with a maximum of 9.2 atom % Sn in the Ge crystal lattice for $Au_{0.80}Ag_{0.20}$ growth seeds.[509] A follow-up study demonstrates that the $Au_{1-x}Ag_x$ alloy seeds also allow the direct formation of $Ge_{0.91}Sn_{0.09}$ NWs, which has been ascribed to accelerated growth rates.[509] The use of an alternative Sn precursor with higher decomposition rate can lead to branched $Ge_{1-x}Sn_x$ NWs with larger diameter stems growing from $Au_{0.80}Ag_{0.20}$ and branches forming by self-seeding from Sn particles.[510] Interestingly, the thicker stems contain only 4 atom % Sn, while the thin self-seeded branches incorporated 8 atom %. A definite explanation for the Sn NP formation on the sidewalls has not been provided, but accumulation/precipitation and migration of Sn droplets from the $Au_{1-x}Ag_x$ seed was suggested to be the most likely mechanism. The material revealed similar capacities and cyclability to *dc*-Ge NWs when used as anodes in Li-ion batteries.[510−512] Unfortunately, no optical data are described in the literature for these branched $Ge_{1-x}Sn_x$ NWs.

In addition, Au-catalyzed growth of $Ge_{1-x}Sn_x$ NWs with specific orientation on substrates has been reported.[513] Although the temperature used in the first report is in the regime (300−350 °C) where efficient Sn incorporation has been demonstrated for layer growth,[150] the Ge NWs contain only the thermodynamically stable ∼1 atom % Sn and reveal a Sn−O-enriched shell.[513] Alloying Sn with Au prior to NW growth has been the latest development in the growth of $Ge_{1-x}Sn_x$ NWs using an inert growth promoter and simplified process condition by using only one gaseous Ge source.[514] The $Ge_{1-x}Sn_x$ NWs show Sn gradients along the $Ge_{1-x}Sn_x$ NWs as can be expected when large lattice mismatch between the growing material and the substrate has to be overcome and the forming crystal can accommodate stress by compositional variation. However, the reported 5 atom % Sn is significantly below the indirect−direct bandgap semiconductor transition in $Ge_{1-x}Sn_x$, but in the upmost region this value increases to 7.3 atom % for the most efficient parameters described in the study.[514] According to the study, the Sn content is dependent on the initial composition of the growth seeds increasing from 1.3 atom %, 2.2 atom %, and 5 atom % of Sn in $Ge_{1-x}Sn_x$ NWs by using 61 atom %, 76 atom %, and 86 atom % of Sn in the binary Au/Sn seeding layer. In addition, the predominant growth direction of the $Ge_{1-x}Sn_x$ NWs changes from ⟨111⟩ to ⟨110⟩ when the Sn content increases in the seeds.[514] This is rather surprising since pure Sn as self-seeding NPs allows the growth of $Ge_{1-x}Sn_x$ NWs with higher Sn content while growing epitaxially along the ⟨111⟩ axis, which will be discussed in more detail in the following section.[515] It is clear that such trends require more validation and comparison with studies showing different Sn contents and preferred crystal orientation including the analysis of growth parameters, precursor decomposition kinetics, *etc.*

2.2.2.4. Self-Seeding of Metastable Ge-Based NWs. 2.2.2.4.1. Approaches to Ge NWs Hyperdoped with In and Ga. Self-seeding of NW growth refers to a metallic particle acting as both a nucleation/crystal growth promoter, and at the same time the metal is intentionally incorporated in the forming NW to form a binary compound.[239,240] For the low temperature formation of metastable, Ge-based NWs, the list of potential growth promoters can be narrowed down to low melting metals including Bi, Ga, Hg, In, Pb, and Sn as well as alloys thereof to enable the VLS growth of the material at moderate temperature.

An approach to grow Ge microwires and NWs at unusually low temperatures (i.e., < 100 °C) involves the use of liquid metals as electrodes. Low melting point metal nanodroplets (e.g., Ga, In, and Bi) can perform two functions simultaneously if they are connected to a current collector. As cathodes for electrodeposition, they can supply electrons at the liquid metal/liquid electrolyte interface to reduce a dissolved oxidized precursor. For example, GeO_2 is moderately soluble in alkaline solutions as a monomeric species[516] that can be reduced to Ge.[517] However, unlike conventional solid electrodes, such liquid metal nanodroplets can also serve as solvent media for the dissolution and crystal growth of Ge (Figure 13a).[518−523] In this way, a hybrid process known as electrochemical liquid−liquid−solid crystal growth (ec-LLS) that conceptually merges electrodeposition and VLS together is possible.[524] The principal advantages afforded by ec-LLS are the low temperature and the use of an electrochemical, rather than thermal, stimulus to dictate crystal growth. Extraordinarily high concentrations of the employed liquid metals, well beyond thermodynamic solubilities and up to 10 atom % (4.41×10^{21} cm^{-3}) Ga,[519] 6 atom % (2.65×10^{21} cm^{-3}) In,[522] and 3 atom % (1.32×10^{21} cm^{-3}) Bi[522] are possible via the ec-LLS strategy. For some liquid metals, the extensive incorporation results in a shrinking liquid volume during growth and imparts a noticeable taper (Figure 13b). For other liquid metal alloys, the nanowire/microwire morphology shows much less tapering (Figure 13b). Nevertheless, the prevailing measurements suggest the amount of liquid metal atoms that incorporate into the microwire and NWs grown by ec-LLS is variable. Precisely how the metal incorporates in the as-grown Ge, e.g., in lattice sites as substitutional dopants, in nonregular lattice sites, or as clusters/occlusions, depends strongly on the synthetic conditions. The lowest resistivity values obtained from two-contact measurements of numerous Ge microwires

https://dx.doi.org/10.1021/acs.chemmater.9b04471
Chem. Mater. 2020, 32, 2703−2741

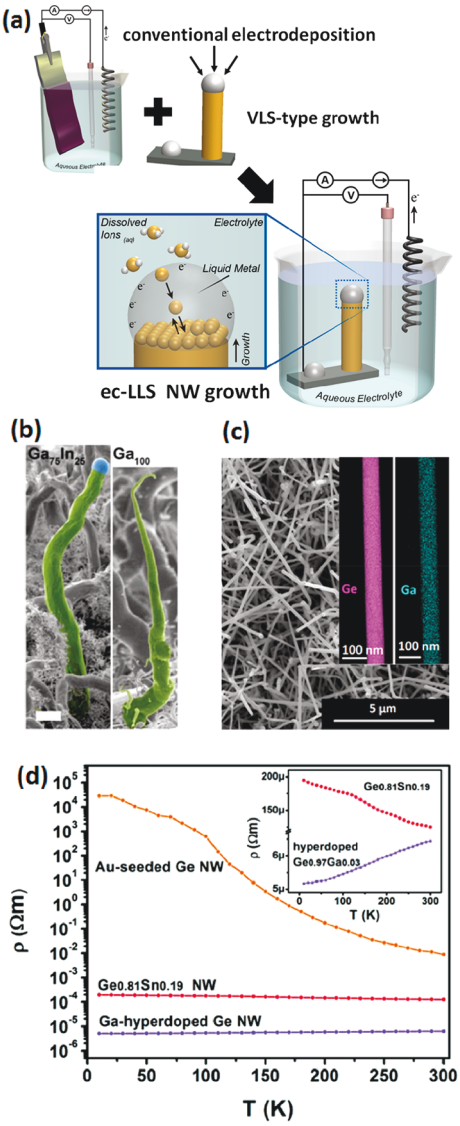

Figure 13. (a) Schematic depiction of the initial three-electrode electrochemical cell setup used for Ge NW and microwire growth by the ec-LLS method. The proposed ec-LLS growth mechanism contains electrochemical reduction of dissolved $HGeO_3^-$(aq) ions to Ge(s), which dissolves in the liquid metal until supersaturation induces nucleation and concomitant heterogeneous crystal growth. (b) Tilted scanning electron micrographs of Ge microwires grown from $Ga_{1-x}In_x$ (75% Ga and 25% In by weight) and pure Ga electrodes. The scale bar represents 10 μm.[519] Reprinted with permission from ref 519. Copyright 2015 American Chemical Society. (c) SEM image of Ge NWs grown by Ga seeding at 210 °C and STEM-EDX mapping for Ga and Ge of a NW.[357] Adapted from ref 357 by Seifner et al., licensed under CC BY 4.0 (https://creativecommons.org/licenses/by/4.0/). Published 2018 by the American Chemical Scoiety. (d) Resistivity changes with temperature in the range 298−10 K for Ga-hyperdoped Ge NWs compared to intrinsic Au-seeded Ge NWs and $Ge_{0.81}Sn_{0.19}$ NWs. While the $Ge_{0.81}Sn_{0.19}$ NW shows semiconductor behavior, the hyperdoped Ge reveals quasi-metallic transport characteristics.[525] Reprinted from ref 525 by Sistani et al., licensed under CC BY 3.0 (https://creativecommons.org/licenses/by/3.0/). Published 2018 by The Royal Society of Chemistry.

sampled across a dense film of microwires grown on degenerately doped Si[521] suggest Ga hyperdoping with an active dopant concentration of ~6 × 10^{18} cm^{-3} (~10^{-2} atom %).atom %. In contrast, EDX and APT measurements on the same materials suggest significant additional metal incorporation in the range of 8−10 atom %, implying a low efficiency of incorporating the liquid metal as dopants during ec-LLS.[521] Optical measurements on separate Ge NWs grown by ec-LLS with In showed 0.14 atom % (~6.18 × 10^{19} cm^{-3}), corresponding to a notably higher level of active dopants.[518] In these NWs, the resistivity and associated electrically active In content was inferred not from direct electrical measurements but rather from the blue-shift of optical absorbance. It is presently unclear whether this discrepancy reflects a difference in the growth mechanisms caused by the change from Ga to In, the specific ec-LLS conditions that were employed (e.g., temperature), or the measurement technique. Still, the cumulative data strongly hint that doping estimates from just conductivity measurements could be biased by the crystallographic properties (e.g., twinning defects, grain boundaries) of high aspect materials produced *via* the ec-LLS mechanism.[522] Accordingly, the utility of and possibilities for ec-LLS as a self-seeding synthetic route for hyperdoped Ge and possibly Si[397] NWs is still nascent.

Similarly, the incorporation of In can be achieved in a solution-based process via the thermal decomposition of an oligogermane precursor in the presence of In NPs at low temperatures down to 180 °C.[526] In this study up to 2 atom % (8.83 × 10^{20} cm^{-3}) In can be incorporated in the highly curled/kinked Ge NWs, which is often a sign of an accumulation of defects. Elemental mapping or APT has not been reported, and therefore the distribution/localization of In in the NWs remains unknown. Moreover, highly Ga doped Ge nanorods have been grown in a batch reaction via the SLS mechanism at temperatures down to 170 °C, illustrating the catalytic activity of metallic Ga by lowering the decomposition temperature of the Ge precursor by ~60 °C.[527] Ga NPs form *in situ* by the thermal decomposition of a Ga precursor and are subsequently supersaturated by Ge initiating the growth of the Ge nanorods. STEM-EDX and laser-assisted inductively coupled plasma mass spectrometry (LA-ICP-MS) have been used as complementary methods to determine the Ga incorporation efficiency in the Ge nanostructure to be ~2.3 et al. atom % (1.0 × 10^{21} cm^{-3}).[527]

Ga self-seeding by the VLS-based CVD approach can be used for the synthesis of Ge NWs with an average Ga content of ~3.5 atom % (1.55 × 10^{21} cm^{-3}) according to STEM-EDX analyses (Figure 13c).[357] The increased Ga content could be associated with an increased growth rate. A dense mesh of highly crystalline NWs formed at low temperatures of 210−230 °C, while containing a homogeneous distribution of Ga within the Ge matrix. As expected for a metastable material, thermal annealing at elevated temperatures results in the formation of thermodynamically stable products and thus Ga segregation has been observed after annealing at temperatures of 400 °C. The electronic properties of the hyperdoped material are determined by I−V measurements on single NW devices showing resistivity of ~3 × 10^{-4} Ω·cm representing an eelectrically active dopant concentration of ~1.5 atom % (6.62 × 10^{20} cm^{-3}) (Figure 13d). In addition, the Ga-hyperdoped Ge NWs reveal metal-like behavior in temperature dependent resistivity evolution. Two growth regimes in the Ga-seeded Ge NW growth have been determined, changing the growth temperature.[528] The high efficiency of Ga incorporation has been observed at temperatures below 350 °C with Ga contents in the ~3.8 atom % range, while higher growth temperatures of

https://dx.doi.org/10.1021/acs.chemmater.9b04471
Chem. Mater. 2020, 32, 2703−2741

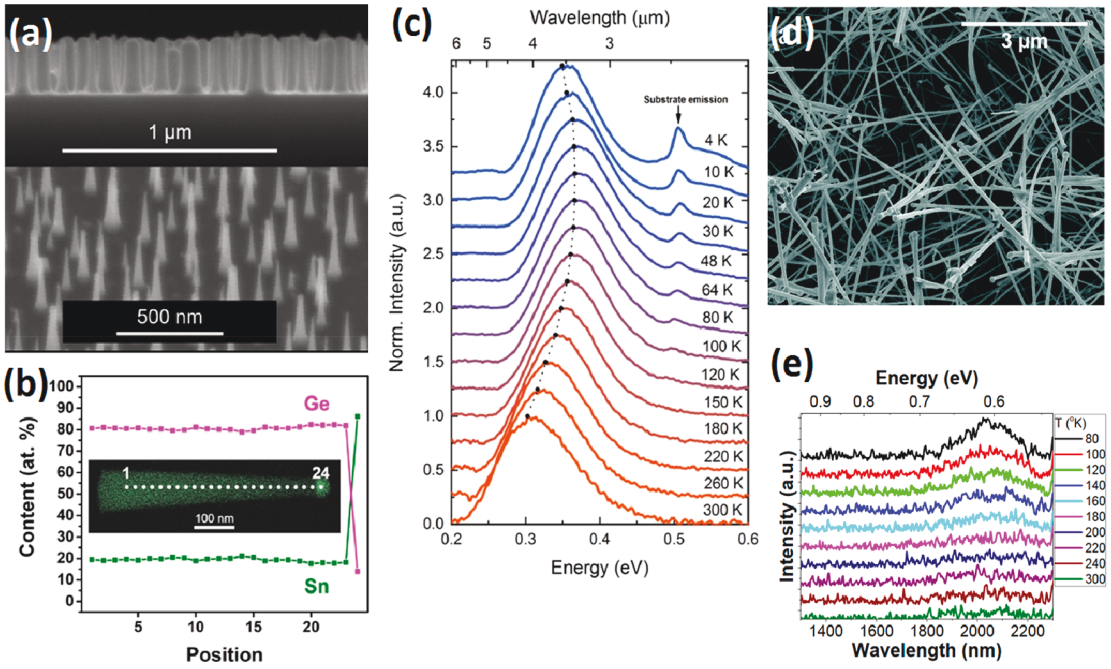

Figure 14. Cross section (a) of highly oriented $Ge_{1-x}Sn_x$ nanostructures grown on Ge(111) substrates and subsequent reactive ion etching. The 30° tilted view shows fully terminated $Ge_{1-x}Sn_x$ NWs grown perpendicular to the Ge surface, while the perfect perpendicular orientation is illustrated in the 90° view. (b) STEM-EDX maps showing the local Sn distribution without clustering. The graph illustrates the homogeneous Sn distribution along a $Ge_{1-x}Sn_x$ NW (19.3 ± 0.9 atom %), which was mechanically removed from the substrate and transferred to the TEM grid. (c) Spectra of the temperature dependence of the PL emission at an excitation density of 5.4 kW/cm^2. The peaks of the spectra are indicated with black dots, and the feature at ∼0.5 eV is an artifact of the Sb doped Ge substrate.[515] (a−c) Reprinted with permission from ref 515. Copyright 2019 American Chemical Society. (d) SEM image of $Ge_{0.91}Sn_{0.09}$ NWs grown using $Au_{0.80}Ag_{0.20}$ NPs. (e) Temperature dependent PL studies convey of the $Ge_{1-x}Sn_x$ NWs with 9.1 atom % Sn.[509] (d, e) Reproduced from ref 509 with permission. Copyright 2018 the Royal Society of Chemistry.

390 °C lead to Ge NWs without Ga incorporation according to STEM-EDX analyses. Small Ga concentrations below the detection limit of STEM-EDX would result in p-type behavior of the produced NWs, which has not been observed in the electronic measurements using single NW devices. The high temperature Ga-seeded Ge NWs showed a typical behavior of intrinsic Ge, which cannot be fully explained yet. Models describing the self-cleaning of semiconductor nanocrystals and associated doping limits depending on the crystal size usually refer to diameters below 5 nm and, thus, much smaller than the NW diameter of ∼20 nm.[529,530]

2.2.2.4.2. NWs of $Ge_{1-x}Sn_x$ Solid Solutions by Self-Seeding. Besides the self-seeding using group III metals leading to hyperdoping, the formation of metastable $Ge_{1-x}Sn_x$ alloy NWs from Sn seeds is an elegant approach. Sn as a type B growth promoter has been described for Ge NW[531,532] synthesis as well as axial Ge/Si heterostructures.[533−535] The incorporation efficiency described in these reports, if even mentioned, is rather low, <∼4 atom % Sn in Ge, but also exceeds the solid solubility.[531,532] Indeed, the first report on the bottom-up growth of metastable $Ge_{1-x}Sn_x$ NWs with Sn growth promoters contains 17−19 atom % Sn.[536] Thus, self-seeding by Sn particles results in $Ge_{1-x}Sn_x$ exceeding the indirect-to-direct semiconductor transition limit of ∼8.5−11 atom % Sn.[135−138,140] The thermal decomposition of a mixture of homo- and heterometallic imides by microwave synthesis results in the formation of $Ge_{1-x}Sn_x$ NWs with a Sn particle at the growth front.[536,537] Lowering the synthesis temperature to 140 °C increases the Sn content up to 28 atom % in $Ge_{1-x}Sn_x$ nanorods.[477] The crystal growth of these $Ge_{0.72}Sn_{0.28}$ nanorods is also supported by a templating effect of α-Sn NP seeds identified at the initial nucleation site, while for $Ge_{0.81}Sn_{0.19}$ NW growth at ∼230 °C no α-Sn has been observed. The Sn distribution and content determined by STEM-EDX confirm the homogeneous distribution in the $Ge_{1-x}Sn_x$ segment.[477] In addition, Sn contents determined by the EDX analyses and calculations based on the lattice expansion from XRD data using Vegard's law show excellent agreement. Thermal stability of the $Ge_{1-x}Sn_x$ NWs and nanorods has been investigated by *in situ* XRD measurements showing an increase in thermal stability with decreasing Sn content and destabilization in the presence of metallic Sn. Most strikingly, the degradation of $Ge_{0.72}Sn_{0.28}$ starts already at temperatures far below the melting point of Sn. *In situ* TEM investigations revealed the diffusion of solid Sn within the boundaries of $Ge_{0.72}Sn_{0.28}$ nanorods at temperatures below 200 °C. The driving force of this process has been assigned to a gain of lattice energy when metastable $Ge_{1-x}Sn_x$ dissolves in the diffusing solid Sn while subsequently redeposition of metastable $Ge_{1-y}Sn_y$ ($x > y$) occurs in the trace of the Sn section.[477] Direct bandgaps of 0.29 eV for $Ge_{0.72}Sn_{0.28}$ NRs and 0.40 eV for $Ge_{0.83}Sn_{0.17}$ NWs have been determined from absorption measurements using Tauc plots, showing the expected decrease in bandgap energy with higher Sn content. In addition, the electronic properties have been determined for $Ge_{0.81}Sn_{0.19}$ NWs by performing $I-V$ measurements on single NW devices.[527] Compared to intrinsic, Au-seeded Ge NWs, $Ge_{0.81}Sn_{0.19}$ NWs exhibited the typical behavior of a semiconductor but with resistivity values in the range of $\sim 1 \times 10^{-4}$ Ω m. The associated conductivity was thus several orders of magnitude higher than that of intrinsic Ge NWs (Figure 13d). This change can be attributed to alteration

https://dx.doi.org/10.1021/acs.chemmater.9b04471
Chem. Mater. 2020, 32, 2703−2741

of charge carrier mobilities upon Sn incorporation in the Ge host lattice.[538]

Very recently, the Sn-supported formation of epitaxial $Ge_{0.81}Sn_{0.19}$ NWs by CVD synthesis has been reported (Figure 14a).[515] Prior to the $Ge_{1-x}Sn_x$ nanostructure growth by a self-seeded VLS mechanism at low temperatures of 300−350 °C the Sn seeds were deposited via CVD. Liquid metallic Sn seeds enabled the anisotropic crystal growth and acted as a sole source of Sn for the metastable $Ge_{1-x}Sn_x$ semiconductor material. The thermal stability of the $Ge_{0.81}Sn_{0.19}$ NWs at these temperatures required short growth cycles.[477] The lattice mismatch between the Ge single crystal substrate and the variability of the $Ge_{1-x}Sn_x$ composition caused a short compositional transition zone of <100 nm length between a constant composition of the $Ge_{1-x}Sn_x$ NW (Figure 14b) and the Ge substrate. Efficient control over orientation and composition has been achieved for small initial dimensions of the Sn seeds with diameters in the range of ∼100 nm. Temperature- and laser power-dependent PL analyses verify the formation of a direct bandgap material, while the emission properties are constant at the whole substrate. The emission in the mid-IR region is observed as expected for unstrained $Ge_{0.81}Sn_{0.19}$ with a bandgap of 0.3 eV at room temperature and 0.37 eV at low temperatures.[515] The optical properties including the temperature-dependent trends in bandgap energy are comparable with results of high quality thin films.[22,150,160] This is a significant step forward since $Ge_{0.91}Sn_{0.09}$ NWs of prior studies showed only rather weak PL emission at low temperature and essentially no emission above 180 K,[509] while the epitaxially grown $Ge_{0.81}Sn_{0.19}$ NWs reveal a rather strong PL signal even at 300 K[515] (Figure 14c,e).

Self-seeding of in-plane $Ge_{1-x}Sn_x$ NWs on a substrate has been successfully demonstrated to incorporate up to 22 atom % Sn.[539] In this process, SnO_2 particles on a substrate are partially reduced by a H_2 plasma to form SnO_2/Sn heterodimers. Subsequently, an amorphous Ge coating has been applied, and the in-plane growth of $Ge_{0.78}Sn_{0.22}$ NWs is initiated by temperature increase above the melting temperature of Sn. The presence of SnO_2 for the nucleation of the in-plane nanostructure appears to be vital to prevent isotropic diffusion of Sn in the amorphous layer. The driving force for the solid−liquid−solid process is the gained lattice energy of the crystalline $Ge_{1-x}Sn_x$ alloy. The high Sn content, when compared to similar studies describing in-plane NW growth of $Ge_{1-x}Sn_x$ on Ge single crystals,[515,540] can be assigned to a thin SiO_2 layer on the Si substrate avoiding any epitaxial growth and associated strain effects on the growing binary alloy.[539]

The PL emissions of NWs and core−shell NWs are summarized in Table 4 depending on Ge allotrope and composition of the *dc*-$Ge_{1-x}Sn_x$. Since 2H-Si is an indirect gap semiconductor, alloying with large amounts of Ge will cause a transition to a direct bandgap semiconductor material.[491] However, only one group has reported the direct bandgap transition in the range of 0.3−0.7 eV in 2H-$Si_{1-x}Ge_x$ for x > 0.65 in very recent studies.[323,493]

Emission values for the thick $Ge_{0.87}Sn_{0.13}$ shell agree well with thin film data with similar composition and slight compressive strain including signal splitting at low temperatures due to the abrogation of degeneracy between heavy and light holes in the valence band.[140,498] Lower Sn content Ge/$Ge_{0.96}Sn_{0.04}$ core−shell NWs show four transitions fitted in a very broad emission, which are related to indirect and direct transitions in the $Ge_{0.96}Sn_{0.04}$ shell and also the Ge core. Signals

Table 4. Tabulated Emission Values for PL Studies on Metastable Ge-Based NWs

material	sample description	PL emission [eV]	temp [K]	ref
dc-Ge	bulk	0.66 (direct)		541
		0.80 (indirect)		
2H-Ge	calculated	0.32 (direct)		489
2H-$Si_{1-x}Ge_x$ with x = 1.0−0.65	2H-$Si_{1-x}Ge_x$ shell on GaAs NWs	0.3−0.7 (direct)	298	323
$Ge_{0.91}Sn_{0.09}$	NWs	0.55 (direct)	7	508
$Ge_{0.81}Sn_{0.19}$	NWs	0.30 (direct)	298	515
		0.37 (direct)	45	
Ge/$Ge_{0.87}Sn_{0.13}$	core−shell	0.47 (direct)	298	498
Ge/$Ge_{0.96}Sn_{0.04}$	$Ge_{0.96}Sn_{0.04}$ shell	0.55 (indirect)	298	499
		0.58 (direct)		
	strained Ge core	0.63 (indirect)		
		0.70 (direct)		
$Ge_{0.87}Sn_{0.13}$ thin film	compressive strain −0.41%	0.49 (direct)	4	140
		0.46 (direct)	298	
$Ge_{0.82}Sn_{0.18}$ triple layer film	compressive strain −1.3%	0.36 (direct)	298	160

at higher energy of 0.63 and 0.70 eV have been assigned to the Ge core material with a tensile strain of ∼0.5%,[499] as determined by exhibiting an ∼0.05 eV and ∼0.1 eV decrease in indirect-gap and direct-gap transition energies.[502] Lower energy features at 0.55 eV for the indirect and 0.58 eV for the direct bandgap transitions in the $Ge_{0.96}Sn_{0.04}$ shell can be observed showing the typical decreased difference between L and Γ energy levels before a direct bandgap material is finally obtained for higher Sn contents.[499,542] Similar effects have been predicted and are described in theoretical studies on similar core−shell structures.[500,501]

$Au_{1-x}Ag_x$-seeded $Ge_{0.91}Sn_{0.09}$ NWs show PL emission, which is limited to low temperature in the range of 7−180 K, with a very low signal-to-noise ratio at the higher temperatures considered (Figure 14e).[508,509] This could be indicative of a higher number of defects in the crystals leading to high recombination rates and thus quenching the radiative emission. In addition, the composition is very close to the minimum Sn content for the indirect−direct transition of the bandgap, and thus, minor local fluctuations could affect the emission properties significantly. In contrast, $Ge_{0.81}Sn_{0.19}$ NWs clearly show significant PL at room temperature in the expected range for a $Ge_{1-x}Sn_x$ alloy with this composition.[515] No peak splitting is observed, which would indicate strain effects. For instance, strain effects could be related to the two emission maxima described for thin films (overall thickness 380 nm) of comparable $Ge_{0.82}Sn_{0.18}$ composition with compressive strain of 1.3% prepared by sequential layer growth[160] that could be a result of heavy and light hole spitting.[140] Moreover, compressive strain will shift the PL emission to higher energies than expected for a relaxed material with the same

https://dx.doi.org/10.1021/acs.chemmater.9b04471
Chem. Mater. 2020, 32, 2703−2741

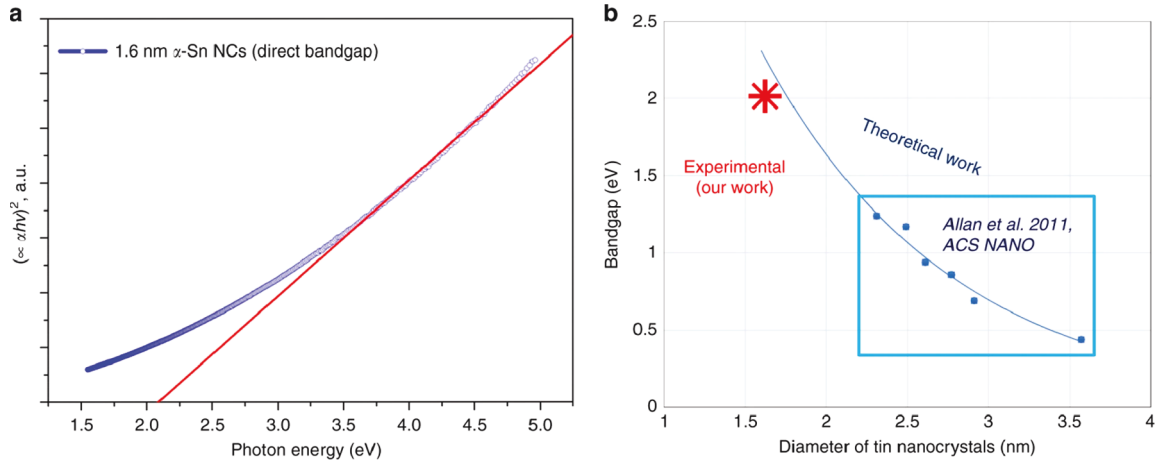

Figure 15. (a) Tauc plot for direct semiconductors of 1.6 nm α-Sn NPs and linear fit which estimates the bandgap to be 2.2 eV. (b) Bandgap values (blue dots) for Sn NPs from theoretical calculations and fitted exponential curve (blue line) with diameter dependence due to quantum confinement induced bandgap widening in α-Sn NPs.[561] Reprinted from ref 561 by Haq et al., licensed under CC BY 4.0 (https://creativecommons.org/licenses/by/4.0/). Published 2019 by Springer Nature.

composition. The room temperature emission maximum of 0.30 eV for $Ge_{0.81}Sn_{0.19}$ NWs is red-shifted when compared to the one at 0.36 eV for the $Ge_{0.82}Sn_{0.18}$ thin film, illustrating further the effective strain relaxation in NWs. For increasing low excitation power, the emission peak shifts in the PL spectra indicating a band filling effect before band-to-band transition is observed which is a typical observation for $Ge_{1-x}Sn_x$. According to the PL data, only two reports (one core−shell and one free NWs)[498,515] describe crystal qualities comparable to the state-of-the-art observed in thin film growth studies.[140,160]

2.3. Sn-Based Metastable Nanostructures. Theoretical studies suggest nanostructured α-Sn as a potential candidate for nanoelectronics[543−550] as well as optoelectronics[551−555] due to the possibility of altering the electronic band structure of this zero-bandgap semiconductor via quantum confinement effects. According to the literature, quantum confinement in α-Sn nanostructures can be expected for structures below 10 nm, and thus conversion to a material with semiconducting behavior[548] and bandgap energies in the infrared region could be anticipated.[554] Moreover, quantum confinement effects strongly depend on the surface termination or functionalization that alters band bending.[548,549] Switching between the semiconductor and the semimetal state ought to be observable in a size regime that enables semiconductor−semimetal junctions in α-Sn NWs.[548] However, reports on the synthesis of α-Sn nanostructures which can be stabilized at ambient conditions and even higher temperatures are very limited.

2.3.1. α-Sn Nanoparticles. The synthesis of α-Sn NPs has been realized by the intentional thermally induced phase segregation using $Si_{1-x}Sn_x$[556,557] and $Si_{1-x-y}Sn_xC_y$[558,559] films epitaxially grown on a Si substrate via molecular-beam epitaxy (MBE). Detailed investigations on the enhanced stability and the driving force of α-Sn formation beyond 13.2 °C are performed on strained and partially relaxed epitaxial $Si_{0.95}Sn_{0.05}$ thin films with subsequent thermal annealing in the range of 900−950 °C. During the cooling down step, segregated liquid Sn solidifies to β-Sn or coexisting β-Sn and α-Sn, which is confirmed by electron microscopy studies. The isotype $Si_{1-x}Sn_x$ matrix is attributed as the driving force of α-Sn formation due to interface effects. However, the volume expansion during α-Sn crystallization leads to the pressure-induced formation of β-Sn due to the lower density of β-Sn when compared to α-Sn.[556] The effect of the crystalline matrix can be illustrated by the exclusive formation of β-Sn precipitate when similar segregation experiments are performed using Sn-rich SiO_2 as the starting material.[560] Moreover, the increased thermal stability of the α-Sn phase up to temperatures of approximately 200 °C has been attributed to tensile strain in the NP inclusions.[556]

Very recently a first report on the direct synthesis of α-Sn NPs by microplasma synthesis evaporating material from a β-Sn target has been published.[561] The experimental parameters allow the synthesis of different Sn NP sizes in the range between 1.6 and 6.1 nm. For larger NPs with diameter of ∼6.1 nm the β-Sn phase is observed, while the smallest 1.6 nm NPs crystallize exclusively in the α-Sn phase. In the diameter range of 2−3 nm both phases have been obtained. The optical bandgap of 2.2 eV for 1.6 nm α-Sn NPs has been estimated by using Tauc plots (Figure 15). This is in reasonable agreement with theoretical works with calculated values for larger diameters and extrapolated to lower diameters.[552] Further investigations are required to confirm the proposed size-dependent bandgap evolution of α-Sn upon downscaling to the lower nanometer regime.[554]

In addition, α-Sn is a potential candidate to act as an anode material for Li ion batteries due to the capability of storing high amounts of Li.[562−564] The electrochemical reaction of the monodisperse β-phase Sn NPs with Li and subsequent delithiation reveals the transition to the α-phase.[565] α-Sn NPs form crystalline intercalation compounds and retain their crystalline nature over repeated cycles, while β-Sn leads to predominantly amorphous alloys causing lower electrical conductivity of the anode material. Therefore, future research should focus on the prevention of Sn amorphization in Li ion batteries based on the Sn anode material. A possible approach to reach this goal is the controlled synthesis of Sn NPs with diameters in the low nanometer regime which could help to thermodynamically stabilize the α-Sn phase. Below the critical particle diameter of 17 nm the formation of α-Sn after extraction of Li at room temperature is favored.[566] Therefore, a synthesis route for the formation of monodisperse α-Sn NPs, research on the stabilization of α-Sn, and the prevention of the

https://dx.doi.org/10.1021/acs.chemmater.9b04471
Chem. Mater. 2020, 32, 2703−2741

formation of amorphous Sn would be of great interest for the Li ion battery research community.

2.3.2. α-Sn Nanowires. There are few reports of α-Sn NWs. α-Sn/SnO_2 core−shell NWs have been successfully synthesized by VLS using SnO as the precursor and Au as the growth promoter.[567] XRD analyses confirm the presence of the α-Sn phase and the rutile phase of SnO_2. Disproportion of SnO leads to metallic Sn, which can dissolve in Au and SnO_2 as a shell material covering the Sn core. Information concerning the aggregate state of the Sn core during growth is not provided in this study.[567] The thermal stability of an α-Sn NW with a diameter of 14 nm covered with an 8 nm thick SnO_2 shell has been investigated up to 700 °C by *in situ* TEM and electron diffraction. Degradation of the support at higher temperatures does not allow the determination of the melting temperature. The extraordinary high thermal stability of the α-Sn core has been attributed to the well-defined epitaxial interface between the Sn core and the SnO_2 shell, which has also been observed with a less pronounced effect for epitaxial thin films.[568,569] Although a plausible explanation for α-Sn growth is provided by the authors, the initiation of α-Sn growth and the stabilization of this phase by SnO nuclei, which is reported in an early study, has to be considered a factor.[570]

3. SUMMARY

This review gives a comprehensive overview of the state-of-the-art in research related to group IV nanostructures with metastable composition or crystal structure. The increased interest in this field of research is based on the possibility of tailoring basic semiconducting properties such as a transition from a direct to indirect semiconductor behavior through a crystal phase change (e.g., *dc*-Ge/2H-Ge) or by compositional tuning, (e.g., $Ge_{1-x}Sn_x$ solid solutions). In addition, semiconductor-based plasmonics require a very high charge carrier density sparking interest in hyperdoped group IV NWs and NPs. Besides template effects enabling the growth of metastable phases by epitaxy, new synthesis strategies under conditions far from the thermodynamic equilibrium help to stabilize these materials in excellent purity and also in a controlled manner. For instance, a significant number of different metastable compositions, including hyperdoped materials/solid solutions, have been demonstrated for group IV NPs and NWs by nonequilibrium processing at low temperatures. However, the desired physical properties have been observed only in a limited number of reports, illustrating that significant improvement in the crystal quality and efficiency of dopant distribution/activation is required to harness the full potential of these nanomaterials. To date, the number of group IV allotropes in NPs and NWs is limited to 2H-Si, *bc8*-Si, *fcc*-Si, *r8*-Si, *st12*-Ge, 2H-Ge, and α-Sn. The recent advancements provide the basis for future research on this topic, and also potential use in new and transformative device concepts can be considered.

3.1. Perspectives. Further progress in the synthesis procedures and strategies for metastable materials in the NP or NW forms will broaden the fields of applications since the physical properties can be theoretically tailored for the envisioned purpose by composition and phase tuning. However, there is still significant progress required to understand and control how surfaces and interfaces can be produced in a pristine and reproducible manner. Similarly, the determination of "impurity" localization at substitutional sites or at interstitials is of outmost importance and will affect the properties and could be a reason for discrepancies in literature reports on similar compositions of the metastable nanomaterial in question.

Strategies to gain profound fundamental understanding of nanoscale properties should be based on the synergy between experiments and theory. For instance, recent discoveries on the kinetics of crystal formation and the influence of process parameters on crystal growth enabled by *in situ* methods[571−573] provide valuable new insight for the controlled growth of NWs. However, detailed characterization of the physical and structural properties using complementary methods[574] is vital to evaluate all potential deviations from an existing model describing the physical properties of a material. As a result, a deeper understanding of nanoscale properties and a minimization of misleading interpretations can be expected.

Unraveling some of the open questions will require the joint interdisciplinary efforts by chemists, surface scientists, physicists, and engineers to make progress on tuning the materials properties as well as controlling the processes to ensure knowledge transfer from a synthesis equipment on the lab scale, which are often home-built, to commercial reactors. Moreover, the understanding of processes and material properties will require the support of theory. In this context, the screening of extrinsic point defect properties in Si and Ge shown in the literature is a good example for the prediction of material properties, which helps to tailor a nanomaterial for a certain application.[575] Furthermore, a very powerful tool to predict materials with interesting physical properties is machine learning.[576−580] However, big data are required to get accurate extrapolations via machine learning, which again points out the importance of a detailed characterization of nanomaterials.

The most obvious field of applications of metastable group IV NWs and NPs will take advantage of the altered physical properties for electronic circuits or optoelectronic devices including nanoemitters and detectors. We would expect a significant impact of metastable materials in this area. Besides the well-established strain relaxation in NPs and NWs, the opportunities offered by metastable group IV NWs and NPs should have significant technological impact.

From a technological view, the opportunities in the area of bandgap engineering in semiconductors either by size or by composition in direct bandgap semiconductors, e.g., in 2H-$Si_{1-x}Ge_x$ or $Ge_{1-x}Sn_x$, offer tremendous potential of metastable group IV materials. In this respect, a combination of nanoelectronics with photonics has been identified as being a target for next generation of systems on a chip.[581,582] Therefore, nanoscale direct bandgap light emitter placement on conventional substrates that are based on Si technology will be required and should be achieved by progress in the direct growth of metastable group IV NWs and NPs on those substrates by combining different materials (composition or phase) with site selective growth strategies.[323,515,583,584] Furthermore, injection of a significant amount of charge carriers in group IV NPs or NWs by the incorporation of electrically active heteroatoms in the host lattice results in accessibility of mid-IR localized surface plasmon resonance effects,[290,585] which is also a promising approach to merge photonics and electronics at the nanoscale.[586]

On another note, flexible and/or stretchable devices for nanobio-applications, such as sensing, signal transducers, imaging, and drug delivery, could be envisioned since the group IV elements described herein have been described to

https://dx.doi.org/10.1021/acs.chemmater.9b04471
Chem. Mater. 2020, 32, 2703−2741

impose low cytotoxicity.[587] Thus, group IV NPs of metastable composition could be used for imaging in an additional biological window in the near-IR to mid-IR wavelength range. Such biological imaging can take advantage of either the specific transitions of the direct bandgap semiconductors[588,589] or the specific imaging contrast provided by the incorporation of metals in the crystal structure.[261] A wide range of different signals created by NPs can be used for imaging the human body. Inherent flaws of the imaging methods such as low penetration depth, limited resolution, sensitivity, *etc.* can hinder accurate diagnostics and make the use of multimodal agents very attractive.[590,591] Moreover, surface functionalization of Si and Ge are well established and can be applied to their hyperdoped counterparts, broadening the application portfolio to drug delivery or site-selective binding in specific locations of the body.[592]

In addition, bio-related applications envisioned for semiconductor NWs span from miniaturized elements of devices and circuits to ultrasensitive biosensors for diagnostics in wearable and integrated sensors;[593] however, the pristine properties of individual NW devices will have to be preserved.[594] The use of semiconductor NWs to interact with single cells while regulating and monitoring cellular activities by the ability to create bioelectric and/or biophotonic interfaces within cells may also suggest new avenues for biomedical research.[595,596]

■ ASSOCIATED CONTENT

Supporting Information

The Supporting Information is available free of charge at https://pubs.acs.org/doi/10.1021/acs.chemmater.9b04471.

Description and estimation of $Ge_{1-x}Sn_x$ phase evolution in the temperature range 300−505 K (PDF)

■ AUTHOR INFORMATION

Corresponding Author

Sven Barth − *Physikalisches Institut, Goethe-Universität Frankfurt, 60438 Frankfurt am Main, Germany;* orcid.org/0000-0003-3900-2487; Phone: +49 6979847261; Email: barth@physik.uni-frankfurt.de

Authors

Michael S. Seifner − *Centre for Analysis and Synthesis and NanoLund, Lund University, 22100 Lund, Sweden;* orcid.org/0000-0001-9101-5520

Stephen Maldonado − *Department of Chemistry, University of Michigan, Ann Arbor, Michigan 48109-1055, United States;* orcid.org/0000-0002-2917-4851

Complete contact information is available at: https://pubs.acs.org/10.1021/acs.chemmater.9b04471

Author Contributions

The manuscript was written through contributions of all authors. All authors have given approval to the final version of the manuscript.

Notes

The authors declare no competing financial interest.

■ ACKNOWLEDGMENTS

S.B. acknowledges funding by the Deutsche Forschungsgemeinschaft (DFG, German Research Foundation) in the Heisenberg Programme—413940754. In addition, S.B. thanks Prof. M. Huth, Prof. A. Terfort, and Prof. M. Wagner for their support at Goethe University Frankfurt. S.M. acknowledges generous financial support from the National Science Foundation (CHE-1807755).

■ REFERENCES

(1) Jariwala, D.; Sangwan, V. K.; Lauhon, L. J.; Marks, T. J.; Hersam, M. C. Carbon nanomaterials for Electronics, Optoelectronics, Photovoltaics, and Sensing. *Chem. Soc. Rev.* **2013**, *42* (7), 2824−60.

(2) Dai, L.; Chang, D. W.; Baek, J. B.; Lu, W. Carbon Nanomaterials for Advanced Energy Conversion and Storage. *Small* **2012**, *8* (8), 1130−66.

(3) Georgakilas, V.; Perman, J. A.; Tucek, J.; Zboril, R. Broad Family of Carbon Nanoallotropes: Classification, Chemistry, and Applications of Fullerenes, Carbon Dots, Nanotubes, Graphene, Nanodiamonds, and Combined Superstructures. *Chem. Rev.* **2015**, *115* (11), 4744−822.

(4) Popov, I. V.; Görne, A. L.; Tchougréeff, A. L.; Dronskowski, R. Relative Stability of Diamond and Graphite as Seen Through Bonds and Hybridizations. *Phys. Chem. Chem. Phys.* **2019**, *21* (21), 10961−10969.

(5) Bundy, F. P.; Kasper, J. S. Hexagonal Diamond - A New Form of Carbon. *J. Chem. Phys.* **1967**, *46* (9), 3437−3446.

(6) Guldi, D. M. Fullerenes: Three Dimensional Electron Acceptor Materials. *Chem. Commun.* **2000**, *5*, 321−327.

(7) Kroto, H. W.; Heath, J. R.; O'Brien, S. C.; Curl, R. F.; Smalley, R. E. C60: Buckminsterfullerene. *Nature* **1985**, *318* (6042), 162−163.

(8) Baughman, R. H.; Zakhidov, A. A.; de Heer, W. A. Carbon Nanotubes–the Route Toward Applications. *Science* **2002**, *297* (5582), 787−92.

(9) Dai, H. Carbon Nanotubes: Synthesis, Integration, and Properties. *Acc. Chem. Res.* **2002**, *35* (12), 1035−1044.

(10) Allen, M. J.; Tung, V. C.; Kaner, R. B. Honeycomb Carbon: a Review of Graphene. *Chem. Rev.* **2010**, *110* (1), 132−45.

(11) Katsnelson, M. I. Graphene: Carbon in Two Dimensions. *Mater. Today* **2007**, *10* (1−2), 20−27.

(12) Novoselov, K. S.; Fal'ko, V. I.; Colombo, L.; Gellert, P. R.; Schwab, M. G.; Kim, K. A Roadmap for Graphene. *Nature* **2012**, *490* (7419), 192−200.

(13) Diederich, F.; Kivala, M. All-Carbon Scaffolds by Rational Design. *Adv. Mater.* **2010**, *22* (7), 803−12.

(14) Li, Y.; Xu, L.; Liu, H.; Li, Y. Graphdiyne and Graphyne: from Theoretical Predictions to Practical Construction. *Chem. Soc. Rev.* **2014**, *43* (8), 2572−86.

(15) Peng, Q.; Dearden, A. K.; Crean, J.; Han, L.; Liu, S.; Wen, X.; De, S. New Materials Graphyne, Graphdiyne, Graphone, and Graphane: Review of Properties, Synthesis, and Application in Nanotechnology. *Nanotechnol., Sci. Appl.* **2014**, *7*, 1−29.

(16) Li, G.; Li, Y.; Liu, H.; Guo, Y.; Li, Y.; Zhu, D. Architecture of Graphdiyne Nanoscale Films. *Chem. Commun.* **2010**, *46* (19), 3256−8.

(17) Hsiao, W. W. W.; Hui, Y. Y.; Tsai, P. C.; Chang, H. C. Fluorescent Nanodiamond: A Versatile Tool for Long-Term Cell Tracking, Super-Resolution Imaging, and Nanoscale Temperature Sensing. *Acc. Chem. Res.* **2016**, *49* (3), 400−407.

(18) Mochalin, V. N.; Shenderova, O.; Ho, D.; Gogotsi, Y. The Properties and Applications of Nanodiamonds. *Nat. Nanotechnol.* **2012**, *7* (1), 11−23.

(19) Kaiser, K.; Scriven, L. M.; Schulz, F.; Gawel, P.; Gross, L.; Anderson, H. L. An sp-Hybridized Molecular Carbon Allotrope, Cyclo[18]Carbon. *Science* **2019**, *365* (6459), 1299−1301.

(20) Zhuang, J.; Xu, X.; Feng, H.; Li, Z.; Wang, X.; Du, Y. Honeycomb Silicon: a Review of Silicene. *Sci. Bull.* **2015**, *60* (18), 1551−1562.

(21) Dávila, M. E.; Xian, L.; Cahangirov, S.; Rubio, A.; Le Lay, G. Germanene: a Novel Two-Dimensional Germanium Allotrope akin to Graphene and Silicene. *New J. Phys.* **2014**, *16* (9), 095002.

(22) Wirths, S.; Buca, D.; Mantl, S. Si−Ge−Sn Alloys: From Growth to Applications. *Prog. Cryst. Growth Charact. Mater.* **2016**, *62* (1), 1−39.
(23) Zaima, S.; Nakatsuka, O.; Taoka, N.; Kurosawa, M.; Takeuchi, W.; Sakashita, M. Growth and Applications of GeSn-Related Group-IV Semiconductor Materials. *Sci. Technol. Adv. Mater.* **2015**, *16* (4), 043502.
(24) Kouvetakis, J.; Menendez, J.; Chizmeshya, A. V. G. Tin-Based Group IV Semiconductors: New Platforms for Opto- and Micro-electronics on Silicon. *Annu. Rev. Mater. Res.* **2006**, *36* (1), 497−554.
(25) Ronning, C.; Borschel, C.; Geburt, S.; Niepelt, R. Ion Beam Doping of Semiconductor Nanowires. *Mater. Sci. Eng., R* **2010**, *70* (3), 30−43.
(26) Kasper, E.; Oehme, M.; Lupaca-Schomber, J. High Ge Content SiGe alloys: Doping and Contact Formation. *ECS Trans* **2008**, *16*, 893−904.
(27) Ackland, G. J. High-Pressure Phases of Group IV and III-V Semiconductors. *Rep. Prog. Phys.* **2001**, *64* (4), 483−516.
(28) Katzke, H.; Tolédano, P. Structural Mechanisms of the High-Pressure Phase Transitions in the Elements of Group IVa. *J. Phys.: Condens. Matter* **2007**, *19* (27), 275204.
(29) Mujica, A.; Rubio, A.; Muñoz, A.; Needs, R. J. High-Pressure Phases of Group-IV, III−V, and II−VI Compounds. *Rev. Mod. Phys.* **2003**, *75* (3), 863−912.
(30) Wentorf, R. H.; Kasper, J. S. Two New Forms of Silicon. *Science* **1963**, *139* (3552), 338−339.
(31) Zhao, Y.-X.; Buehler, F.; Sites, J. R.; Spain, I. L. New Metastable Phases of Silicon. *Solid State Commun.* **1986**, *59* (10), 679−682.
(32) Crain, J.; Ackland, G. J.; Maclean, J. R.; Piltz, R. O.; Hatton, P. D.; Pawley, G. S. Reversible Pressure-Induced Structural Transitions Between Metastable Phases of Silicon. *Phys. Rev. B: Condens. Matter Mater. Phys.* **1994**, *50* (17), 13043−13046.
(33) Ruffell, S.; Haberl, B.; Koenig, S.; Bradby, J. E.; Williams, J. S. Annealing of Nanoindentation-Induced High Pressure Crystalline Phases Created in Crystalline and Amorphous Silicon. *J. Appl. Phys.* **2009**, *105* (9), 093513.
(34) Ruffell, S.; Bradby, J. E.; Williams, J. S.; Munroe, P. Formation and Growth of Nanoindentation-Induced High Ppressure Phases in Crystalline and Amorphous Silicon. *J. Appl. Phys.* **2007**, *102* (6), 063521.
(35) Kailer, A.; Nickel, K. G.; Gogotsi, Y. G. Raman Microspectroscopy of Nanocrystalline and Amorphous Phases in Hardness indentations. *J. Raman Spectrosc.* **1999**, *30* (10), 939−946.
(36) Domnich, V.; Gogotsi, Y.; Dub, S. Effect of Phase Transformations on the Shape of the Unloading Curve in the Nanoindentation of Silicon. *Appl. Phys. Lett.* **2000**, *76* (16), 2214−2216.
(37) Ge, D.; Domnich, V.; Gogotsi, Y. Thermal Stability of Metastable Silicon Phases Produced by Nanoindentation. *J. Appl. Phys.* **2004**, *95* (5), 2725−2731.
(38) Haberl, B.; Guthrie, M.; Sinogeikin, S. V.; Shen, G.; Williams, J. S.; Bradby, J. E. Thermal Evolution of the Metastable r8 and bc8 Polymorphs of Silicon. *High Pressure Res.* **2015**, *35* (2), 99−116.
(39) Liu, P. L.; Yen, R.; Bloembergen, N.; Hodgson, R. T. Picosecond Laser-Induced Melting and Resolidification Morphology on Si. *Appl. Phys. Lett.* **1979**, *34* (12), 864−866.
(40) Verburg, P. C.; Smillie, L. A.; Romer, G. R. B. E.; Haberl, B.; Bradby, J. E.; Williams, J. S.; Huis in 't Veld, A. J. Huis in 't Veld, A. J., Crystal Structure of Laser-Induced Subsurface Modifications in Si. *Appl. Phys. A: Mater. Sci. Process.* **2015**, *120* (2), 683−691.
(41) Al'tshuler, L. V. Use of Shock Waves in High-Pressure Physics. *Soviet Physics Uspekhi* **1965**, *8* (1), 52−91.
(42) Pavlovskii, M. N. Formation of Metallic Modifications of Germanium and Silicon under Shock Loading. *Soviet Physics Solid State* **1968**, *9* (11), 2514.
(43) Gilev, S. D.; Trubachev, A. M. Metallization of Silicon in a Shock Wave: the Metallization Threshold and Ultrahigh Defect Densities. *J. Phys.: Condens. Matter* **2004**, *16* (46), 8139−8153.
(44) Goto, T.; Sato, T.; Syono, Y. Reduction of Shear Strength and Phase-Transition in Shock-Loaded Silicon. *Jpn. J. Appl. Phys.* **1982**, *21* (Part 2, No. 6), L369−L371.
(45) Rapp, L.; Haberl, B.; Bradby, J. E.; Gamaly, E. G.; Williams, J. S.; Rode, A. V. Confined Micro-Explosion Induced by Ultrashort Laser Pulse at SiO_2/Si Interface. *Appl. Phys. A: Mater. Sci. Process.* **2014**, *114* (1), 33−43.
(46) Rapp, L.; Haberl, B.; Bradby, J. E.; Gamaly, E. G.; Williams, J. S.; Rode, A. V., Ultrafast Laser Induced Confined Microexplosion: A New Route to Form Super-Dense Material Phases. In *Fundamentals of Laser-Assisted Micro- and Nanotechnologies*; Veiko, V., Konov, V. I., Eds.; Springer: Cham, 2014; Vol. *195*, pp 3−26.
(47) Rapp, L.; Haberl, B.; Pickard, C. J.; Bradby, J. E.; Gamaly, E. G.; Williams, J. S.; Rode, A. V. Experimental Evidence of New Tetragonal Polymorphs of Silicon Formed Through Ultrafast Laser-Induced Confined Microexplosion. *Nat. Commun.* **2015**, *6*, 7555.
(48) Von Schnering, H.-G.; Schwarz, M.; Nesper, R. The Lithium Sodium Silicide Li_3NaSi_6 and the Formation of allo-Silicon. *J. Less-Common Met.* **1988**, *137* (1−2), 297−310.
(49) Gryko, J.; McMillan, P. F.; Marzke, R. F.; Ramachandran, G. K.; Patton, D.; Deb, S. K.; Sankey, O. F. Low-Density Framework Form of Crystalline Silicon with a wide Optical Band Gap. *Phys. Rev. B: Condens. Matter Mater. Phys.* **2000**, *62* (12), R7707−R7710.
(50) Ammar, A.; Cros, C.; Pouchard, M.; Jaussaud, N.; Bassat, J.-M.; Villeneuve, G.; Duttine, M.; Ménétrier, M.; Reny, E. On the Clathrate Form of Elemental Silicon, Si_{136}: Preparation and Characterisation of $Na_xSi_{136\ (x\rightarrow 0)}$. *Solid State Sci.* **2004**, *6* (5), 393−400.
(51) Kim, D. Y.; Stefanoski, S.; Kurakevych, O. O.; Strobel, T. A. Synthesis of an Open-Framework Allotrope of Silicon. *Nat. Mater.* **2015**, *14* (2), 169−73.
(52) Lalmi, B.; Oughaddou, H.; Enriquez, H.; Kara, A.; Vizzini, S.; Ealet, B.; Aufray, B. Epitaxial Growth of a Silicene Sheet. *Appl. Phys. Lett.* **2010**, *97* (22), 223109.
(53) Feng, B.; Ding, Z.; Meng, S.; Yao, Y.; He, X.; Cheng, P.; Chen, L.; Wu, K. Evidence of Silicene in Honeycomb Structures of Silicon on Ag(111). *Nano Lett.* **2012**, *12* (7), 3507−11.
(54) Jamgotchian, H.; Colignon, Y.; Hamzaoui, N.; Ealet, B.; Hoarau, J. Y.; Aufray, B.; Biberian, J. P. Growth of Silicene Layers on Ag(111): Unexpected Effect of the Substrate Temperature. *J. Phys.: Condens. Matter* **2012**, *24* (17), 172001.
(55) Lin, C.-L.; Arafune, R.; Kawahara, K.; Tsukahara, N.; Minamitani, E.; Kim, Y.; Takagi, N.; Kawai, M. Structure of Silicene Grown on Ag(111). *Appl. Phys. Express* **2012**, *5* (4), 045802.
(56) Vogt, P.; De Padova, P.; Quaresima, C.; Avila, J.; Frantzeskakis, E.; Asensio, M. C.; Resta, A.; Ealet, B.; Le Lay, G. Silicene: Compelling Experimental Evidence for Graphenelike Two-Dimensional Silicon. *Phys. Rev. Lett.* **2012**, *108* (15), 155501.
(57) Aufray, B.; Kara, A.; Vizzini, S.; Oughaddou, H.; Léandri, C.; Ealet, B.; Le Lay, G. Graphene-Like Silicon Nanoribbons on Ag(110): A possible Formation of Silicene. *Appl. Phys. Lett.* **2010**, *96* (18), 183102.
(58) De Padova, P.; Quaresima, C.; Ottaviani, C.; Sheverdyaeva, P. M.; Moras, P.; Carbone, C.; Topwal, D.; Olivieri, B.; Kara, A.; Oughaddou, H.; Aufray, B.; Le Lay, G. Evidence of Graphene-Like Electronic Signature in Silicene Nanoribbons. *Appl. Phys. Lett.* **2010**, *96* (26), 261905.
(59) Rachid Tchalala, M.; Enriquez, H.; Mayne, A. J.; Kara, A.; Roth, S.; Silly, M. G.; Bendounan, A.; Sirotti, F.; Greber, T.; Aufray, B.; Dujardin, G.; Ait Ali, M.; Oughaddou, H. Formation of One-Dimensional Self-Assembled Silicon Nanoribbons on Au(110)-(2 × 1). *Appl. Phys. Lett.* **2013**, *102* (8), 083107.
(60) Meng, L.; Wang, Y.; Zhang, L.; Du, S.; Wu, R.; Li, L.; Zhang, Y.; Li, G.; Zhou, H.; Hofer, W. A.; Gao, H. J. Buckled Silicene Formation on Ir(111). *Nano Lett.* **2013**, *13* (2), 685−90.
(61) Fleurence, A.; Friedlein, R.; Ozaki, T.; Kawai, H.; Wang, Y.; Yamada-Takamura, Y. Experimental Evidence for Epitaxial Silicene on Diboride Thin Films. *Phys. Rev. Lett.* **2012**, *108* (24), 245501.

https://dx.doi.org/10.1021/acs.chemmater.9b04471
Chem. Mater. 2020, 32, 2703−2741

(62) Jamieson, J. C. Crystal Structures at High Pressures of Metallic Modifications of Silicon and Germanium. *Science* **1963**, *139* (3556), 762−4.
(63) Olijnyk, H.; Sikka, S. K.; Holzapfel, W. B. Structural Phase Transitions in Si and Ge Under Pressures up to 50 GPa. *Phys. Lett. A* **1984**, *103* (3), 137−140.
(64) Menoni, C. S.; Hu, J. Z.; Spain, I. L. Germanium at High Pressures. *Phys. Rev. B: Condens. Matter Mater. Phys.* **1986**, *34* (1), 362−368.
(65) McMahon, M. I.; Nelmes, R. J.; Wright, N. G.; Allan, D. R. Pressure Dependence of the ImmaPhase of Silicon. *Phys. Rev. B: Condens. Matter Mater. Phys.* **1994**, *50* (2), 739−743.
(66) Hanfland, M.; Schwarz, U.; Syassen, K.; Takemura, K. Crystal Structure of the High-Pressure Phase Silicon VI. *Phys. Rev. Lett.* **1999**, *82* (6), 1197−1200.
(67) Duclos, S. J.; Vohra, Y. K.; Ruoff, A. L. Experimental Study of the Crystal Stability and Equation of State of Si to 248 GPa. *Phys. Rev. B: Condens. Matter Mater. Phys.* **1990**, *41* (17), 12021−12028.
(68) McMahon, M. I.; Nelmes, R. J. New High-Pressure Phase of Si. *Phys. Rev. B: Condens. Matter Mater. Phys.* **1993**, *47* (13), 8337−8340.
(69) Minomura, S.; Drickamer, H. G. Pressure Induced Phase Transitions in Silicon, Germanium and Some III−V Compounds. *J. Phys. Chem. Solids* **1962**, *23* (5), 451−456.
(70) Piltz, R. O.; Maclean, J. R.; Clark, S. J.; Ackland, G. J.; Hatton, P. D.; Crain, J. Structure and Properties of Silicon XII: A Complex Tetrahedrally Bonded Phase. *Phys. Rev. B: Condens. Matter Mater. Phys.* **1995**, *52* (6), 4072−4085.
(71) Besson, J. M.; Mokhtari, E. H.; Gonzalez, J.; Weill, G. Electrical Properties of Semimetallic Silicon III and Semiconductive Silicon IV at Ambient Pressure. *Phys. Rev. Lett.* **1987**, *59* (4), 473−476.
(72) Nelmes, R. J.; McMahon, M. I.; Wright, N. G.; Allan, D. R.; Loveday, J. S. Stability and Crystal Sstructure of BC8 Germanium. *Phys. Rev. B: Condens. Matter Mater. Phys.* **1993**, *48* (13), 9883−9886.
(73) Joannopoulos, J. D.; Cohen, M. L. Electronic Properties of Complex Crystalline and Amorphous Phases of Ge and Si. I. Density of States and Band Structures. *Phys. Rev. B* **1973**, *7* (6), 2644−2657.
(74) Persson, C.; Janzén, E. Electronic Band Structure in Hexagonal Close-Packed Si Polytypes. *J. Phys.: Condens. Matter* **1998**, *10* (47), 10549−10555.
(75) Raffy, C.; Furthmüller, J.; Bechstedt, F. Properties of Hexagonal Polytypes of Group-IV Elements From First-Principles Calculations. *Phys. Rev. B: Condens. Matter Mater. Phys.* **2002**, *66* (7), 075201.
(76) Pandolfi, S.; Renero-Lecuna, C.; Le Godec, Y.; Baptiste, B.; Menguy, N.; Lazzeri, M.; Gervais, C.; Spektor, K.; Crichton, W. A.; Kurakevych, O. O. Nature of Hexagonal Silicon Forming via High-Pressure Synthesis: Nanostructured Hexagonal 4H Polytype. *Nano Lett.* **2018**, *18* (9), 5989−5995.
(77) Amsler, M.; Botti, S.; Marques, M. A. L.; Lenosky, T. J.; Goedecker, S. Low-Density Silicon Allotropes for Photovoltaic Applications. *Phys. Rev. B: Condens. Matter Mater. Phys.* **2015**, *92* (1), 014101.
(78) Du, Y.; Zhuang, J.; Liu, H.; Xu, X.; Eilers, S.; Wu, K.; Cheng, P.; Zhao, J.; Pi, X.; See, K. W.; Peleckis, G.; Wang, X.; Dou, S. X. Tuning the Band Gap in Silicene by Oxidation. *ACS Nano* **2014**, *8* (10), 10019−25.
(79) Haberl, B.; Strobel, T. A.; Bradby, J. E. Pathways to Exotic Metastable Silicon Allotropes. *Appl. Phys. Rev.* **2016**, *3* (4), 040808.
(80) Molle, A.; Grazianetti, C.; Tao, L.; Taneja, D.; Alam, M. H.; Akinwande, D. Silicene, Silicene Derivatives, and Their Device Applications. *Chem. Soc. Rev.* **2018**, *47* (16), 6370−6387.
(81) Lew Yan Voon, L. C.; Zhu, J.; Schwingenschlögl, U. Silicene: Recent Theoretical Advances. *Appl. Phys. Rev.* **2016**, *3* (4), 040802.
(82) Nelmes, R. J.; Liu, H.; Belmonte, S. A.; Loveday, J. S.; McMahon, M. I.; Allan, D. R.; Hausermann, D.; Hanfland, M. Imma Phase of Germanium at ∼ 80 GPa. *Phys. Rev. B: Condens. Matter Mater. Phys.* **1996**, *53* (6), R2907−R2909.
(83) Takemura, K.; Schwarz, U.; Syassen, K.; Hanfland, M.; Christensen, N. E.; Novikov, D. L.; Loa, I. High-Pressure Cmca and hcp Phases of Germanium. *Phys. Rev. B: Condens. Matter Mater. Phys.* **2000**, *62* (16), R10603−R10606.
(84) Vohra, Y. K.; Brister, K. E.; Desgreniers, S.; Ruoff, A. L.; Chang, K. J.; Cohen, M. L. Phase Transition Studies of Germanium to 1.25 Mbar. *Phys. Rev. Lett.* **1986**, *56* (18), 1944−1947.
(85) Grüttner, A.; Nesper, R.; von Schnering, H. G. Novel Metastable Germanium Modifications allo-Ge and 4H-Ge from Li_7Ge_{12}. *Angew. Chem., Int. Ed. Engl.* **1982**, *21* (12), 912−913.
(86) Kiefer, F.; Karttunen, A. J.; Döblinger, M.; Fässler, T. F. Bulk Synthesis and Structure of a Microcrystalline Allotrope of Germanium (m-allo-Ge). *Chem. Mater.* **2011**, *23* (20), 4578−4586.
(87) Zaikina, J. V.; Muthuswamy, E.; Lilova, K. I.; Gibbs, Z. M.; Zeilinger, M.; Snyder, G. J.; Fässler, T. F.; Navrotsky, A.; Kauzlarich, S. M. Thermochemistry, Morphology, and Optical Characterization of Germanium Allotropes. *Chem. Mater.* **2014**, *26* (10), 3263−3271.
(88) Cros, C.; Pouchard, M.; Hagenmuller, P. Sur une Nouvelle Famille de Clathrates Minéraux Isotypes des Hydrates de Gaz et de Liquides. Interprétation des Résultats Obtenus. *J. Solid State Chem.* **1970**, *2* (4), 570−581.
(89) Guloy, A. M.; Ramlau, R.; Tang, Z.; Schnelle, W.; Baitinger, M.; Grin, Y. AvGuest-Free Germanium Clathrate. *Nature* **2006**, *443* (7109), 320−323.
(90) Fassler, T. F. Germanium (cF136): a new Crystalline Modification of Germanium with the Porous Clathrate-II Structure. *Angew. Chem., Int. Ed.* **2007**, *46* (15), 2572−5.
(91) Li, L.; Lu, S. Z.; Pan, J.; Qin, Z.; Wang, Y. Q.; Wang, Y.; Cao, G. Y.; Du, S.; Gao, H. J. Buckled Germanene Formation on Pt(111). *Adv. Mater.* **2014**, *26* (28), 4820−4.
(92) Derivaz, M.; Dentel, D.; Stephan, R.; Hanf, M. C.; Mehdaoui, A.; Sonnet, P.; Pirri, C. Continuous Germanene layer on Al(111). *Nano Lett.* **2015**, *15* (4), 2510−6.
(93) d'Acapito, F.; Torrengo, S.; Xenogiannopoulou, E.; Tsipas, P.; Marquez Velasco, J.; Tsoutsou, D.; Dimoulas, A. Evidence for Germanene Growth on Epitaxial Hexagonal (h)-AlN on Ag(111). *J. Phys.: Condens. Matter* **2016**, *28* (4), 045002.
(94) Zhang, L.; Bampoulis, P.; Rudenko, A. N.; Yao, Q.; van Houselt, A.; Poelsema, B.; Katsnelson, M. I.; Zandvliet, H. J. Structural and Electronic Properties of Germanene on MoS_2. *Phys. Rev. Lett.* **2016**, *116* (25), 256804.
(95) Acun, A.; Zhang, L.; Bampoulis, P.; Farmanbar, M.; van Houselt, A.; Rudenko, A. N.; Lingenfelder, M.; Brocks, G.; Poelsema, B.; Katsnelson, M. I.; Zandvliet, H. J. Germanene: the Germanium Analogue of Graphene. *J. Phys.: Condens. Matter* **2015**, *27* (44), 443002.
(96) Jayaraman, A.; Klement, W.; Kennedy, G. C. Melting and Polymorphism at High Pressures in Some Group IV Elements and III-V Compounds with the Diamond/Zincblende Structure. *Phys. Rev.* **1963**, *130* (2), 540−547.
(97) Brudevoll, T.; Citrin, D. S.; Cardona, M.; Christensen, N. E. Electronic Structure of α-Sn and its Dependence on Hydrostatic Strain. *Phys. Rev. B: Condens. Matter Mater. Phys.* **1993**, *48* (12), 8629−8635.
(98) Pedersen, T. G.; Fisker, C.; Jensen, R. V. S. Tight-Binding Parameterization of α-Sn Quasiparticle Band Structure. *J. Phys. Chem. Solids* **2010**, *71* (1), 18−23.
(99) Aguado, A. First-Principles Study of Elastic Properties and Pressure-Induced Phase Transitions of Sn: LDA versus GGA Results. *Phys. Rev. B: Condens. Matter Mater. Phys.* **2003**, *67* (21), 212104.
(100) Yu, C.; Liu, J.; Lu, H.; Chen, J. Ab Initio Calculation of the Properties and Pressure Induced Transition of Sn. *Solid State Commun.* **2006**, *140* (11−12), 538−543.
(101) Cheong, B. H.; Chang, K. J. First-Principles Study of the Structural Properties of Sn Under Pressure. *Phys. Rev. B: Condens. Matter Mater. Phys.* **1991**, *44* (9), 4103−4108.
(102) Ihm, J.; Cohen, M. L. Equilibrium Properties and the Phase Transition of Grey and White Tin. *Phys. Rev. B: Condens. Matter Mater. Phys.* **1981**, *23* (4), 1576−1579.
(103) Pavone, P.; Baroni, S.; de Gironcoli, S. $\alpha \leftrightarrow \beta$ Phase Transition in Tin: A Theoretical Study Based on Density-Functional

Perturbation Theory. *Phys. Rev. B: Condens. Matter Mater. Phys.* **1998**, *57* (17), 10421−10423.
(104) Na, S.-H. First-principles Study of Structural Phase Transition of Sn. *J. Korean Phys. Soc.* **2010**, *56* (1), 494−497.
(105) Barnett, J. D.; Bean, V. E.; Hall, H. T. X-Ray Diffraction Studies on Tin to 100 Kilobars. *J. Appl. Phys.* **1966**, *37* (2), 875.
(106) Olijnyk, H.; Holzapfel, W. B. Phase Transitions in Si, Ge and Sn Under Pressure. *Le Journal de Physique Colloques* **1984**, *45* (C8), C8-153−C8-156.
(107) Zhu, F.-f.; Chen, W.-j.; Xu, Y.; Gao, C.-l.; Guan, D.-d.; Liu, C.-h.; Qian, D.; Zhang, S.-C.; Jia, J.-f. Epitaxial Growth of Two-Dimensional Stanene. *Nat. Mater.* **2015**, *14* (10), 1020−1025.
(108) Deng, J.; Xia, B.; Ma, X.; Chen, H.; Shan, H.; Zhai, X.; Li, B.; Zhao, A.; Xu, Y.; Duan, W.; Zhang, S.-C.; Wang, B.; Hou, J. G. Epitaxial Growth of Ultraflat Stanene with Topological Band Inversion. *Nat. Mater.* **2018**, *17* (12), 1081−1086.
(109) Yuhara, J.; Fujii, Y.; Nishino, K.; Isobe, N.; Nakatake, M.; Xian, L.; Rubio, A.; Le Lay, G. Large area Planar Stanene Epitaxially Grown on Ag(1 1 1). *2D Mater.* **2018**, *5* (2), 025002.
(110) Maniraj, M.; Stadtmüller, B.; Jungkenn, D.; Düvel, M.; Emmerich, S.; Shi, W.; Stöckl, J.; Lyu, L.; Kollamana, J.; Wei, Z.; Jurenkow, A.; Jakobs, S.; Yan, B.; Steil, S.; Cinchetti, M.; Mathias, S.; Aeschlimann, M. A Case Study for the Formation of Stanene on a Metal Surface. *Commun. Phys.* **2019**, *2* (1), 12.
(111) Olesinski, R. W.; Abbaschian, G. J. The Ge−Si (Germanium-Silicon) System. *Bull. Alloy Phase Diagrams* **1984**, *5* (2), 180−183.
(112) Olesinski, R. W.; Abbaschian, G. J. The Ge−Sn (Germanium−Tin) System. *Bull. Alloy Phase Diagrams* **1984**, *5* (3), 265−271.
(113) Olesinski, R. W.; Abbaschian, G. J. The Si−Sn (Silicon−Tin) System. *Bull. Alloy Phase Diagrams* **1984**, *5* (3), 273−276.
(114) Ye, H.; Yu, J. Germanium Epitaxy on Silicon. *Sci. Technol. Adv. Mater.* **2014**, *15* (2), 024601.
(115) Currie, M. T.; Samavedam, S. B.; Langdo, T. A.; Leitz, C. W.; Fitzgerald, E. A. Controlling Threading Dislocation Densities in Ge on Si using Graded SiGe Layers and Chemical-Mechanical Polishing. *Appl. Phys. Lett.* **1998**, *72* (14), 1718−1720.
(116) Samavedam, S. B.; Currie, M. T.; Langdo, T. A.; Fitzgerald, E. A. High-Quality Germanium Photodiodes Integrated on Silicon Substrates Using Optimized Relaxed Graded Buffers. *Appl. Phys. Lett.* **1998**, *73* (15), 2125−2127.
(117) Kasper, E.; Herzog, H. J.; Kibbel, H. A One-Dimensional SiGe Superlattice Grown by UHV Epitaxy. *Appl. Phys.* **1975**, *8* (3), 199−205.
(118) Fitzgerald, E. A. Dislocations in Strained-Layer Epitaxy: Theory, Experiment, and Applications. *Mater. Sci. Rep.* **1991**, *7* (3), 87−142.
(119) Hartmann, J. M.; Abbadie, A.; Barnes, J. P.; Fédéli, J. M.; Billon, T.; Vivien, L. Impact of the H_2 Anneal on the Structural and Optical Properties of Thin and Thick Ge Layers on Si; Low Temperature Surface Passivation of Ge by Si. *J. Cryst. Growth* **2010**, *312* (4), 532−541.
(120) Yamamoto, Y.; Zaumseil, P.; Arguirov, T.; Kittler, M.; Tillack, B. Low Threading Dislocation Density Ge Deposited on Si (100) using RPCVD. *Solid-State Electron.* **2011**, *60* (1), 2−6.
(121) Fitzgerald, E. A. GeSi/Si Nanostructures. *Annu. Rev. Mater. Sci.* **1995**, *25* (1), 417−454.
(122) Kasper, E.; Oehme, M.; Lupaca-Schomber, J. High Ge Content SiGe alloys: Doping and Contact Formation. *ECS Trans.* **2008**, *16*, 893−904.
(123) Liu, J.; Pan, D.; Jongthammanurak, S.; Wada, K.; Kimerling, L. C.; Michel, J. Design of Monolithically Integrated GeSi Electro-Absorption Modulators and Photodetectors on a SOI Platform. *Opt. Express* **2007**, *15* (2), 623−8.
(124) Pillarisetty, R. Academic and Industry Research Progress in Germanium Nanodevices. *Nature* **2011**, *479* (7373), 324−8.
(125) Currie, M. T.; Leitz, C. W.; Langdo, T. A.; Taraschi, G.; Fitzgerald, E. A.; Antoniadis, D. A. Carrier Mobilities and Process Stability of Strained Si *n*- and *p*-MOSFETs on SiGe Virtual Substrates. *J. Vac. Sci. Technol., B: Microelectron. Process. Phenom.* **2001**, *19* (6), 2268−2279.
(126) Tezuka, T.; Sugiyama, N.; Takagi, S. Fabrication of Strained Si on an Ultrathin SiGe-on-Insulator Virtual Substrate with a High-Ge Fraction. *Appl. Phys. Lett.* **2001**, *79* (12), 1798−1800.
(127) Rim, K.; Chu, J.; Chen, H.; Jenkins, K. A.; Kanarsky, T.; Lee, K.; Mocuta, A.; Zhu, H.; Roy, R.; Newbury, J.; Ott, J.; Petrarca, K.; Mooney, P.; Lacey, D.; Koester, S.; Chan, K.; Boyd, D.; Ieong, M.; Wong, H. Characteristics and Device Design of Sub-100 nm Strained Si N- and PMOSFETs. *2002 Symposium on VLSI Technology. Digest of Technical Papers*, Cat. No.01CH37303; 11−13 June 2002; IEEE: 2002; pp 98−99.
(128) Lee, M. L.; Fitzgerald, E. A.; Bulsara, M. T.; Currie, M. T.; Lochtefeld, A. Strained Si, SiGe, and Ge Channels for High-Mobility Metal-Oxide-Semiconductor Field-Effect Transistors. *J. Appl. Phys.* **2005**, *97* (1), 011101.
(129) Fischetti, M. V.; Laux, S. E. Band Structure, Deformation Potentials, and Carrier Mobility in Strained Si, Ge, and SiGe Alloys. *J. Appl. Phys.* **1996**, *80* (4), 2234−2252.
(130) Thompson, S.E.; Armstrong, M.; Auth, C.; Alavi, M.; Buehler, M.; Chau, R.; Cea, S.; Ghani, T.; Glass, G.; Hoffman, T.; Jan, C.-H.; Kenyon, C.; Klaus, J.; Kuhn, K.; Ma, Z.; Mcintyre, B.; Mistry, K.; Murthy, A.; Obradovic, B.; Nagisetty, R.; Nguyen, P.; Sivakumar, S.; Shaheed, R.; Shifren, L.; Tufts, B.; Tyagi, S.; Bohr, M.; El-Mansy, Y. A 90-nm Logic Technology Featuring Strained-Silicon. *IEEE Trans. Electron Devices* **2004**, *51* (11), 1790−1797.
(131) Ieong, M.; Doris, B.; Kedzierski, J.; Rim, K.; Yang, M. Silicon Device Scaling to the Sub-10-nm Regime. *Science* **2004**, *306* (5704), 2057−2060.
(132) Geiger, R.; Zabel, T.; Sigg, H. Group IV Direct Band Gap Photonics: Methods, Challenges, and Opportunities. *Front. Mater.* **2015**, *2*, 52.
(133) Gupta, S.; Magyari-Köpe, B.; Nishi, Y.; Saraswat, K. C. Achieving Direct Band Gap in Germanium through Integration of Sn Alloying and External Strain. *J. Appl. Phys.* **2013**, *113* (7), 073707.
(134) Wirths, S.; Geiger, R.; von den Driesch, N.; Mussler, G.; Stoica, T.; Mantl, S.; Ikonic, Z.; Luysberg, M.; Chiussi, S.; Hartmann, J. M.; Sigg, H.; Faist, J.; Buca, D.; Grutzmacher, D. Lasing in Direct-Bandgap GeSn Alloy Grown on Si. *Nat. Photonics* **2015**, *9* (2), 88−92.
(135) Lan, H. S.; Chang, S. T.; Liu, C. W. Semiconductor, Topological Semimetal, Indirect Semimetal, and Topological Dirac Semimetal Phases of $Ge_{1-x}Sn_x$ Alloys. *Phys. Rev. B: Condens. Matter Mater. Phys.* **2017**, *95* (20), 201201.
(136) Ghetmiri, S. A.; Du, W.; Margetis, J.; Mosleh, A.; Cousar, L.; Conley, B. R.; Domulevicz, L.; Nazzal, A.; Sun, G.; Soref, R. A.; Tolle, J.; Li, B.; Naseem, H. A.; Yu, S.-Q. Direct-Bandgap GeSn Grown on Silicon with 2230 nm Photoluminescence. *Appl. Phys. Lett.* **2014**, *105* (15), 151109.
(137) Lu Low, K.; Yang, Y.; Han, G.; Fan, W.; Yeo, Y.-C. Electronic Band Structure and Effective Mass Parameters of $Ge_{1-x}Sn_x$ Alloys. *J. Appl. Phys.* **2012**, *112* (10), 103715.
(138) Chen, R.; Lin, H.; Huo, Y.; Hitzman, C.; Kamins, T. I.; Harris, J. S. Increased Photoluminescence of Strain-Reduced, High-Sn Composition $Ge_{1-x}Sn_x$ Alloys Grown by Molecular Beam Epitaxy. *Appl. Phys. Lett.* **2011**, *99* (18), 181125.
(139) Guo, Q.; Di, Z.; Lagally, M. G.; Mei, Y. Strain Engineering and Mechanical Assembly of Silicon/Germanium Nanomembranes. *Mater. Sci. Eng., R* **2018**, *128*, 1−31.
(140) Stange, D.; Wirths, S.; von den Driesch, N.; Mussler, G.; Stoica, T.; Ikonic, Z.; Hartmann, J. M.; Mantl, S.; Grützmacher, D.; Buca, D. Optical Transitions in Direct-Bandgap $Ge_{1-x}Sn_x$ Alloys. *ACS Photonics* **2015**, *2* (11), 1539−1545.
(141) von den Driesch, N.; Stange, D.; Wirths, S.; Mussler, G.; Holländer, B.; Ikonic, Z.; Hartmann, J. M.; Stoica, T.; Mantl, S.; Grützmacher, D.; Buca, D. Direct Bandgap Group IV Epitaxy on Si for Laser Applications. *Chem. Mater.* **2015**, *27* (13), 4693−4702.
(142) Attiaoui, A.; Moutanabbir, O. Indirect-to-Direct Band Gap Transition in Relaxed and Strained $Ge_{1-x-y}Si_xSn_y$ Ternary Alloys. *J. Appl. Phys.* **2014**, *116* (6), 063712.

https://dx.doi.org/10.1021/acs.chemmater.9b04471
Chem. Mater. 2020, 32, 2703−2741

(143) Goodman, C. H. L. Direct-Gap Group IV Semiconductors Based on Tin. *IEE Proc., Part I: Solid-State Electron Devices* **1982**, *129* (5), 189−192.
(144) Oguz, S.; Paul, W.; Deutsch, T. F.; Tsaur, B. Y.; Murphy, D. V. Synthesis of Metastable, Semiconducting Ge-Sn Alloys by Pulsed UV Laser Crystallization. *Appl. Phys. Lett.* **1983**, *43* (9), 848−850.
(145) Wirths, S.; Geiger, R.; von den Driesch, N.; Mussler, G.; Stoica, T.; Mantl, S.; Ikonic, Z.; Luysberg, M.; Chiussi, S.; Hartmann, J. M.; Sigg, H.; Faist, J.; Buca, D.; Grützmacher, D. Lasing in Direct-Bandgap GeSn Alloy Grown on Si. *Nat. Photonics* **2015**, *9* (2), 88−92.
(146) Schulze, J.; Blech, A.; Datta, A.; Fischer, I. A.; Hähnel, D.; Naasz, S.; Rolseth, E.; Tropper, E.-M. Vertical Ge and GeSn Heterojunction Gate-All-Around Tunneling Field Effect Transistors. *Solid-State Electron.* **2015**, *110* (Suppl. C), 59−64.
(147) Sau, J. D.; Cohen, M. L. Possibility of Increased Mobility in Ge-Sn Alloy System. *Phys. Rev. B: Condens. Matter Mater. Phys.* **2007**, *75* (4), 045208.
(148) Liu, L.; Liang, R.; Wang, J.; Xu, J. Investigation on the Effective Mass of $Ge_{1-x}Sn_x$ Alloys and the Transferred-Electron Effect. *Appl. Phys. Express* **2015**, *8* (3), 031301.
(149) Wang, S.; Zheng, J.; Xue, C.; Li, C.; Zuo, Y.; Cheng, B.; Wang, Q. Device Simulation of GeSn/GeSiSn Pocket n-Type Tunnel Field-Effect Transistor for Analog and RF Applications. *Superlattices Microstruct.* **2017**, *111*, 286−292.
(150) Stange, D.; Wirths, S.; Geiger, R.; Schulte-Braucks, C.; Marzban, B.; von den Driesch, N.; Mussler, G.; Zabel, T.; Stoica, T.; Hartmann, J.-M.; Mantl, S.; Ikonic, Z.; Grützmacher, D.; Sigg, H.; Witzens, J.; Buca, D. Optically Pumped GeSn Microdisk Lasers on Si. *ACS Photonics* **2016**, *3* (7), 1279−1285.
(151) Al-Kabi, S.; Ghetmiri, S. A.; Margetis, J.; Pham, T.; Zhou, Y.; Dou, W.; Collier, B.; Quinde, R.; Du, W.; Mosleh, A.; Liu, J.; Sun, G.; Soref, R. A.; Tolle, J.; Li, B.; Mortazavi, M.; Naseem, H. A.; Yu, S.-Q. An Optically Pumped 2.5 μm GeSn Laser on Si Operating at 110 K. *Appl. Phys. Lett.* **2016**, *109* (17), 171105.
(152) von den Driesch, N.; Stange, D.; Rainko, D.; Povstugar, I.; Zaumseil, P.; Capellini, G.; Schröder, T.; Denneulin, T.; Ikonic, Z.; Hartmann, J.-M.; Sigg, H.; Mantl, S.; Grützmacher, D.; Buca, D. Advanced GeSn/SiGeSn Group IV Heterostructure Lasers. *Adv. Sci.* **2018**, *5*, 1700955.
(153) Conley, B. R.; Margetis, J.; Du, W.; Tran, H.; Mosleh, A.; Ghetmiri, S. A.; Tolle, J.; Sun, G.; Soref, R.; Li, B.; Naseem, H. A.; Yu, S.-Q. Si Based GeSn Photoconductors with a 1.63 A/W Peak Responsivity and a 2.4 μm Long-Wavelength Cutoff. *Appl. Phys. Lett.* **2014**, *105* (22), 221117.
(154) Pham, T. N.; Du, W.; Conley, B. R.; Margetis, J.; Sun, G.; Soref, R. A.; Tolle, J.; Li, B.; Yu, S. Q. Si-Based $Ge_{0.9}Sn_{0.1}$ Photodetector with Peak Responsivity of 2.85 A/W and Longwave Cutoff at 2.4 μm. *Electron. Lett.* **2015**, *51* (11), 854−856.
(155) Tseng, H. H.; Wu, K. Y.; Li, H.; Mashanov, V.; Cheng, H. H.; Sun, G.; Soref, R. A. Mid-Infrared Electroluminescence From a Ge/$Ge_{0.922}Sn_{0.078}$/Ge Double Heterostructure p-i-n Diode on a Si Substrate. *Appl. Phys. Lett.* **2013**, *102* (18), 182106.
(156) Gupta, J. P.; Bhargava, N.; Kim, S.; Adam, T.; Kolodzey, J. Infrared Electroluminescence from GeSn Heterojunction Diodes Grown by Molecular Beam Epitaxy. *Appl. Phys. Lett.* **2013**, *102* (25), 251117.
(157) Chang, C.; Chang, T.-W.; Li, H.; Cheng, H. H.; Soref, R.; Sun, G.; Hendrickson, J. R. Room-Temperature 2-μm GeSn *p-i-n* Homojunction Light-Emitting Diode for Inplane Coupling to Group-IV Waveguides. *Appl. Phys. Lett.* **2017**, *111* (14), 141105.
(158) Soref, R. Mid-Infrared Photonics in Silicon and Germanium. *Nat. Photonics* **2010**, *4*, 495.
(159) Gupta, S.; Chen, R.; Huang, Y.-C.; Kim, Y.; Sanchez, E.; Harris, J. S.; Saraswat, K. C. Highly Selective Dry Etching of Germanium over Germanium−Tin (Ge1−xSnx): A Novel Route for Ge1−xSnx Nanostructure Fabrication. *Nano Lett.* **2013**, *13* (8), 3783−3790.
(160) Assali, S.; Nicolas, J.; Mukherjee, S.; Dijkstra, A.; Moutanabbir, O. Atomically Uniform Sn-Rich GeSn Semiconductors with 3.0−3.5 μm Room-Temperature Optical Emission. *Appl. Phys. Lett.* **2018**, *112* (25), 251903.
(161) Wang, X.; Cuervo Covian, A.; Je, L.; Fu, S.; Li, H.; Piao, J.; Liu, J. GeSn on Insulators (GeSnOI) Toward Mid-infrared Integrated Photonics. *Front. Phys.* **2019**, *7*, 134.
(162) Huang, W. Q.; Cheng, B. W.; Xue, C. L.; Yang, H. The Band Structure and Optical Gain of a new IV-Group Alloy GePb: A first-Principles Calculation. *J. Alloys Compd.* **2017**, *701*, 816−821.
(163) Cordero, B.; Gomez, V.; Platero-Prats, A. E.; Reves, M.; Echeverria, J.; Cremades, E.; Barragan, F.; Alvarez, S. Covalent Radii Revisited. *Dalton Trans* **2008**, No. 21, 2832−8.
(164) Tolle, J.; Chizmeshya, A. V. G.; Fang, Y. Y.; Kouvetakis, J.; D'Costa, V. R.; Hu, C. W.; Menéndez, J.; Tsong, I. S. T. Low Temperature Chemical Vapor Deposition of Si-based Compounds via $SiH_3SiH_2SiH_3$: Metastable SiSn/GeSn/Si(100) Heteroepitaxial Structures. *Appl. Phys. Lett.* **2006**, *89* (23), 231924.
(165) Moontragoon, P.; Ikonić, Z.; Harrison, P. Band Structure Calculations of Si−Ge−Sn Alloys: Achieving Direct Band Gap Materials. *Semicond. Sci. Technol.* **2007**, *22* (7), 742−748.
(166) Yu, L.; Alet, P. J.; Picardi, G.; Maurin, I.; Cabarrocas, P. R. Synthesis, Morphology and Compositional Evolution of Silicon Nanowires Directly Grown on $SnO_{(2)}$ Substrates. *Nanotechnology* **2008**, *19* (48), 485605.
(167) Bogart, T. D.; Lu, X.; Gu, M.; Wang, C.; Korgel, B. A. Enhancing the Lithiation Rate of Silicon Nanowires by the Inclusion of Tin. *RSC Adv.* **2014**, *4* (79), 42022−42028.
(168) Bogart, T. D.; Oka, D.; Lu, X.; Gu, M.; Wang, C.; Korgel, B. A. Lithium Ion Battery Peformance of Silicon Nanowires with Carbon Skin. *ACS Nano* **2014**, *8* (1), 915−22.
(169) Nikiforov, A. I.; Timofeev, V. A.; Mashanov, V. I.; Gavrilova, T. A.; Gulyaev, D. V. Elastically Stressed Pseudomorphic SiSn Island Array Formation with a Pedestal on the Si(1 0 0) Substrate Using Sn as a Growth Catalyst. *J. Cryst. Growth* **2019**, *518*, 103−107.
(170) Kurosawa, M.; Kato, M.; Takahashi, K.; Nakatsuka, O.; Zaima, S. Self-Organized Lattice-Matched Epitaxy of $Si_{1-x}Sn_x$ Alloys on (001)-Oriented Si, Ge, and InP Substrates. *Appl. Phys. Lett.* **2017**, *111* (19), 192106.
(171) Kurosawa, M.; Nakatsuka, O.; Zaima, S. Growth and Applications of $Si_{1-x}Sn_x$ Thin Films. *ECS Trans.* **2017**, *80* (4), 253−258.
(172) Kolmakov, A.; Moskovits, M. Chemical Sensing and Catalysis by One-Dimensional Metal-Oxide Nanostructures. *Annu. Rev. Mater. Res.* **2004**, *34* (1), 151−180.
(173) Cao, L.; White, J. S.; Park, J. S.; Schuller, J. A.; Clemens, B. M.; Brongersma, M. L. Engineering Light Absorption in Semiconductor Nanowire Devices. *Nat. Mater.* **2009**, *8* (8), 643−7.
(174) Yang, P. The Chemistry and Physics of Semiconductor Nanowires. *MRS Bull.* **2005**, *30* (2), 85−91.
(175) Kashchiev, D. Nucleation. In *Science and Technology of Crystal Growth*,; van der Eerden, J. P., Bruinsma, O. S. L., Eds.; Springer Netherlands: Dordrecht, 1995; pp 53−66.
(176) Vekilov, P. G. Nucleation. *Cryst. Growth Des.* **2010**, *10* (12), 5007−5019.
(177) De Yoreo, J. J.; Vekilov, P. G. Principles of Crystal Nucleation and Growth. *Rev. Mineral. Geochem.* **2003**, *54* (1), 57−93.
(178) Hartman, P.; Perdok, W. G. On the Relations Between Structure and Morphology of Crystals. I. *Acta Crystallogr.* **1955**, *8* (1), 49−52.
(179) Hartman, P.; Perdok, W. G. On the Relations Between Structure and Morphology of Crystals. II. *Acta Crystallogr.* **1955**, *8* (9), 521−524.
(180) Hartman, P.; Perdok, W. G. On the Relations Between Structure and Morphology of Crystals. III. *Acta Crystallogr.* **1955**, *8* (9), 525−529.
(181) Burton, W. K.; Cabrera, N.; Frank, F. C. The Growth of Crystals and the Equilibrium Structure of their Surfaces. *Philos. Trans. R. Soc., A* **1951**, *243* (866), 299−358.
(182) Vere, A. W. *Crystal Growth*; Springer: 1987.

(183) Clouet, E.; Nastar, M.; Sigli, C. Nucleation of Al_3Zr andAl_3Sc in Aluminum Alloys: From Kinetic Monte Carlo Simulations to Classical Theory. *Phys. Rev. B: Condens. Matter Mater. Phys.* **2004**, *69* (6), 064109.
(184) Strey, R.; Wagner, P. E.; Viisanen, Y. The Problem of Measuring Homogeneous Nucleation Rates and the Molecular Contents of Nuclei: Progress in the Form of Nucleation Pulse Measurements. *J. Phys. Chem.* **1994**, *98* (32), 7748−7758.
(185) Gebauer, D.; Kellermeier, M.; Gale, J. D.; Bergstrom, L.; Colfen, H. Pre-Nucleation Clusters as Solute Precursors in Crystallisation. *Chem. Soc. Rev.* **2014**, *43* (7), 2348−71.
(186) Gebauer, D.; Wolf, S. E. Designing Solid Materials from Their Solute State: A Shift in Paradigms toward a Holistic Approach in Functional Materials Chemistry. *J. Am. Chem. Soc.* **2019**, *141* (11), 4490−4504.
(187) Mer, V. K. L. Nucleation in Phase Transitions. *Ind. Eng. Chem.* **1952**, *44* (6), 1270−1277.
(188) Laxson, W. W.; Finke, R. G. Nucleation is Second Order: An Apparent Kinetically Effective Nucleus of Two for $Ir(0)_n$ Nanoparticle Formation from $[(1,5\text{-COD})IrI{\cdot}P_2W_{15}Nb_3O_{62}]^{8-}$ Plus Hydrogen. *J. Am. Chem. Soc.* **2014**, *136* (50), 17601−17615.
(189) Whitehead, C. B.; Özkar, S.; Finke, R. G. LaMer's 1950 Model for Particle Formation of Instantaneous Nucleation and Diffusion-Controlled Growth: A Historical Look at the Model's Origins, Assumptions, Equations, and Underlying Sulfur Sol Formation Kinetics Data. *Chem. Mater.* **2019**, *31* (18), 7116−7132.
(190) Wu, Z.; Yang, S.; Wu, W. Shape Control of Inorganic Nanoparticles From Solution. *Nanoscale* **2016**, *8* (3), 1237−1259.
(191) Xia, Y.; Xiong, Y.; Lim, B.; Skrabalak, S. E. Shape-Controlled Synthesis of Metal Nanocrystals: Simple Chemistry Meets Complex Physics? *Angew. Chem., Int. Ed.* **2009**, *48* (1), 60−103.
(192) Polavarapu, L.; Mourdikoudis, S.; Pastoriza-Santos, I.; Pérez-Juste, J. Nanocrystal Engineering of Noble Metals and Metal chalcogenides: Controlling the Morphology, Composition and Crystallinity. *CrystEngComm* **2015**, *17* (20), 3727−3762.
(193) Wilson, H. F.; Barnard, A. S. Predictive Morphology Control of Hydrogen-Terminated Silicon Nanoparticles. *J. Phys. Chem. C* **2014**, *118* (5), 2580−2586.
(194) Baldwin, R. K.; Pettigrew, K. A.; Garno, J. C.; Power, P. P.; Liu, G.-y.; Kauzlarich, S. M. Room Temperature Solution Synthesis of Alkyl-Capped Tetrahedral Shaped Silicon Nanocrystals. *J. Am. Chem. Soc.* **2002**, *124* (7), 1150−1151.
(195) Barrett, C. A.; Dickinson, C.; Ahmed, S.; Hantschel, T.; Arstila, K.; Ryan, K. M. The Evolution of Pseudo-Spherical Silicon Nanocrystals to Tetrahedra, Mediated by Phosphonic Acid Surfactants. *Nanotechnology* **2009**, *20* (27), 275605.
(196) Bapat, A.; Anderson, C.; Perrey, C. R.; Carter, C. B.; Campbell, S. A.; Kortshagen, U. Plasma Synthesis of Single-Crystal Silicon Nanoparticles for Novel Electronic Device Applications. *Plasma Phys. Controlled Fusion* **2004**, *46* (12B), B97−B109.
(197) Yang, Z.; Dobbie, A. R.; Cui, K.; Veinot, J. G. C. A Convenient Method for Preparing Alkyl-Functionalized Silicon Nanocubes. *J. Am. Chem. Soc.* **2012**, *134* (34), 13958−13961.
(198) Wang; Huang; Ren. Synthesis of Germanium Nanocubes by a Low-Temperature Inverse Micelle Solvothermal Technique. *Langmuir* **2005**, *21* (2), 751−754.
(199) Yu, Y.; Lu, X.; Guillaussier, A.; Voggu, V. R.; Pineros, W.; de la Mata, M.; Arbiol, J.; Smilgies, D.-M.; Truskett, T. M.; Korgel, B. A. Orientationally Ordered Silicon Nanocrystal Cuboctahedra in Superlattices. *Nano Lett.* **2016**, *16* (12), 7814−7821.
(200) Lu, W.; Lieber, C. M. Semiconductor Nanowires. *J. Phys. D: Appl. Phys.* **2006**, *39* (21), R387−R406.
(201) Borgstrom, M. T.; Immink, G.; Ketelaars, B.; Algra, R.; Bakkers, E. P. Synergetic Nanowire Growth. *Nat. Nanotechnol.* **2007**, *2* (9), 541−4.
(202) Wang, N.; Cai, Y.; Zhang, R. Q. Growth of Nanowires. *Mater. Sci. Eng., R* **2008**, *60* (1−6), 1−51.
(203) Barth, S.; Hernandez-Ramirez, F.; Holmes, J. D.; Romano-Rodriguez, A. Synthesis and Applications of One-Dimensional Semiconductors. *Prog. Mater. Sci.* **2010**, *55* (6), 563−627.
(204) Ek, M.; Filler, M. A. Atomic-Scale Choreography of Vapor-Liquid-Solid Nanowire Growth. *Acc. Chem. Res.* **2018**, *51* (1), 118−126.
(205) Guniat, L.; Caroff, P.; Fontcuberta i Morral, A. Vapor Phase Growth of Semiconductor Nanowires: Key Developments and Open Questions. *Chem. Rev.* **2019**, *119*, 8958−8971.
(206) Jia, C.; Lin, Z.; Huang, Y.; Duan, X. Nanowire Electronics: From Nanoscale to Macroscale. *Chem. Rev.* **2019**, *119*, 9074−9135.
(207) Staudinger, P.; Sistani, M.; Greil, J.; Bertagnolli, E.; Lugstein, A. Ultrascaled Germanium Nanowires for Highly Sensitive Photodetection at the Quantum Ballistic Limit. *Nano Lett.* **2018**, *18* (8), 5030−5035.
(208) Quan, L. N.; Kang, J.; Ning, C. Z.; Yang, P. Nanowires for Photonics. *Chem. Rev.* **2019**, *119*, 9153−9169.
(209) Shen, F.; Wang, J.; Xu, Z.; Wu, Y.; Chen, Q.; Li, X.; Jie, X.; Li, L.; Yao, M.; Guo, X.; Zhu, T. Rapid Flu Diagnosis Using Silicon Nanowire Sensor. *Nano Lett.* **2012**, *12* (7), 3722−30.
(210) Shehada, N.; Cancilla, J. C.; Torrecilla, J. S.; Pariente, E. S.; Bronstrup, G.; Christiansen, S.; Johnson, D. W.; Leja, M.; Davies, M. P.; Liran, O.; Peled, N.; Haick, H. Silicon Nanowire Sensors Enable Diagnosis of Patients via Exhaled Breath. *ACS Nano* **2016**, *10* (7), 7047−57.
(211) Samà, J.; Seifner, M. S.; Domènech-Gil, G.; Santander, J.; Calaza, C.; Moreno, M.; Gràcia, I.; Barth, S.; Romano-Rodríguez, A. Low Temperature Humidity Sensor Based on Ge Nanowires Selectively Grown on Suspended Microhotplates. *Sens. Actuators, B* **2017**, *243*, 669−677.
(212) Hrachowina, L.; Domenech-Gil, G.; Pardo, A.; Seifner, M. S.; Gracia, I.; Cane, C.; Romano-Rodriguez, A.; Barth, S. Site-Specific Growth and in Situ Integration of Different Nanowire Material Networks on a Single Chip: Toward a Nanowire-Based Electronic Nose for Gas Detection. *ACS Sensors* **2018**, *3* (3), 727−734.
(213) Barth, S.; Jimenez-Diaz, R.; Samà, J.; Daniel Prades, J.; Gracia, I.; Santander, J.; Cane, C.; Romano-Rodriguez, A. Localized Growth and *in situ* Integration of Nanowires for Device Applications. *Chem. Commun.* **2012**, *48* (39), 4734−4736.
(214) Chan, C. K.; Peng, H.; Liu, G.; McIlwrath, K.; Zhang, X. F.; Huggins, R. A.; Cui, Y. High-Performance Lithium Battery Anodes using Silicon Nanowires. *Nat. Nanotechnol.* **2008**, *3* (1), 31−5.
(215) Chan, C. K.; Zhang, X. F.; Cui, Y. High Capacity Li Ion Battery Anodes using Ge Nanowires. *Nano Lett.* **2008**, *8* (1), 307−9.
(216) Chockla, A. M.; Klavetter, K. C.; Mullins, C. B.; Korgel, B. A. Solution-Grown Germanium Nanowire Anodes for Lithium-Ion Batteries. *ACS Appl. Mater. Interfaces* **2012**, *4* (9), 4658−64.
(217) Wu, H.; Cui, Y. Designing Nanostructured Si Anodes for High Energy Lithium Ion Batteries. *Nano Today* **2012**, *7* (5), 414−429.
(218) Kennedy, T.; Mullane, E.; Geaney, H.; Osiak, M.; O'Dwyer, C.; Ryan, K. M. High-Performance Germanium Nanowire-Based Lithium-ion Battery Anodes Extending Over 1000 Cycles Through *in situ* Formation of a Continuous Porous Network. *Nano Lett.* **2014**, *14* (2), 716−23.
(219) Hobbs, R. G.; Petkov, N.; Holmes, J. D. Semiconductor Nanowire Fabrication by Bottom-Up and Top-Down Paradigms. *Chem. Mater.* **2012**, *24* (11), 1975−1991.
(220) Wagner, R. S.; Ellis, W. C. Vapor-Liquid-Solid Mechanism of Single Crystal Growth. *Appl. Phys. Lett.* **1964**, *4* (5), 89−90.
(221) Lensch-Falk, J. L.; Hemesath, E. R.; Perea, D. E.; Lauhon, L. J. Alternative Catalysts for VSS Growth of Silicon and Germanium Nanowires. *J. Mater. Chem.* **2009**, *19* (7), 849−857.
(222) Wen, C. Y.; Reuter, M. C.; Tersoff, J.; Stach, E. A.; Ross, F. M. Structure, Growth Kinetics, and Ledge Flow during Vapor-Solid-Solid Growth of Copper-Catalyzed Silicon Nanowires. *Nano Lett.* **2010**, *10* (2), 514−519.
(223) Barth, S.; Seifner, M. S.; Bernardi, J. Growth of Monocrystalline In_2O_3 Nanowires by a Seed Orientation Dependent Vapour−Solid−Solid Mechanism. *J. Mater. Chem. C* **2014**, *2* (29), 5747−5751.

https://dx.doi.org/10.1021/acs.chemmater.9b04471
Chem. Mater. 2020, 32, 2703−2741

(224) Trentler, T. J.; Hickman, K. M.; Goel, S. C.; Viano, A. M.; Gibbons, P. C.; Buhro, W. E. Solution-Liquid-Solid Growth of Crystalline III-V Semiconductors - an Analogy to Vapor-Liquid-Solid Growth. *Science* **1995**, *270* (5243), 1791−1794.
(225) Lu, X.; Hessel, C. M.; Yu, Y.; Bogart, T. D.; Korgel, B. A. Colloidal Luminescent Silicon Nanorods. *Nano Lett.* **2013**, *13* (7), 3101−3105.
(226) Wang, J.; Chen, K.; Gong, M.; Xu, B.; Yang, Q. Solution−Solid−Solid Mechanism: Superionic Conductors Catalyze Nanowire Growth. *Nano Lett.* **2013**, *13* (9), 3996−4000.
(227) Guria, A. K.; Sarkar, S.; Patra, B. K.; Pradhan, N. Efficient Superionic Conductor Catalyst for Solid in Solution−Solid−Solid Growth of Heteronanowires. *J. Phys. Chem. Lett.* **2014**, *5* (4), 732−736.
(228) Holmes, J. D.; Johnston, K. P.; Doty, R. C.; Korgel, B. A. Control of Thickness and Orientation of Solution-Grown Silicon Nanowires. *Science* **2000**, *287* (5457), 1471−1473.
(229) Korgel, B. A. Supercritical Fluid-Liquid-Solid (SFLS) Growth of Semiconductor Nanowires. In *One-Dimensional Nanostructures*; Zhai, T., Yao, J., Eds.; John Wiley & Sons, Inc.: Hoboken, NJ, 2013; pp 41−63.
(230) Collins, G.; Fleming, P.; Barth, S.; O'Dwyer, C.; Boland, J. J.; Morris, M. A.; Holmes, J. D. Alkane and Alkanethiol Passivation of Halogenated Ge Nanowires. *Chem. Mater.* **2010**, *22* (23), 6370−6377.
(231) Barth, S.; Boland, J. J.; Holmes, J. D. Defect Transfer from Nanoparticles to Nanowires. *Nano Lett.* **2011**, *11* (4), 1550−1555.
(232) Tuan, H. Y.; Lee, D. C.; Hanrath, T.; Korgel, B. A. Germanium Nanowire Synthesis: An Example of Solid-Phase Seeded Growth with Nickel Nanocrystals. *Chem. Mater.* **2005**, *17* (23), 5705−5711.
(233) Barth, S.; Koleśnik, M. M.; Donegan, K.; Krstić, V.; Holmes, J. D. Diameter-Controlled Solid-Phase Seeding of Germanium Nanowires: Structural Characterization and Electrical Transport Properties. *Chem. Mater.* **2011**, *23* (14), 3335−3340.
(234) Okamoto, H.; Massalski, T. B. The Au−Si (Gold-Silicon) System. *Bull. Alloy Phase Diagrams* **1983**, *4* (2), 190−198.
(235) Gamalski, A. D.; Ducati, C.; Hofmann, S. Cyclic Supersaturation and Triple Phase Boundary Dynamics in Germanium Nanowire Growth. *J. Phys. Chem. C* **2011**, *115* (11), 4413−4417.
(236) Oh, S. H.; Chisholm, M. F.; Kauffmann, Y.; Kaplan, W. D.; Luo, W.; Rühle, M.; Scheu, C. Oscillatory Mass Transport in Vapor-Liquid-Solid Growth of Sapphire Nanowires. *Science* **2010**, *330* (6003), 489−493.
(237) Heurlin, M.; Magnusson, M. H.; Lindgren, D.; Ek, M.; Wallenberg, L. R.; Deppert, K.; Samuelson, L. Continuous Gas-Phase Synthesis of Nanowires with Tunable Properties. *Nature* **2012**, *492*, 90.
(238) Dick, K. A.; Deppert, K.; Mårtensson, T.; Mandl, B.; Samuelson, L.; Seifert, W. Failure of the Vapor−Liquid−Solid Mechanism in Au-Assisted MOVPE Growth of InAs Nanowires. *Nano Lett.* **2005**, *5* (4), 761−764.
(239) Fontcuberta i Morral, A.; Colombo, C.; Abstreiter, G.; Arbiol, J.; Morante, J. R. Nucleation Mechanism of Gallium-Assisted Molecular Beam Epitaxy Growth of Gallium Arsenide Nanowires. *Appl. Phys. Lett.* **2008**, *92* (6), 063112.
(240) Woo, R. L.; Gao, L.; Goel, N.; Hudait, M. K.; Wang, K. L.; Kodambaka, S.; Hicks, R. F. Kinetic Control of Self-Catalyzed Indium Phosphide Nanowires, Nanocones, and Nanopillars. *Nano Lett.* **2009**, *9* (6), 2207−2211.
(241) Chen, W.; Yu, L.; Misra, S.; Fan, Z.; Pareige, P.; Patriarche, G.; Bouchoule, S.; Roca i Cabarrocas, P. Incorporation and Redistribution of Impurities into Silicon Nanowires During Metal-Particle-Assisted Growth. *Nat. Commun.* **2014**, *5*, 4134.
(242) Wippermann, S.; Voros, M.; Rocca, D.; Gali, A.; Zimanyi, G.; Galli, G. High-Pressure Core Structures of Si Nanoparticles for Solar Energy Conversion. *Phys. Rev. Lett.* **2013**, *110* (4), 046804.
(243) Viera, G.; Mikikian, M.; Bertran, E.; Cabarrocas, P. R. i.; Boufendi, L. Atomic Structure of the Nanocrystalline Si Particles Appearing in Nanostructured Si Thin Films Produced in Low-Temperature Radiofrequency Plasmas. *J. Appl. Phys.* **2002**, *92* (8), 4684−4694.
(244) Du, X.-W.; Qin, W.-J.; Lu, Y.-W.; Han, X.; Fu, Y.-S.; Hu, S.-L. Face-Centered-Cubic Si Nanocrystals Prepared by Microsecond Pulsed Laser Ablation. *J. Appl. Phys.* **2007**, *102* (1), 013518.
(245) Lu, Y. W.; Du, X. W.; Sun, J.; Hu, S. L.; Han, X.; Li, H. Formation and Luminescent Properties of Face-Centered-Cubic Si Nanocrystals in Silica Matrix by Magnetron Sputtering with Substrate Bias. *Appl. Phys. Lett.* **2007**, *90* (24), 241910.
(246) Du, X. W.; Wang, B.; Zhao, N. Q.; Furuya, K. Structure Evolution of Silicon Nanocrystals Under Electron Irradiation. *Scr. Mater.* **2005**, *53* (8), 899−903.
(247) Saxena, N.; Kumar, P.; Agarwal, A.; Kanjilal, D. Lattice Distortion in Ion Beam Synthesized Silicon Nanocrystals in SiO_x Thin Films. *Phys. Status Solidi A* **2012**, *209* (2), 283−288.
(248) Zeng, Y.; Chen, X.; Cheng, Q.; Zhao, J.; Song, W.; Dai, N. Thermodynamics of the Formation of Face-Centered-Cubic Silicon Nanocrystals in Silicon-Rich SiC Thin Films Annealed Using Rapid Thermal Annealing. *Appl. Surf. Sci.* **2013**, *265*, 286−290.
(249) Hu, S.; Zhang, J.; Yang, J.; Liu, J.; Cao, S. Theoretical Analysis of The Formation of Face-Centered Cubic Si Nanocrystals by Magnetron Sputtering. *Appl. Phys. Lett.* **2011**, *99* (15), 151901.
(250) Hu, S.; Li, W.; Liu, W.; Dong, Y.; Cao, S.; Yang, J. Thermodynamics of Face-Centered-Cubic Silicon Nucleation at the Nanoscale from Laser Ablation. *J. Phys.: Condens. Matter* **2011**, *23* (20), 205302.
(251) Balcı, M. H.; Sæterli, R.; Maria, J.; Lindgren, M.; Holmestad, R.; Grande, T.; Einarsrud, M.-A. Solution Based Synthesis of Simple fcc Si Nano-Crystals Under Ambient Conditions. *Dalton Trans* **2013**, *42* (8), 2700−2703.
(252) Liu, A. Y.; Chang, K. J.; Cohen, M. L. Theory of Electronic, Vibrational, and Superconducting Properties of fcc Silicon. *Phys. Rev. B: Condens. Matter Mater. Phys.* **1988**, *37* (11), 6344−6348.
(253) Arguirov, T.; McHedlidze, T.; Kittler, M.; Rölver, R.; Berghoff, B.; Först, M.; Spangenberg, B. Residual Stress in Si Nanocrystals Embedded in a SiO_2 Matrix. *Appl. Phys. Lett.* **2006**, *89* (5), 053111.
(254) Smith, M. J.; Lin, Y.-T.; Sher, M.-J.; Winkler, M. T.; Mazur, E.; Gradečak, S. Pressure-Induced Phase Transformations During Femtosecond-Laser Doping of Silicon. *J. Appl. Phys.* **2011**, *110* (5), 053524.
(255) Wang, Y.; Zou, J.; Huang, H.; Zhou, L.; Wang, B. L.; Wu, Y. Q. Formation Mechanism of Nanocrystalline High-Pressure Phases in Silicon During Nanogrinding. *Nanotechnology* **2007**, *18* (46), 465705.
(256) Ganguly, S.; Kazem, N.; Carter, D.; Kauzlarich, S. M. Colloidal Synthesis of an Exotic Phase of Silicon: the BC8 Structure. *J. Am. Chem. Soc.* **2014**, *136* (4), 1296−9.
(257) Navrotsky, A. Energetic Clues to Pathways to Biomineralization: Precursors, Clusters, and Nanoparticles. *Proc. Natl. Acad. Sci. U. S. A.* **2004**, *101* (33), 12096−101.
(258) Aslanov, L. A.; Zakharov, V. N.; Savilov, S. V.; Senyavin, V. M.; Yatsenko, A. V. Synthesis and Properties of Nanosilicon Prepared by Homogeneous and Heterogeneous Reduction of Tetraethyl Orthosilicate. *Russ. J. Coord. Chem.* **2014**, *40* (9), 607−610.
(259) Hannah, D. C.; Yang, J.; Podsiadlo, P.; Chan, M. K. Y.; Demortière, A.; Gosztola, D. J.; Prakapenka, V. B.; Schatz, G. C.; Kortshagen, U.; Schaller, R. D. On the Origin of Photoluminescence in Silicon Nanocrystals: Pressure-Dependent Structural and Optical Studies. *Nano Lett.* **2012**, *12* (8), 4200−4205.
(260) Zhang, X.; Brynda, M.; Britt, R. D.; Carroll, E. C.; Larsen, D. S.; Louie, A. Y.; Kauzlarich, S. M. Synthesis and Characterization of Manganese-Doped Silicon Nanoparticles: Bifunctional Paramagnetic-Optical Nanomaterial. *J. Am. Chem. Soc.* **2007**, *129* (35), 10668−9.
(261) Singh, M. P.; Atkins, T. M.; Muthuswamy, E.; Kamali, S.; Tu, C.; Louie, A. Y.; Kauzlarich, S. M. Development of Iron-Doped Silicon Nanoparticles as Bimodal Imaging Agents. *ACS Nano* **2012**, *6* (6), 5596−604.

https://dx.doi.org/10.1021/acs.chemmater.9b04471
Chem. Mater. 2020, 32, 2703−2741

(262) McVey, B. F.; Butkus, J.; Halpert, J. E.; Hodgkiss, J. M.; Tilley, R. D. Solution Synthesis and Optical Properties of Transition-Metal-Doped Silicon Nanocrystals. *J. Phys. Chem. Lett.* **2015**, *6* (9), 1573−6.
(263) Chandra, S.; Masuda, Y.; Shirahata, N.; Winnik, F. M. Transition-Metal-Doped NIR-Emitting Silicon Nanocrystals. *Angew. Chem., Int. Ed.* **2017**, *56* (22), 6157−6160.
(264) Klimešová, E.; Kůsová, K.; Vacík, J.; Holý, V.; Pelant, I. Tuning Luminescence Properties of Silicon Nanocrystals by Lithium Doping. *J. Appl. Phys.* **2012**, *112* (6), 064322.
(265) Tchebotareva, A. L.; de Dood, M. J. A.; Biteen, J. S.; Atwater, H. A.; Polman, A. Quenching of Si Nanocrystal Photoluminescence by Doping with Gold or Phosphorous. *J. Lumin.* **2005**, *114* (2), 137−144.
(266) St. John, J.; Coffer, J. L.; Chen, Y.; Pinizzotto, R. F. Synthesis and Characterization of Discrete Luminescent Erbium-Doped Silicon Nanocrystals. *J. Am. Chem. Soc.* **1999**, *121* (9), 1888−1892.
(267) John, J. S.; Coffer, J. L.; Chen, Y.; Pinizzotto, R. F. Size Control of Erbium-Doped Silicon Nanocrystals. *Appl. Phys. Lett.* **2000**, *77* (11), 1635−1637.
(268) Heitmann, J.; Schmidt, M.; Zacharias, M.; Timoshenko, V. Y.; Lisachenko, M. G.; Kashkarov, P. K. Fabrication and Photoluminescence Properties of Erbium doped Size-Controlled Silicon Nanocrystals. *Mater. Sci. Eng., B* **2003**, *105* (1−3), 214−220.
(269) Ji, J.; Senter, R. A.; Tessler, L. R.; Back, D.; Winter, C. H.; Coffer, J. L. Rare Earth Doped Silicon Nanocrystals Derived from an Erbium Amidinate Precursor. *Nanotechnology* **2004**, *15* (5), 643−647.
(270) Fujii, M.; Hayashi, S.; Yamamoto, K. Photoluminescence from B-doped Si Nanocrystals. *J. Appl. Phys.* **1998**, *83* (12), 7953−7957.
(271) Mimura, A.; Fujii, M.; Hayashi, S.; Yamamoto, K. Quenching of Photoluminescence From Si Nanocrystals Caused by Boron Doping. *Solid State Commun.* **1999**, *109* (9), 561−565.
(272) Fujii, M.; Toshikiyo, K.; Takase, Y.; Yamaguchi, Y.; Hayashi, S. Below Bulk-Band-Gap Photoluminescence at Room Temperature from Heavily P- and B-Doped Si Nanocrystals. *J. Appl. Phys.* **2003**, *94* (3), 1990−1995.
(273) Hao, X. J.; Cho, E. C.; Flynn, C.; Shen, Y. S.; Park, S. C.; Conibeer, G.; Green, M. A. Synthesis and Characterization of Boron-doped Si Quantum Dots for all-Si Quantum Dot Tandem Solar Cells. *Sol. Energy Mater. Sol. Cells* **2009**, *93* (2), 273−279.
(274) Sato, K.; Niino, K.; Fukata, N.; Hirakuri, K.; Yamauchi, Y. The Synthesis and Structural Characterization of Boron-Doped Silicon-Nanocrystals with Enhanced Electroconductivity. *Nanotechnology* **2009**, *20* (36), 365207.
(275) Sugimoto, H.; Fujii, M.; Imakita, K.; Hayashi, S.; Akamatsu, K. All-Inorganic Near-Infrared Luminescent Colloidal Silicon Nanocrystals: High Dispersibility in Polar Liquid by Phosphorus and Boron Codoping. *J. Phys. Chem. C* **2012**, *116* (33), 17969−17974.
(276) Kramer, N. J.; Schramke, K. S.; Kortshagen, U. R. Plasmonic Properties of Silicon Nanocrystals Doped with Boron and Phosphorus. *Nano Lett.* **2015**, *15* (8), 5597−603.
(277) Zhou, S.; Pi, X.; Ni, Z.; Ding, Y.; Jiang, Y.; Jin, C.; Delerue, C.; Yang, D.; Nozaki, T. Comparative Study on the Localized Surface Plasmon Resonance of Boron- and Phosphorus-doped Silicon Nanocrystals. *ACS Nano* **2015**, *9* (1), 378−86.
(278) Zhou, S.; Pi, X.; Ni, Z.; Luan, Q.; Jiang, Y.; Jin, C.; Nozaki, T.; Yang, D. Boron- and Phosphorus-Hyperdoped Silicon Nanocrystals. *Part. Part. Syst. Charact.* **2015**, *32* (2), 213−221.
(279) Ni, Z.; Pi, X.; Zhou, S.; Nozaki, T.; Grandidier, B.; Yang, D. Size-Dependent Structures and Optical Absorption of Boron-Hyperdoped Silicon Nanocrystals. *Adv. Opt. Mater.* **2016**, *4* (5), 700−707.
(280) Nomoto, K.; Sugimoto, H.; Breen, A.; Ceguerra, A. V.; Kanno, T.; Ringer, S. P.; Wurfl, I. P.; Conibeer, G.; Fujii, M. Atom Probe Tomography Analysis of Boron and/or Phosphorus Distribution in Doped Silicon Nanocrystals. *J. Phys. Chem. C* **2016**, *120* (31), 17845−17852.
(281) Zhou, S.; Ni, Z.; Ding, Y.; Sugaya, M.; Pi, X.; Nozaki, T. Ligand-Free, Colloidal, and Plasmonic Silicon Nanocrystals Heavily Doped with Boron. *ACS Photonics* **2016**, *3* (3), 415−422.
(282) Mimura, A.; Fujii, M.; Hayashi, S.; Kovalev, D.; Koch, F. Photoluminescence and Free-Electron Absorption in Heavily Phosphorus-Doped Si Nanocrystals. *Phys. Rev. B: Condens. Matter Mater. Phys.* **2000**, *62* (19), 12625−12627.
(283) Stegner, A. R.; Pereira, R. N.; Klein, K.; Lechner, R.; Dietmueller, R.; Brandt, M. S.; Stutzmann, M.; Wiggers, H. Electronic Transport in Phosphorus-Doped Silicon Nanocrystal Networks. *Phys. Rev. Lett.* **2008**, *100* (2), 026803.
(284) Rowe, D. J.; Jeong, J. S.; Mkhoyan, K. A.; Kortshagen, U. R. Phosphorus-Doped Silicon Nanocrystals Exhibiting Mid-Infrared Localized Surface Plasmon Resonance. *Nano Lett.* **2013**, *13* (3), 1317−22.
(285) Yang, P.; Gwilliam, R. M.; Crowe, I. F.; Papachristodoulou, N.; Halsall, M. P.; Hylton, N. P.; Hulko, O.; Knights, A. P.; Shah, M.; Kenyon, A. J. Size Limit on the Phosphorous Doped Silicon Nanocrystals for Dopant Activation. *Nucl. Instrum. Methods Phys. Res., Sect. B* **2013**, *307*, 456−458.
(286) Sun, E.; Su, F.-H.; Chen, C.-H.; Tsai, H.-L.; Yang, J.-R.; Chen, M.-J. Temperature-Dependent Photoluminescence of Arsenic-Doped Si Nanocrystals. *J. Lumin.* **2010**, *130* (8), 1485−1488.
(287) Khelifi, R.; Mathiot, D.; Gupta, R.; Muller, D.; Roussel, M.; Duguay, S. Efficient n-Type Doping of Si Nanocrystals Embedded in SiO_2 by ion Beam Synthesis. *Appl. Phys. Lett.* **2013**, *102* (1), 013116.
(288) Olesinski, R. W.; Abbaschian, G. J. The As−Si (Arsenic-Silicon) System. *Bull. Alloy Phase Diagrams* **1985**, *6* (3), 254−258.
(289) Olesinski, R. W.; Abbaschian, G. J. The B−Si (Boron-Silicon) System. *Bull. Alloy Phase Diagrams* **1984**, *5* (5), 478−484.
(290) Rohani, P.; Banerjee, S.; Sharifi-Asl, S.; Malekzadeh, M.; Shahbazian-Yassar, R.; Billinge, S. J. L.; Swihart, M. T. Synthesis and Properties of Plasmonic Boron-Hyperdoped Silicon Nanoparticles. *Adv. Funct. Mater.* **2019**, *29* (8), 1807788.
(291) Ishida, K.; Nishizawa, T.; Schlesinger, M. E. The Co-Si (Cobalt-Silicon) System. *J. Phase Equilib.* **1991**, *12* (5), 578−586.
(292) Olesinski, R. W.; Abbaschian, G. J. The Cu−Si (Copper-Silicon) System. *Bull. Alloy Phase Diagrams* **1986**, *7* (2), 170−178.
(293) Polman, A. Erbium Implanted Thin Film Photonic Materials. *J. Appl. Phys.* **1997**, *82* (1), 1−39.
(294) Weber, E.; Riotte, H. G. The Solution of Iron in Silicon. *J. Appl. Phys.* **1980**, *51* (3), 1484−1488.
(295) Okamoto, H. The Li-Si (Lithium-Silicon) System. *Bull. Alloy Phase Diagrams* **1990**, *11* (3), 306−312.
(296) Carlson, R. O. Properties of Silicon Doped with Manganese. *Phys. Rev.* **1956**, *104* (4), 937−941.
(297) Nash, P.; Nash, A. The Ni−Si (Nickel-Silicon) System. *Bull. Alloy Phase Diagrams* **1987**, *8* (1), 6−14.
(298) Olesinski, R. W.; Kanani, N.; Abbaschian, G. J. The P−Si (Phosphorus-Silicon) System. *Bull. Alloy Phase Diagrams* **1985**, *6* (2), 130−133.
(299) Pi, X. D.; Gresback, R.; Liptak, R. W.; Campbell, S. A.; Kortshagen, U. Doping Efficiency, Dopant Location, and Oxidation of Si Nanocrystals. *Appl. Phys. Lett.* **2008**, *92* (12), 123102.
(300) Key, B.; Bhattacharyya, R.; Morcrette, M.; Seznéc, V.; Tarascon, J.-M.; Grey, C. P. Real-Time NMR Investigations of Structural Changes in Silicon Electrodes for Lithium-Ion Batteries. *J. Am. Chem. Soc.* **2009**, *131* (26), 9239−9249.
(301) Priolo, F.; Franzò, G.; Coffa, S.; Polman, A.; Libertino, S.; Barklie, R.; Carey, D. The Erbium-Impurity Interaction and its Effects on the 1.54 μm Luminescence of Er^{3+} in Crystalline Silicon. *J. Appl. Phys.* **1995**, *78* (6), 3874−3882.
(302) Faucheaux, J. A.; Stanton, A. L.; Jain, P. K. Plasmon Resonances of Semiconductor Nanocrystals: Physical Principles and New Opportunities. *J. Phys. Chem. Lett.* **2014**, *5* (6), 976−85.
(303) Mangolini, L.; Kortshagen, U. Selective Nanoparticle Heating: Another Form of Nonequilibrium in Dusty Plasmas. *Phys. Rev. E: Stat., Nonlinear, Soft Matter Phys.* **2009**, *79* (2), 026405.
(304) Pi, X.; Chen, X.; Yang, D. First-Principles Study of 2.2 nm Silicon Nanocrystals Doped with Boron. *J. Phys. Chem. C* **2011**, *115* (20), 9838−9843.

https://dx.doi.org/10.1021/acs.chemmater.9b04471
Chem. Mater. 2020, 32, 2703−2741

(305) Alippi, P.; Ruggerone, P.; Colombo, L. Neutral Boron-Interstitial Clusters in Crystalline Silicon. *Phys. Rev. B: Condens. Matter Mater. Phys.* **2004**, *69* (12), 125205.
(306) Chan, T. L.; Tiago, M. L.; Kaxiras, E.; Chelikowsky, J. R. Size Limits on Doping Phosphorus into Silicon Nanocrystals. *Nano Lett.* **2008**, *8* (2), 596−600.
(307) Yu, L.; Fortuna, F.; O'Donnell, B.; Jeon, T.; Foldyna, M.; Picardi, G.; Roca i Cabarrocas, P. Bismuth-Catalyzed and Doped Silicon Nanowires for One-Pump-Down Fabrication of Radial Junction Solar Cells. *Nano Lett.* **2012**, *12* (8), 4153−8.
(308) Chen, X.; Pi, X.; Yang, D. Critical Role of Dopant Location for P-Doped Si Nanocrystals. *J. Phys. Chem. C* **2011**, *115* (3), 661−666.
(309) Miyamoto, Y.; Hirata, M. Polytypism and Amorphousness in Silicon Whiskers. *J. Phys. Soc. Jpn.* **1978**, *44* (1), 181−190.
(310) Arbiol, J.; Kalache, B.; Cabarrocas, P. R. i.; Morante, J. R.; Morral, A. F. i. Influence of Cu as a Ccatalyst on the Properties of Silicon nanowires Synthesized by the Vapour−Solid−Solid Mechanism. *Nanotechnology* **2007**, *18* (30), 305606.
(311) Fontcuberta i Morral, A.; Arbiol, J.; Prades, J. D.; Cirera, A.; Morante, J. R. Synthesis of Silicon Nanowires with Wurtzite Crystalline Structure by Using Standard Chemical Vapor Deposition. *Adv. Mater.* **2007**, *19* (10), 1347−1351.
(312) Arbiol, J.; Fontcuberta i Morral, A.; Estradé, S.; Peiró, F.; Kalache, B.; Roca i Cabarrocas, P.; Morante, J. R. Influence of the (111) Twinning on the Formation of Diamond Cubic/Diamond Hexagonal Heterostructures in Cu-Catalyzed Si Nanowires. *J. Appl. Phys.* **2008**, *104* (6), 064312.
(313) Lopez, F. J.; Hemesath, E. R.; Lauhon, L. J. Ordered Stacking Fault Arrays in Silicon Nanowires. *Nano Lett.* **2009**, *9* (7), 2774−9.
(314) Conesa-Boj, S. n.; Zardo, I.; Estradé, S. n.; Wei, L.; Jean Alet, P.; Roca i Cabarrocas, P.; Morante, J. R.; Peiró, F.; Morral, A. F. i.; Arbiol, J. Defect Formation in Ga-Catalyzed Silicon Nanowires. *Cryst. Growth Des.* **2010**, *10* (4), 1534−1543.
(315) Liu, X.; Wang, D. Kinetically-Induced Hexagonality in Chemically Grown Silicon Nanowires. *Nano Res.* **2009**, *2* (7), 575−582.
(316) Lopez, F. J.; Givan, U.; Connell, J. G.; Lauhon, L. J. Silicon Nanowire Polytypes: Identification by Raman Spectroscopy, Generation Mechanism, and Misfit Strain in Homostructures. *ACS Nano* **2011**, *5* (11), 8958−66.
(317) Fabbri, F.; Rotunno, E.; Lazzarini, L.; Cavalcoli, D.; Castaldini, A.; Fukata, N.; Sato, K.; Salviati, G.; Cavallini, A. Preparing the Way for Doping Wurtzite Silicon Nanowires while Retaining the Phase. *Nano Lett.* **2013**, *13* (12), 5900−6.
(318) Fabbri, F.; Rotunno, E.; Lazzarini, L.; Fukata, N.; Salviati, G. Visible and Infra-Red Light Emission in Boron-Doped Wurtzite Silicon Nanowires. *Sci. Rep.* **2015**, *4*, 3603.
(319) Tang, J.; Maurice, J.-L.; Fossard, F.; Florea, I.; Chen, W.; Johnson, E. V.; Foldyna, M.; Yu, L.; Roca i Cabarrocas, P. Natural Occurrence of the Diamond Hexagonal Structure in Silicon Nanowires Grown by a Plasma-Assisted Vapour-Liquid-Solid Method. *Nanoscale* **2017**, *9* (24), 8113−8118.
(320) He, Z.; Maurice, J. L.; Li, Q.; Pribat, D. Direct Evidence of 2H Hexagonal Si in Si Nanowires. *Nanoscale* **2019**, *11* (11), 4846−4853.
(321) Rödl, C.; Sander, T.; Bechstedt, F.; Vidal, J.; Olsson, P.; Laribi, S.; Guillemoles, J. F. Wurtzite Silicon as a Potential Absorber in Photovoltaics: Tailoring the Optical Absorption by Applying Strain. *Phys. Rev. B: Condens. Matter Mater. Phys.* **2015**, *92* (4), 045207.
(322) Amato, M.; Kaewmaraya, T.; Zobelli, A.; Palummo, M.; Rurali, R. Crystal Phase Effects in Si Nanowire Polytypes and Their Homojunctions. *Nano Lett.* **2016**, *16* (9), 5694−700.
(323) Fadaly, E. M. T.; Dijkstra, A.; Suckert, J. R.; Ziss, D.; Tilburg, M. A. J. v.; Mao, C.; Ren, Y.; Lange, V. T. v.; Kölling, S.; Verheijen, M. A.; Busse, D.; Rödl, C.; Furthmüller, J.; Bechstedt, F.; Stangl, J.; Finley, J. J.; Botti, S.; Haverkort, J. E. M.; Bakkers, E. P. A. M. Direct Bandgap Emission from Hexagonal Ge and SiGe Alloys. *arXiv*, 2019, 1911.00726v1 (accessed March 15. 2020).
(324) Pashley, D. W.; Stowell, M. J.; Law, T. J. The Crystal Structure of Evaporated Gold Films. *Phys. Status Solidi B* **1965**, *10* (1), 153−163.
(325) Kohno, H.; Ozaki, N.; Yoshida, H.; Tanaka, K.; Takeda, S. Misleading Fringes in TEM images and Diffraction Patterns of Si Nanocrystallites. *Cryst. Res. Technol.* **2003**, *38* (12), 1082−1086.
(326) Cayron, C.; Den Hertog, M.; Latu-Romain, L.; Mouchet, C.; Secouard, C.; Rouviere, J. L.; Rouviere, E.; Simonato, J. P. Odd Electron Diffraction Patterns in Silicon Nanowires and Silicon Thin Films Explained by Microtwins and Nanotwins. *J. Appl. Crystallogr.* **2009**, *42* (2), 242−252.
(327) He, Z. B.; Stolitchnov, I.; Setter, N.; Cantoni, M.; Wojciechowski, T.; Karczewski, G. HREM Studies of Twins in $Cd_{1-x}Zn_xTe$ ($x \approx 0.04$) Thin Films Grown by Molecular Beam Epitaxy. *J. Alloys Compd.* **2009**, *484* (1−2), 757−762.
(328) den Hertog, M. I.; Cayron, C.; Gentile, P.; Dhalluin, F.; Oehler, F.; Baron, T.; Rouviere, J. L. Hidden Defects in Silicon Nanowires. *Nanotechnology* **2012**, *23* (2), 025701.
(329) Nemeth, P.; Garvie, L. A.; Aoki, T.; Dubrovinskaia, N.; Dubrovinsky, L.; Buseck, P. R. Lonsdaleite is Faulted and Twinned Cubic Diamond and Does Not Exist as a Discrete Material. *Nat. Commun.* **2014**, *5*, 5447.
(330) Dahmen, U.; Westmacott, K. H.; Pirouz, P.; Chaim, R. The Martensitic Transformation in Silicon—II. Crystallographic Analysis. *Acta Metall. Mater.* **1990**, *38* (2), 323−328.
(331) Pirouz, P.; Chaim, R.; Dahmen, U.; Westmacott, K. H. The Martensitic Transformation in Silicon—I Experimental Observations. *Acta Metall. Mater.* **1990**, *38* (2), 313−322.
(332) Pirouz, P.; Dahmen, U.; Westmacott, K. H.; Chaim, R. The Martensitic Transformation in Silicon—III. Comparison With Other Work. *Acta Metall. Mater.* **1990**, *38* (2), 329−336.
(333) Qiu, Y.; Bender, H.; Richard, O.; Kim, M. S.; Van Besien, E.; Vos, I.; de Potter de ten Broeck, M.; Mocuta, D.; Vandervorst, W. Epitaxial Diamond-Hexagonal Silicon Nano-Ribbon growth on (001) Silicon. *Sci. Rep.* **2015**, *5*, 12692.
(334) Vincent, L.; Djomani, D.; Fakfakh, M.; Renard, C.; Belier, B.; Bouchier, D.; Patriarche, G. Shear-Driven Phase Transformation in Silicon Nanowires. *Nanotechnology* **2018**, *29* (12), 125601.
(335) Hauge, H. I. T.; Verheijen, M. A.; Conesa-Boj, S.; Etzelstorfer, T.; Watzinger, M.; Kriegner, D.; Zardo, I.; Fasolato, C.; Capitani, F.; Postorino, P.; Kölling, S.; Li, A.; Assali, S.; Stangl, J.; Bakkers, E. P. A. M. Hexagonal Silicon Realized. *Nano Lett.* **2015**, *15* (9), 5855−5860.
(336) Ren, Y.; Leubner, P.; Verheijen, M. A.; Haverkort, J. E. M.; Bakkers, E. Hexagonal Silicon Grown From Higher Order Silanes. *Nanotechnology* **2019**, *30* (29), 295602.
(337) De, A.; Pryor, C. E. Electronic Structure and Optical Properties of Si, Ge and Diamond in the Lonsdaleite Phase. *J. Phys.: Condens. Matter* **2014**, *26* (4), 045801.
(338) Amato, M.; Ossicini, S.; Canadell, E.; Rurali, R. Preferential Positioning, Stability, and Segregation of Dopants in Hexagonal Si Nanowires. *Nano Lett.* **2019**, *19* (2), 866−876.
(339) Schmidt, V.; Wittemann, J. V.; Gosele, U. Growth, Thermodynamics, and Electrical Properties of Silicon Nanowires. *Chem. Rev.* **2010**, *110* (1), 361−88.
(340) Ramanujam, J.; Shiri, D.; Verma, A. Silicon Nanowire Growth and Properties: A Review. *Mater. Express* **2011**, *1* (2), 105−126.
(341) Lieber, C. M.; Wang, Z. L. Functional Nanowires. *MRS Bull.* **2007**, *32* (2), 99−108.
(342) Putnam, M. C.; Filler, M. A.; Kayes, B. M.; Kelzenberg, M. D.; Guan, Y.; Lewis, N. S.; Eiler, J. M.; Atwater, H. A. Secondary Ion Mass Spectrometry of Vapor−Liquid−Solid Grown, Au-Catalyzed, Si Wires. *Nano Lett.* **2008**, *8* (10), 3109−3113.
(343) Cui, Y.; Duan, X.; Hu, J.; Lieber, C. M. Doping and Electrical Transport in Silicon Nanowires. *J. Phys. Chem. B* **2000**, *104* (22), 5213−5216.
(344) Lew, K.-K.; Pan, L.; Bogart, T. E.; Dilts, S. M.; Dickey, E. C.; Redwing, J. M.; Wang, Y.; Cabassi, M.; Mayer, T. S.; Novak, S. W. Structural and Electrical Properties of Trimethylboron-Doped Silicon Nanowires. *Appl. Phys. Lett.* **2004**, *85* (15), 3101−3103.

(345) Pan, L.; Lew, K.-K.; Redwing, J. M.; Dickey, E. C. Effect of Diborane on the Microstructure of Boron-Doped Silicon Nanowires. *J. Cryst. Growth* **2005**, *277* (1−4), 428−436.
(346) Schlitz, R. A.; Perea, D. E.; Lensch-Falk, J. L.; Hemesath, E. R.; Lauhon, L. J. Correlating Dopant Distributions and Electrical Properties of Boron-Doped Silicon Nanowires. *Appl. Phys. Lett.* **2009**, *95* (16), 162101.
(347) Schmidt, V.; Wittemann, J. V.; Senz, S.; Gösele, U. Silicon Nanowires: A Review on Aspects of their Growth and their Electrical Properties. *Adv. Mater.* **2009**, *21* (25−26), 2681−2702.
(348) Amit, I.; Givan, U.; Connell, J. G.; Paul, D. F.; Hammond, J. S.; Lauhon, L. J.; Rosenwaks, Y. Spatially Resolved Correlation of Active and Total Doping Concentrations in VLS Grown Nanowires. *Nano Lett.* **2013**, *13* (6), 2598−604.
(349) Christesen, J. D.; Pinion, C. W.; Zhang, X.; McBride, J. R.; Cahoon, J. F. Encoding Abrupt and Uniform Dopant Profiles in Vapor-Liquid-Solid Nanowires by Suppressing the Reservoir Effect of the Liquid Catalyst. *ACS Nano* **2014**, *8* (11), 11790−8.
(350) Chou, L. W.; Boyuk, D. S.; Filler, M. A. Optically Abrupt Localized Surface Plasmon Resonances in Si Nanowires by Mitigation of Carrier Density Gradients. *ACS Nano* **2015**, *9* (2), 1250−6.
(351) Pinion, C. W.; Christesen, J. D.; Cahoon, J. F. Understanding the Vapor−Liquid−Solid Mechanism of Si Nanowire Growth and Doping to Synthetically Encode Precise Nanoscale Morphology. *J. Mater. Chem. C* **2016**, *4* (18), 3890−3897.
(352) Kim, S.; Hill, D. J.; Pinion, C. W.; Christesen, J. D.; McBride, J. R.; Cahoon, J. F. Designing Morphology in Epitaxial Silicon Nanowires: The Role of Gold, Surface Chemistry, and Phosphorus Doping. *ACS Nano* **2017**, *11* (5), 4453−4462.
(353) Pinion, C. W.; Nenon, D. P.; Christesen, J. D.; Cahoon, J. F. Identifying crystallization- and incorporation-limited regimes during vapor-liquid-solid growth of Si nanowires. *ACS Nano* **2014**, *8* (6), 6081−8.
(354) Hultin, O.; Otnes, G.; Borgstrom, M. T.; Bjork, M.; Samuelson, L.; Storm, K. Comparing Hall Effect and Field Effect Measurements on the Same Single Nanowire. *Nano Lett.* **2016**, *16* (1), 205−11.
(355) Koren, E.; Rosenwaks, Y.; Allen, J. E.; Hemesath, E. R.; Lauhon, L. J. Nonuniform Doping Distribution Along Silicon Nanowires Measured by Kelvin Probe Force Microscopy and Scanning Photocurrent Microscopy. *Appl. Phys. Lett.* **2009**, *95* (9), 092105.
(356) Sun, Z.; Seidman, D. N.; Lauhon, L. J. Nanowire Kinking Modulates Doping Profiles by Reshaping the Liquid-Solid Growth Interface. *Nano Lett.* **2017**, *17* (7), 4518−4525.
(357) Seifner, M. S.; Sistani, M.; Porrati, F.; Di Prima, G.; Pertl, P.; Huth, M.; Lugstein, A.; Barth, S. Direct Synthesis of Hyperdoped Germanium Nanowires. *ACS Nano* **2018**, *12* (2), 1236−1241.
(358) Jung, L.; Pries, J.; Maß, T. W. W.; Lewin, M.; Boyuk, D. S.; Mohabir, A. T.; Filler, M. A.; Wuttig, M.; Taubner, T. Quantification of Carrier Density Gradients along Axially Doped Silicon Nanowires Using Infrared Nanoscopy. *ACS Photonics* **2019**, *6* (7), 1744−1754.
(359) Fukata, N.; Sato, K.; Mitome, M.; Bando, Y.; Sekiguchi, T.; Kirkham, M.; Hong, J.-i.; Wang, Z. L.; Snyder, R. L. Doping and Raman Characterization of Boron and Phosphorus Atoms in Germanium Nanowires. *ACS Nano* **2010**, *4* (7), 3807−3816.
(360) Hemesath, E. R.; Schreiber, D. K.; Gulsoy, E. B.; Kisielowski, C. F.; Petford-Long, A. K.; Voorhees, P. W.; Lauhon, L. J. Catalyst Incorporation at Defects during Nanowire Growth. *Nano Lett.* **2012**, *12* (1), 167−71.
(361) Christesen, J. D.; Pinion, C. W.; Grumstrup, E. M.; Papanikolas, J. M.; Cahoon, J. F. Synthetically Encoding 10 nm Morphology in Silicon Nanowires. *Nano Lett.* **2013**, *13* (12), 6281−6.
(362) Harmand, J. C.; Patriarche, G.; Glas, F.; Panciera, F.; Florea, I.; Maurice, J. L.; Travers, L.; Ollivier, Y. Atomic Step Flow on a Nanofacet. *Phys. Rev. Lett.* **2018**, *121* (16), 166101.
(363) Hofmann, S.; Sharma, R.; Wirth, C. T.; Cervantes-Sodi, F.; Ducati, C.; Kasama, T.; Dunin-Borkowski, R. E.; Drucker, J.; Bennett, P.; Robertson, J. Ledge-Flow-Controlled Catalyst Interface Dynamics During Si Nanowire Growth. *Nat. Mater.* **2008**, *7* (5), 372−5.
(364) Wen, C. Y.; Tersoff, J.; Reuter, M. C.; Stach, E. A.; Ross, F. M. Step-Flow Kinetics in Nanowire Growth. *Phys. Rev. Lett.* **2010**, *105* (19), 195502.
(365) Galenko, P. Solute Trapping and Diffusionless Solidification in a Binary System. *Phys. Rev. E* **2007**, *76* (3), 031606.
(366) Baeri, P.; Poate, J. M.; Campisano, S. U.; Foti, G.; Rimini, E.; Cullis, A. G. Dependence of Trapping and Segregation of Indium in Silicon on the Velocity of the Liquid-Solid Interface. *Appl. Phys. Lett.* **1980**, *37* (10), 912−914.
(367) Aziz, M. J.; White, C. W. Solute Trapping in Silicon by Lateral Motion of {111} Ledges. *Phys. Rev. Lett.* **1986**, *57* (21), 2675−2678.
(368) Kelly, F. X.; Ungar, L. H. A Molecular Dynamics Investigation of Solute Trapping During Rapid Solidification of Silicon. *J. Cryst. Growth* **1990**, *102* (3), 658−666.
(369) Reitano, R.; Smith, P. M.; Aziz, M. J. Solute Trapping of Group III, IV, and V Elements in Silicon by an Aperiodic Stepwise Growth Mechanism. *J. Appl. Phys.* **1994**, *76* (3), 1518−1529.
(370) Jackson, K. A.; Gilmer, G. H.; Temkin, D. E. Monte Carlo Simulation of the Rapid Crystallization of Bismuth-Doped Silicon. *Phys. Rev. Lett.* **1995**, *75* (13), 2530−2533.
(371) Chagnon, D.; Pippel, E.; Senz, S.; Moutanabbir, O. Metal Seed Loss Throughout the Nanowire Growth: Bulk Trapping and Surface Mass Transport. *J. Phys. Chem. C* **2016**, *120* (5), 2932−2940.
(372) Biswas, S.; Barth, S.; Holmes, J. D. Inducing Imperfections in Germanium Nanowires. *Nano Res.* **2017**, *10* (5), 1510−1523.
(373) Nebol'sin, V. A.; Shchetinin, A. A. Role of Surface Energy in the Vapor−Liquid−Solid Growth of Silicon. *Inorg. Mater.* **2003**, *39* (9), 899−903.
(374) Šilhavík, M.; Müller, M.; Stuchlík, J.; Stuchlíková, H.; Klementová, M.; Kočka, J.; Fejfar, A.; Červenka, J. Comparative Study of Catalyst-Induced Doping and Metal Incorporation in Silicon Nanowires. *Appl. Phys. Lett.* **2019**, *114* (13), 132103.
(375) Baron, T.; Gordon, M.; Dhalluin, F.; Ternon, C.; Ferret, P.; Gentile, P. Si Nanowire Growth and Characterization using a Microelectronics-Compatible Catalyst: PtSi. *Appl. Phys. Lett.* **2006**, *89* (23), 233111.
(376) Johnson, D. C.; Mosby, J. M.; Riha, S. C.; Prieto, A. L. Synthesis of Copper Silicide Nanocrystallites Embedded in Silicon Nanowires for Enhanced Transport Properties. *J. Mater. Chem.* **2010**, *20* (10), 1993.
(377) Wittemann, J. V.; Münchgesang, W.; Senz, S.; Schmidt, V. Silver Catalyzed Ultrathin Silicon Nanowires Grown by Low-Temperature Chemical-Vapor-Deposition. *J. Appl. Phys.* **2010**, *107* (9), 096105.
(378) Yuan, F.-W.; Yang, H.-J.; Tuan, H.-Y. Seeded Silicon Nanowire Growth Catalyzed by Commercially Available Bulk Metals: Broad Selection of Metal Catalysts, Superior Field Emission Performance, and Versatile Nanowire/Metal Architectures. *J. Mater. Chem.* **2011**, *21* (36), 13793.
(379) Wang, Y.; Schmidt, V.; Senz, S.; Gosele, U. Epitaxial Growth of Silicon Nanowires Using an Aluminium Catalyst. *Nat. Nanotechnol.* **2006**, *1* (3), 186−9.
(380) Iacopi, F.; Vereecken, P. M.; Schaekers, M.; Caymax, M.; Moelans, N.; Blanpain, B.; Richard, O.; Detavernier, C.; Griffiths, H. Plasma-Enhanced Chemical Vapour Deposition Growth of Si Nanowires with Low Melting Point Metal Catalysts: an Effective Alternative to Au-Mediated Growth. *Nanotechnology* **2007**, *18* (50), 505307.
(381) Ke, Y.; Weng, X.; Redwing, J. M.; Eichfeld, C. M.; Swisher, T. R.; Mohney, S. E.; Habib, Y. M. Fabrication and Electrical Properties of Si Nanowires Synthesized by Al Catalyzed Vapor-Liquid-Solid Growth. *Nano Lett.* **2009**, *9* (12), 4494−9.
(382) Moutanabbir, O.; Senz, S.; Scholz, R.; Alexe, M.; Kim, Y.; Pippel, E.; Wang, Y.; Wiethoff, C.; Nabbefeld, T.; Meyer zu Heringdorf, F.; Horn-von Hoegen, M. Atomically Smooth p-Doped Silicon Nanowires Catalyzed by Aluminum at Low Temperature. *ACS Nano* **2011**, *5* (2), 1313−20.

https://dx.doi.org/10.1021/acs.chemmater.9b04471
Chem. Mater. 2020, 32, 2703−2741

(383) Moutanabbir, O.; Isheim, D.; Blumtritt, H.; Senz, S.; Pippel, E.; Seidman, D. N. Colossal Injection of Catalyst Atoms into Silicon Nanowires. *Nature* **2013**, *496* (7443), 78−82.
(384) Hainey, M. F.; Redwing, J. M. Aluminum-Catalyzed Silicon Nanowires: Growth methods, Properties, and Applications. *Appl. Phys. Rev.* **2016**, *3* (4), 040806.
(385) Hochbaum, A. I.; Fan, R.; He, R.; Yang, P. Controlled Growth of Si Nanowire Arrays for Device Integration. *Nano Lett.* **2005**, *5* (3), 457−460.
(386) Heitsch, A. T.; Fanfair, D. D.; Tuan, H. Y.; Korgel, B. A. Solution-Liquid-Solid (SLS) Growth of Silicon Nanowires. *J. Am. Chem. Soc.* **2008**, *130* (16), 5436−7.
(387) Dhalluin, F.; Baron, T.; Ferret, P.; Salem, B.; Gentile, P.; Harmand, J. C. Silicon Nanowires: Diameter Dependence of Growth Rate and Delay in Growth. *Appl. Phys. Lett.* **2010**, *96* (13), 133109.
(388) Yu, Z.; Lu, J.; Qian, S.; Misra, S.; Yu, L.; Xu, J.; Xu, L.; Wang, J.; Shi, Y.; Chen, K.; Roca i Cabarrocas, P. Bi-Sn Alloy Catalyst for Simultaneous Morphology and Doping Control of Silicon Nanowires in Radial Junction Solar Cells. *Appl. Phys. Lett.* **2015**, *107* (16), 163105.
(389) Nama Manjunatha, K.; Paul, S. In-Situ Catalyst Mediated Growth and Self-Doped Silicon Nanowires for Use in Nanowire Solar Cells. *Vacuum* **2017**, *139*, 178−184.
(390) Carter, J. D.; Qu, Y.; Porter, R.; Hoang, L.; Masiel, D. J.; Guo, T. Silicon-Based Nanowires from Silicon Wafers Catalyzed by Cobalt Nanoparticles in a Hydrogen Environment. *Chem. Commun.* **2005**, *17*, 2274−6.
(391) Kayes, B. M.; Filler, M. A.; Putnam, M. C.; Kelzenberg, M. D.; Lewis, N. S.; Atwater, H. A. Growth of Vertically Aligned Si Wire Arrays over Large Areas (>1 cm^2) with Au and Cu Catalysts. *Appl. Phys. Lett.* **2007**, *91* (10), 103110.
(392) Schmidt, V.; Senz, S.; Gösele, U. UHV Chemical Vapour Deposition of Silicon Nanowires. *Z. Metallkd.* **2005**, *96* (5), 427−428.
(393) Morales, A. M.; Lieber, C. M. A Laser Ablation Method for the Synthesis of Crystalline Semiconductor Nanowires. *Science* **1998**, *279* (5348), 208−211.
(394) Givargizov, E.I.; Sheftal', N.N. Morphology of Silicon Whiskers Grown by the VLS-Technique. *J. Cryst. Growth* **1971**, *9*, 326−329.
(395) Sunkara, M. K.; Sharma, S.; Miranda, R.; Lian, G.; Dickey, E. C. Bulk Synthesis of Silicon Nanowires Using a Low-Temperature Vapor−Liquid−Solid Method. *Appl. Phys. Lett.* **2001**, *79* (10), 1546−1548.
(396) Bae, J.; Kulkarni, N. N.; Zhou, J. P.; Ekerdt, J. G.; Shih, C.-K. VLS Growth of Si Nanocones using Ga and Al Catalysts. *J. Cryst. Growth* **2008**, *310* (20), 4407−4411.
(397) Ma, L.; Lee, S.; DeMuth, J.; Maldonado, S. Direct Electrochemical Deposition of Crystalline Silicon Nanowires at T ≥ 60 °C. *RSC Adv.* **2016**, *6* (82), 78818−78825.
(398) Wagner, R. S.; Ellis, W. C.; Jackson, K. A.; Arnold, S. M. Study of the Filamentary Growth of Silicon Crystals from the Vapor. *J. Appl. Phys.* **1964**, *35* (10), 2993−3000.
(399) Geaney, H.; Kennedy, T.; Dickinson, C.; Mullane, E.; Singh, A.; Laffir, F.; Ryan, K. M. High Density Growth of Indium Seeded Silicon Nanowires in the Vapor phase of a High Boiling Point Solvent. *Chem. Mater.* **2012**, *24* (11), 2204−2210.
(400) Yu, L.; Xu, M.; Xu, J.; Xue, Z.; Fan, Z.; Picardi, G.; Fortuna, F.; Wang, J.; Xu, J.; Shi, Y.; Chen, K.; Roca i Cabarrocas, P. In-plane Epitaxial Growth of Silicon Nanowires and Junction Formation on Si(100) Substrates. *Nano Lett.* **2014**, *14* (11), 6469−74.
(401) James, D. W. F.; Lewis, C. Silicon Whisker Growth and Epitaxy by the Vapour-Liquid-Solid Mechanism. *Br. J. Appl. Phys.* **1965**, *16* (8), 1089−1094.
(402) Tuan, H. Y.; Lee, D. C.; Hanrath, T.; Korgel, B. A. Catalytic Solid-Phase Seeding of Silicon Nanowires by Nickel Nanocrystals in Organic Solvents. *Nano Lett.* **2005**, *5* (4), 681−4.
(403) Garnett, E. C.; Liang, W.; Yang, P. Growth and Electrical Characteristics of Platinum-Nanoparticle-Catalyzed Silicon Nanowires. *Adv. Mater.* **2007**, *19* (19), 2946−2950.
(404) Chockla, A. M.; Klavetter, K. C.; Mullins, C. B.; Korgel, B. A. Tin-Seeded Silicon Nanowires for High Capacity Li-Ion Batteries. *Chem. Mater.* **2012**, *24* (19), 3738−3745.
(405) Lu, X.; Hessel, C. M.; Yu, Y.; Bogart, T. D.; Korgel, B. A. Colloidal luminescent silicon nanorods. *Nano Lett.* **2013**, *13* (7), 3101−5.
(406) Mullane, E.; Kennedy, T.; Geaney, H.; Dickinson, C.; Ryan, K. M. Synthesis of Tin Catalyzed Silicon and Germanium Nanowires in a Solvent−Vapor System and Optimization of the Seed/Nanowire Interface for Dual Lithium Cycling. *Chem. Mater.* **2013**, *25* (9), 1816−1822.
(407) Kamins, T. I.; Williams, R. S.; Chen, Y.; Chang, Y. L.; Chang, Y. A. Chemical Vapor Deposition of Si Nanowires Nucleated by $TiSi_2$ Islands on Si. *Appl. Phys. Lett.* **2000**, *76* (5), 562−564.
(408) Sharma, S.; Kamins, T. I.; Williams, R. S. Diameter Control of Ti-Catalyzed Silicon Nanowires. *J. Cryst. Growth* **2004**, *267* (3−4), 613−618.
(409) Miyamoto, Y.; Hirata, M. Role of Agents in Filamentary Growth of Amorphous Silicon. *Jpn. J. Appl. Phys.* **1976**, *15* (6), 1159−1160.
(410) Chung, S.-W.; Yu, J.-Y.; Heath, J. R. Silicon Nanowire Devices. *Appl. Phys. Lett.* **2000**, *76* (15), 2068−2070.
(411) Weyher, J. Some Notes on the Growth Kinetics and Morphology of VLS Silicon Crystals Grown with Platinum and Gold as Liquid-Forming Agents. *J. Cryst. Growth* **1978**, *43* (2), 235−244.
(412) Ross, F. M.; Wen, C. Y.; Kodambaka, S.; Wacaser, B. A.; Reuter, M. C.; Stach, E. A. The Growth and Characterization of Si and Ge Nanowires Grown From Reactive Metal Catalysts. *Philos. Mag.* **2010**, *90* (35−36), 4769−4778.
(413) Chou, Y. C.; Wen, C. Y.; Reuter, M. C.; Su, D.; Stach, E. A.; Ross, F. M. Controlling the Growth of Si/Ge Nanowires and Heterojunctions using Silver-Gold Alloy Catalysts. *ACS Nano* **2012**, *6* (7), 6407−15.
(414) Wen, Z.; Stark, J.; Saha, R.; Parker, J.; Kohl, P. A. Fabrication and Electrochemical Performance of Interconnected Silicon Nanowires Synthesized from AlCu Catalyst. *J. Phys. Chem. C* **2013**, *117* (17), 8604−8610.
(415) Murray, J. L.; McAlister, A. J. The Al-Si (Aluminum-Silicon) System. *Bull. Alloy Phase Diagrams* **1984**, *5* (1), 74−84.
(416) Toan, L. D.; Moyen, E.; Zamfir, M. R.; Joe, J.; Kim, Y. W.; Pribat, D. Si Nanowires Grown by Al-Catalyzed Plasma-Enhanced Chemical Vapor Deposition: Synthesis Conditions, Electrical Properties and Application to Lithium Battery Anodes. *Mater. Res. Express* **2016**, *3* (1), 015003.
(417) Allen, J. E.; Hemesath, E. R.; Perea, D. E.; Lensch-Falk, J. L.; Li, Z. Y.; Yin, F.; Gass, M. H.; Wang, P.; Bleloch, A. L.; Palmer, R. E.; Lauhon, L. J. High-Resolution Detection of Au Catalyst Atoms in Si Nanowires. *Nat. Nanotechnol.* **2008**, *3* (3), 168−73.
(418) Kelzenberg, M. D.; Turner-Evans, D. B.; Kayes, B. M.; Filler, M. A.; Putnam, M. C.; Lewis, N. S.; Atwater, H. A. Photovoltaic Measurements in Single-Nanowire Silicon Solar Cells. *Nano Lett.* **2008**, *8* (2), 710−4.
(419) Yu, J.-Y.; Chung, S.-W.; Heath, J. R. Silicon Nanowires: Preparation, Device Fabrication, and Transport Properties. *J. Phys. Chem. B* **2000**, *104* (50), 11864−11870.
(420) Olesinski, R. W.; Abbaschian, G. J. The Bi−Si (Bismuth-Silicon) System. *Bull. Alloy Phase Diagrams* **1985**, *6* (4), 359−361.
(421) Olesinski, R. W.; Abbaschian, G. J. The Si-Zn (Silicon-Zinc) System. *Bull. Alloy Phase Diagrams* **1985**, *6* (6), 545−548.
(422) Olesinski, R. W.; Kanani, N.; Abbaschian, G. J. The In−Si (Indium-Silicon) System. *Bull. Alloy Phase Diagrams* **1985**, *6* (2), 128−130.
(423) Backenstoss, G. Conductivity Mobilities of Electrons and Holes in Heavily Doped Silicon. *Phys. Rev.* **1957**, *108* (6), 1416−1419.
(424) Hill, D. J.; Teitsworth, T. S.; Kim, S.; Christesen, J. D.; Cahoon, J. F. Encoding Highly Nonequilibrium Boron Concen-

https://dx.doi.org/10.1021/acs.chemmater.9b04471
Chem. Mater. 2020, 32, 2703−2741

trations and Abrupt Morphology in p-Type/n-Type Silicon Nanowire Superlattices. *ACS Appl. Mater. Interfaces* **2017**, *9* (42), 37105−37111.
(425) Fung, W. Y.; Lu, W. Growth and Electrical Properties of Al-Catalyzed Si Nanowires. *Appl. Phys. Lett.* **2011**, *98* (3), 033108.
(426) Dayeh, S. A.; Mack, N. H.; Huang, J. Y.; Picraux, S. T. Advanced Core/Multishell Germanium/Silicon Nanowire Heterostructures: The Au-Diffusion Bottleneck. *Appl. Phys. Lett.* **2011**, *99* (2), 023102.
(427) Conesa-Boj, S.; Li, A.; Koelling, S.; Brauns, M.; Ridderbos, J.; Nguyen, T. T.; Verheijen, M. A.; Koenraad, P. M.; Zwanenburg, F. A.; Bakkers, E. P. A. M. Boosting Hole Mobility in Coherently Strained [110]-Oriented Ge−Si Core−Shell Nanowires. *Nano Lett.* **2017**, *17* (4), 2259−2264.
(428) Goldthorpe, I. A.; Marshall, A. F.; McIntyre, P. C. Synthesis and Strain Relaxation of Ge-Core/Si-Shell Nanowire Arrays. *Nano Lett.* **2008**, *8* (11), 4081−4086.
(429) Kohen, D.; Cayron, C.; De Vito, E.; Tileli, V.; Faucherand, P.; Morin, C.; Brioude, A.; Perraud, S. Aluminum Catalyzed Growth of Silicon Nanowires: Al Atom Location and the Influence of Silicon Precursor Pressure on the Morphology. *J. Cryst. Growth* **2012**, *341* (1), 12−18.
(430) Lu, X.; Bogart, T. D.; Gu, M.; Wang, C.; Korgel, B. A. In Situ TEM Observations of Sn-Containing Silicon Nanowires Undergoing Reversible Pore Formation Due to Fast Lithiation/Delithiation Kinetics. *J. Phys. Chem. C* **2015**, *119* (38), 21889−21895.
(431) Ceylan, A.; Gumrukcu, A. E.; Akin, N.; Ozcan, S.; Ozcelik, S. Formation of ST12 Phase Ge Nanoparticles in ZnO Thin Films. *Mater. Sci. Semicond. Process.* **2015**, *40*, 407−411.
(432) Rath, S.; Sato, S.; Ono, H.; Nozaki, S.; Morisaki, H. Evidence of a Tetragonal Structure of Germanium Nanocrystals Prepared by the Cluster-Beam Deposition Technique. *Mater. Chem. Phys.* **1998**, *54* (1), 244−246.
(433) Saito, Y. Crystal Structure and Habit of Silicon and Germanium Particles Grown in Argon Gas. *J. Cryst. Growth* **1979**, *47* (1), 61−72.
(434) Liu, J.; Liang, C.; Tian, Z.; Zhang, S.; Shao, G. Spontaneous Growth and Chemical Reduction Ability of Ge Nanoparticles. *Sci. Rep.* **2013**, *3* (1), 1741.
(435) Kim, S. J.; Quy, O. K.; Chang, L.-S.; Stach, E. A.; Handwerker, C. A.; Wei, A. Formation of the ST12 Phase in Nanocrystalline Ge at Ambient Pressure. *J. Mater. Chem.* **2010**, *20* (2), 331−337.
(436) Cho, Y. J.; Im, H. S.; Kim, H. S.; Myung, Y.; Back, S. H.; Lim, Y. R.; Jung, C. S.; Jang, D. M.; Park, J.; Cha, E. H.; Cho, W. I.; Shojaei, F.; Kang, H. S. Tetragonal Phase Germanium Nanocrystals in Lithium Ion Batteries. *ACS Nano* **2013**, *7* (10), 9075−9084.
(437) Pizzagalli, L.; Galli, G.; Klepeis, J. E.; Gygi, F. Structure and Stability of Germanium Nanoparticles. *Phys. Rev. B: Condens. Matter Mater. Phys.* **2001**, *63* (16), 165324.
(438) Zhao, Z.; Zhang, H.; Kim, D. Y.; Hu, W.; Bullock, E. S.; Strobel, T. A. Properties of the Exotic Metastable ST12 Germanium Allotrope. *Nat. Commun.* **2017**, *8* (1), 13909.
(439) Ruddy, D. A.; Erslev, P. T.; Habas, S. E.; Seabold, J. A.; Neale, N. R. Surface Chemistry Exchange of Alloyed Germanium Nanocrystals: A Pathway Toward Conductive Group IV Nanocrystal Films. *J. Phys. Chem. Lett.* **2013**, *4* (3), 416−421.
(440) McAlister, A. J.; Murray, J. L. The Al-Ge (Aluminum-Germanium) System. *Bull. Alloy Phase Diagrams* **1984**, *5* (4), 341.
(441) Olesinski, R. W.; Abbaschian, G. J. The Ga−Ge (Gallium-Germanium) System. *Bull. Alloy Phase Diagrams* **1985**, *6* (3), 258−262.
(442) Olesinki, R. W.; Kanani, N.; Abbaschian, G. J. The Ge-In (Germanium-Indium) System. *Bull. Alloy Phase Diagrams* **1985**, *6* (6), 536−539.
(443) Olesinski, R. W.; Kanani, N.; Abbaschian, G. J. The Ge−P (Germanium-Phosphorus) System. *Bull. Alloy Phase Diagrams* **1985**, *6* (3), 262−266.
(444) Olesinski, R. W.; Abbaschian, G. J. The As−Ge (Arsenic-Germanium) System. *Bull. Alloy Phase Diagrams* **1985**, *6* (3), 250−254.
(445) Luther, J. M.; Jain, P. K.; Ewers, T.; Alivisatos, A. P. Localized Surface Plasmon Resonances Arising From Free Carriers in Doped Quantum Dots. *Nat. Mater.* **2011**, *10* (5), 361−366.
(446) Ochsenbein, S. T.; Feng, Y.; Whitaker, K. M.; Badaeva, E.; Liu, W. K.; Li, X.; Gamelin, D. R. Charge-Controlled Magnetism in Colloidal Doped Semiconductor Nanocrystals. *Nat. Nanotechnol.* **2009**, *4* (10), 681−687.
(447) Gao, Y.; Pi, X.; Wang, X.; Yuan, T.; Jiang, Q.; Gresback, R.; Lu, J.; Yang, D. Structures, Oxidation, and Charge Transport of Phosphorus-Doped Germanium Nanocrystals. *Part. Part. Syst. Charact.* **2016**, *33* (5), 271−278.
(448) Tabatabaei, K.; Lu, H.; Nolan, B. M.; Cen, X.; McCold, C. E.; Zhang, X.; Brutchey, R. L.; van Benthem, K.; Hihath, J.; Kauzlarich, S. M. Bismuth Doping of Germanium Nanocrystals through Colloidal Chemistry. *Chem. Mater.* **2017**, *29* (17), 7353−7363.
(449) Olesinski, R. W.; Abbaschian, G. J. The Bi−Ge (Bismuth-Germanium) System. *Bull. Alloy Phase Diagrams* **1986**, *7* (6), 535−540.
(450) Xiu, F. Magnetic Mn-Doped Ge Nanostructures. *ISRN Condens. Matter Phys.* **2012**, *2012*, 198590.
(451) Jungwirth, T.; Sinova, J.; Mašek, J.; Kučera, J.; MacDonald, A. H. Theory of Ferromagnetic (III,Mn)V Semiconductors. *Rev. Mod. Phys.* **2006**, *78* (3), 809−864.
(452) McLeod, M.; Tabor, C. Tunable Conductivity of Germanium Thin Films Fabricated via Doped Colloidal Nanoparticle Sintering. *J. Phys. Chem. C* **2019**, *123* (2), 1477−1482.
(453) Gastaldo, D.; Conta, G.; Coïsson, M.; Amato, G.; Tiberto, P.; Allia, P. Growth of Room Temperature Ferromagnetic $Ge_{1-x}Mn_x$ Quantum Dots on Hydrogen Passivated Si (100) Surfaces. *AIP Adv.* **2018**, *8* (5), 056414.
(454) Tardif, S.; Yu, I.-S.; Devillers, T.; Jamet, M.; Cherifi, S.; Cibert, J.; Barski, A.; Bayle-Guillemaud, P.; Bellet-Amalric, E. In From Diluted Magnetic Semiconductors to Self-Organized Nanocolumns of GeMn in Germanium. *Spintronics*; Razeghi, M., Drouhin, H.-J. M., Wegrowe, J.-E., Eds.; SPIE: San Diego, CA, U.S.A., 2008; p 703615.
(455) Gokhale, A. B.; Abbaschian, R. The Ge-Mn (Germanium-Manganese) System. *J. Phase Equilib.* **1990**, *11* (5), 460−468.
(456) Xiu, F.; Wang, Y.; Kou, X.; Upadhyaya, P.; Zhou, Y.; Zou, J.; Wang, K. L. Synthesis of High-Curie-Temperature $Fe_{0.02}Ge_{0.98}$ Quantum Dots. *J. Am. Chem. Soc.* **2010**, *132* (33), 11425−11427.
(457) Baira, M.; Aljaghwani, M.; Salem, B.; Madhar, N. A.; Ilahi, B. Investigation of GeSn/Ge Quantum Dots' Optical Transitions for Integrated Optics on Si Substrate. *Results Phys.* **2019**, *12*, 1732−1736.
(458) Baira, M.; Salem, B.; Madhar, N. A.; Ilahi, B. Tuning Direct Bandgap GeSn/Ge Quantum Dots' Interband and Intraband useful Emission Wavelength: Towards CMOS Compatible Infrared Optical Devices. *Superlattices Microstruct.* **2018**, *117*, 31−35.
(459) Nakamura, Y.; Masada, A.; Cho, S.-P.; Tanaka, N.; Ichikawa, M. Epitaxial Growth of Ultrahigh Density $Ge_{1-x}Sn_x$ Quantum Dots on Si (111) Substrates by Codeposition of Ge and Sn on Ultrathin SiO_2 Films. *J. Appl. Phys.* **2007**, *102* (12), 124302.
(460) Nakamura, Y.; Masada, A.; Ichikawa, M. Quantum-Confinement Effect in Individual $Ge_{1-x}Sn_x$ Quantum Dots on Si(111) Substrates Covered with Ultrathin SiO_2 Films using Scanning Tunneling Spectroscopy. *Appl. Phys. Lett.* **2007**, *91* (1), 013109.
(461) Naruse, N.; Mera, Y.; Nakamura, Y.; Ichikawa, M.; Maeda, K. Fourier-Transform Photoabsorption Spectroscopy of Quantum-confinement Effects in Individual GeSn Nanodots. *Appl. Phys. Lett.* **2009**, *94* (9), 093104.
(462) Nakamura, Y.; Fujinoki, N.; Ichikawa, M. Photoluminescence From Si-Capped GeSn Nanodots on Si Substrates Formed Using an Ultrathin SiO_2 Film Technique. *J. Appl. Phys.* **2009**, *106* (1), 014309.
(463) Okamoto, H.; Takita, K.; Tsushima, K.; Tawara, T.; Tateno, K.; Zhang, G.; Gotoh, H. Low-Temperature Formation of GeSn Nanodots by Sn Mediation. *Jpn. J. Appl. Phys.* **2019**, *58* (SD), SDDG09.
(464) Tonkikh, A. A.; Zakharov, N. D.; Suvorova, A. A.; Eisenschmidt, C.; Schilling, J.; Werner, P. Cubic Phase Sn-Rich

https://dx.doi.org/10.1021/acs.chemmater.9b04471
Chem. Mater. 2020, 32, 2703−2741

GeSn Nanocrystals in a Ge Matrix. *Cryst. Growth Des.* **2014**, *14* (4), 1617−1622.
(465) Ragan, R.; Atwater, H. A. Diamond Cubic Sn-Rich Nanocrystals: Ssynthesis, Microstructure and Optical Properties. *Appl. Phys. A: Mater. Sci. Process.* **2005**, *80* (6), 1335−1338.
(466) Zhang, L.; Hong, H.; Li, C.; Chen, S.; Huang, W.; Wang, J.; Wang, H. High-Sn Fraction GeSn Quantum Dots for Si-Based Light Source at 1.55 μm. *Appl. Phys. Express* **2019**, *12* (5), 055504.
(467) Di Bartolomeo, A.; Passacantando, M.; Niu, G.; Schlykow, V.; Lupina, G.; Giubileo, F.; Schroeder, T. Observation of Field Emission from GeSn Nanoparticles Epitaxially Grown on Silicon Nanopillar Arrays. *Nanotechnology* **2016**, *27* (48), 485707.
(468) Schlykow, V.; Zaumseil, P.; Schubert, M. A.; Skibitzki, O.; Yamamoto, Y.; Klesse, W. M.; Hou, Y.; Virgilio, M.; De Seta, M.; Di Gaspare, L.; Schroeder, T.; Capellini, G. Photoluminescence from GeSn Nano-Heterostructures. *Nanotechnology* **2018**, *29* (41), 415702.
(469) Schlykow, V.; Klesse, W. M.; Niu, G.; Taoka, N.; Yamamoto, Y.; Skibitzki, O.; Barget, M. R.; Zaumseil, P.; von Känel, H.; Schubert, M. A.; Capellini, G.; Schroeder, T. Selective Growth of Fully Relaxed GeSn Nano-Islands by Nanoheteroepitaxy on Patterned Si(001). *Appl. Phys. Lett.* **2016**, *109* (20), 202102.
(470) Ramasamy, K.; Kotula, P. G.; Modine, N.; Brumbach, M. T.; Pietryga, J. M.; Ivanov, S. A. Cubic SnGe Nanoalloys: Beyond Thermodynamic Composition Limit. *Chem. Commun.* **2019**, *55* (19), 2773−2776.
(471) Ramasamy, K.; Kotula, P. G.; Fidler, A. F.; Brumbach, M. T.; Pietryga, J. M.; Ivanov, S. A. Sn_xGe_{1-x} Alloy Nanocrystals: A First Step toward Solution-Processed Group IV Photovoltaics. *Chem. Mater.* **2015**, *27* (13), 4640−4649.
(472) Esteves, R. J. A.; Ho, M. Q.; Arachchige, I. U. Nanocrystalline Group IV Alloy Semiconductors: Synthesis and Characterization of $Ge_{1-x}Sn_x$ Quantum Dots for Tunable Bandgaps. *Chem. Mater.* **2015**, *27* (5), 1559−1568.
(473) Tallapally, V.; Nakagawara, T. A.; Demchenko, D. O.; Özgür, Ü.; Arachchige, I. U. $Ge_{1-x}Sn_x$ Alloy Quantum Dots with Composition-Tunable Energy Gaps and Near-Infrared Photoluminescence. *Nanoscale* **2018**, *10* (43), 20296−20305.
(474) Bodnarchuk, M. I.; Kravchyk, K. V.; Krumeich, F.; Wang, S.; Kovalenko, M. V. Colloidal Tin−Germanium Nanorods and Their Li-Ion Storage Properties. *ACS Nano* **2014**, *8* (3), 2360−2368.
(475) Hafiz, S. A.; Esteves, R. J. A.; Demchenko, D. O.; Arachchige, I. U.; Özgür, Ü. Energy Gap Tuning and Carrier Dynamics in Colloidal $Ge_{1-x}Sn_x$ Quantum Dots. *J. Phys. Chem. Lett.* **2016**, *7* (17), 3295−3301.
(476) Xu, C.; Senaratne, C. L.; Culbertson, R. J.; Kouvetakis, J.; Menéndez, J. Deviations from Vegard's Law in Semiconductor Thin Films Measured with X-ray Diffraction and Rutherford Backscattering: The $Ge_{1-y}Sn_y$ and $Ge_{1-x}Si_x$ Cases. *J. Appl. Phys.* **2017**, *122* (12), 125702.
(477) Seifner, M. S.; Hernandez, S.; Bernardi, J.; Romano-Rodriguez, A.; Barth, S. Pushing the Composition Limit of Anisotropic $Ge_{1-x}Sn_x$ Nanostructures and Determination of Their Thermal Stability. *Chem. Mater.* **2017**, *29* (22), 9802−9813.
(478) Alan Esteves, R. J.; Hafiz, S.; Demchenko, D. O.; Ozgur, U.; Arachchige, I. U. Ultra-Small $Ge_{1-x}Sn_x$ Quantum Dots with Visible Photoluminescence. *Chem. Commun.* **2016**, *52* (78), 11665−11668.
(479) Shirahata, N.; Hirakawa, D.; Masuda, Y.; Sakka, Y. Size-Dependent Color Tuning of Efficiently Luminescent Germanium Nanoparticles. *Langmuir* **2013**, *29* (24), 7401−7410.
(480) Ruddy, D. A.; Johnson, J. C.; Smith, E. R.; Neale, N. R. Size and Bandgap Control in the Solution-Phase Synthesis of Near-Infrared-Emitting Germanium Nanocrystals. *ACS Nano* **2010**, *4* (12), 7459−7466.
(481) Wheeler, L. M.; Levij, L. M.; Kortshagen, U. R. Tunable Band Gap Emission and Surface Passivation of Germanium Nanocrystals Synthesized in the Gas Phase. *J. Phys. Chem. Lett.* **2013**, *4* (20), 3392−3396.
(482) Takeoka, S.; Fujii, M.; Hayashi, S.; Yamamoto, K. Size-Dependent Near-Infrared Photoluminescence From Ge Nanocrystals Embedded in SiO_2 matrices. *Phys. Rev. B: Condens. Matter Mater. Phys.* **1998**, *58* (12), 7921−7925.
(483) Holman, Z. C.; Kortshagen, U. R. Absolute Absorption Cross Sections of Ligand-Free Colloidal Germanium Nanocrystals. *Appl. Phys. Lett.* **2012**, *100* (13), 133108.
(484) Carolan, D.; Doyle, H. Tuning the Photoluminescence of Germanium Nanocrystals through Surface Bound Functional Groups. *Part. Part. Syst. Charact.* **2017**, *34* (2), 1600303.
(485) Takeoka, S.; Fujii, M.; Hayashi, S.; Yamamoto, K. Size-dependent near-infrared photoluminescence from Ge nanocrystals embedded in ${\mathrm{SiO}}_{2}$ matrices. *Phys. Rev. B: Condens. Matter Mater. Phys.* **1998**, *58* (12), 7921−7925.
(486) Lee, D. C.; Pietryga, J. M.; Robel, I.; Werder, D. J.; Schaller, R. D.; Klimov, V. I. Colloidal Synthesis of Infrared-Emitting Germanium Nanocrystals. *J. Am. Chem. Soc.* **2009**, *131* (10), 3436−3437.
(487) Vincent, L.; Patriarche, G.; Hallais, G.; Renard, C.; Gardès, C.; Troadec, D.; Bouchier, D. Novel Heterostructured Ge Nanowires Based on Polytype Transformation. *Nano Lett.* **2014**, *14* (8), 4828−4836.
(488) Fasolato, C.; De Luca, M.; Djomani, D.; Vincent, L.; Renard, C.; Di Iorio, G.; Paillard, V.; Amato, M.; Rurali, R.; Zardo, I. Crystalline, Phononic, and Electronic Properties of Heterostructured Polytypic Ge Nanowires by Raman Spectroscopy. *Nano Lett.* **2018**, *18* (11), 7075−7084.
(489) Kaewmaraya, T.; Vincent, L.; Amato, M. Accurate Estimation of Band Offsets in Group IV Polytype Junctions: A First-Principles Study. *J. Phys. Chem. C* **2017**, *121* (10), 5820−5828.
(490) Cartoixà, X.; Palummo, M.; Hauge, H. I. T.; Bakkers, E. P. A. M.; Rurali, R. Optical Emission in Hexagonal SiGe Nanowires. *Nano Lett.* **2017**, *17* (8), 4753−4758.
(491) Hauge, H. I. T.; Conesa-Boj, S.; Verheijen, M. A.; Koelling, S.; Bakkers, E. P. A. M. Single-Crystalline Hexagonal Silicon−Germanium. *Nano Lett.* **2017**, *17* (1), 85−90.
(492) De Luca, M.; Polimeni, A. Electronic Properties of Wurtzite-Phase InP Nanowires Determined by Optical and Magneto-Optical Spectroscopy. *Appl. Phys. Rev.* **2017**, *4* (4), 041102.
(493) Haverkort, J. E. M.; Ren, Y.; Dijkstra, A.; Fadaly, E.; Verheijen, M. A.; Reithmaier, G.; Busse, D.; Botti, S.; Finley, J. J.; Bakkers, E. P. A. M. Light Emission from Direct Bandgap Hexagonal SiGe; *Advanced Photonics 2018* (BGPP, IPR, NP, NOMA, Sensors, Networks, SPPCom, SOF), Zurich, 2018/07/02; Optical Society of America: Zurich, 2018; p ITu4I.5.
(494) Shen, Y.; Meng, X.; Cheng, Q.; Rumley, S.; Abrams, N.; Gazman, A.; Manzhosov, E.; Glick, M. S.; Bergman, K. Silicon Photonics for Extreme Scale Systems. *J. Lightwave Technol.* **2019**, *37* (2), 245−259.
(495) Wang, R. J.; Vasiliev, A.; Muneeb, M.; Malik, A.; Sprengel, S.; Boehm, G.; Amann, M. C.; Simonyte, I.; Vizbaras, A.; Vizbaras, K.; Baets, R.; Roelkens, G. III-V-on-Silicon Photonic Integrated Circuits for Spectroscopic Sensing in the 2−4 mu m Wavelength Range. *Sensors* **2017**, *17* (8), 1788.
(496) Wang, J.; Paesani, S.; Ding, Y.; Santagati, R.; Skrzypczyk, P.; Salavrakos, A.; Tura, J.; Augusiak, R.; Mančinska, L.; Bacco, D.; Bonneau, D.; Silverstone, J. W.; Gong, Q.; Acín, A.; Rottwitt, K.; Oxenløwe, L. K.; O'Brien, J. L.; Laing, A.; Thompson, M. G. Multidimensional Quantum Entanglement with Large-Scale Integrated Optics. *Science* **2018**, *360* (6386), 285−291.
(497) Thomson, D.; Zilkie, A.; Bowers, J. E.; Komljenovic, T.; Reed, G. T.; Vivien, L.; Marris-Morini, D.; Cassan, E.; Virot, L.; Fédéli, J.-M.; Hartmann, J.-M.; Schmid, J. H.; Xu, D.-X.; Boeuf, F.; O'Brien, P.; Mashanovich, G. Z.; Nedeljkovic, M. Roadmap on Silicon Photonics. *J. Opt.* **2016**, *18* (7), 073003.
(498) Assali, S.; Dijkstra, A.; Li, A.; Koelling, S.; Verheijen, M. A.; Gagliano, L.; von den Driesch, N.; Buca, D.; Koenraad, P. M.; Haverkort, J. E. M.; Bakkers, E. P. A. M. Growth and Optical Properties of Direct Band Gap $Ge/Ge_{0.87}Sn_{0.13}$ Core/Shell Nanowire Arrays. *Nano Lett.* **2017**, *17* (3), 1538−1544.
(499) Meng, A. C.; Fenrich, C. S.; Braun, M. R.; McVittie, J. P.; Marshall, A. F.; Harris, J. S.; McIntyre, P. C. Core-Shell Germanium/

Germanium−Tin Nanowires Exhibiting Room-Temperature Direct- and Indirect-Gap Photoluminescence. *Nano Lett.* **2016**, *16* (12), 7521−7529.
(500) Albani, M.; Assali, S.; Verheijen, M. A.; Koelling, S.; Bergamaschini, R.; Pezzoli, F.; Bakkers, E. P. A. M.; Miglio, L. Critical Strain for Sn Incorporation into Spontaneously Graded Ge/GeSn Core/Shell Nanowires. *Nanoscale* **2018**, *10* (15), 7250−7256.
(501) Assali, S.; Albani, M.; Bergamaschini, R.; Verheijen, M. A.; Li, A.; Kölling, S.; Gagliano, L.; Bakkers, E. P. A. M.; Miglio, L. Strain Engineering in Ge/GeSn Core/Shell Nanowires. *Appl. Phys. Lett.* **2019**, *115* (11), 113102.
(502) Sánchez-Pérez, J. R.; Boztug, C.; Chen, F.; Sudradjat, F. F.; Paskiewicz, D. M.; Jacobson, R.; Lagally, M. G.; Paiella, R. Direct-Bandgap Light-Emitting Germanium in Tensilely Strained Nanomembranes. *Proc. Natl. Acad. Sci. U. S. A.* **2011**, *108* (47), 18893−18898.
(503) Assali, S.; Bergamaschini, R.; Scalise, E.; Verheijen, M. A.; Albani, M.; Dijkstra, A.; Li, A.; Koelling, S.; Bakkers, E. P. A. M.; Montalenti, F.; Miglio, L. Kinetic Control of Morphology and Composition in Ge/GeSn Core/Shell Nanowires. *ACS Nano* **2020**, *14* (2), 2445−2455.
(504) Xiu, F.; Wang, Y.; Kim, J.; Hong, A.; Tang, J.; Jacob, A. P.; Zou, J.; Wang, K. L. Electric-Field-Controlled Ferromagnetism in High-Curie-Temperature $Mn_{0.05}Ge_{0.95}$ Quantum dots. *Nat. Mater.* **2010**, *9* (4), 337−344.
(505) van der Meulen, M. I.; Petkov, N.; Morris, M. A.; Kazakova, O.; Han, X.; Wang, K. L.; Jacob, A. P.; Holmes, J. D. Single Crystalline $Ge_{1-x}Mn_x$ Nanowires as Building Blocks for Nanoelectronics. *Nano Lett.* **2009**, *9* (1), 50−56.
(506) Barth, S.; Kazakova, O.; Estrade, S.; Hobbs, R. G.; Peiro, F.; Morris, M. A.; Holmes, J. D. Synthesis and Magnetic Characterization of Coaxial $Ge_{1-x}Mn_x$/a-Si Heterostructures. *Cryst. Growth Des.* **2011**, *11* (12), 5253−5259.
(507) Grossi, V.; Bussolotti, F.; Passacantando, M.; Santucci, S.; Ottaviano, L. Mn Doping of Germanium Nanowires by Vapour−Liquid−Solid Deposition. *Superlattices Microstruct.* **2008**, *44* (4), 489−495.
(508) Biswas, S.; Doherty, J.; Saladukha, D.; Ramasse, Q.; Majumdar, D.; Upmanyu, M.; Singha, A.; Ochalski, T.; Morris, M. A.; Holmes, J. D. Non-Equilibrium Induction of Tin in Germanium: Towards Direct Bandgap $Ge_{1-x}Sn_x$ Nanowires. *Nat. Commun.* **2016**, *7*, 11405.
(509) Doherty, J.; Biswas, S.; Saladukha, D.; Ramasse, Q.; Bhattacharya, T. S.; Singha, A.; Ochalski, T. J.; Holmes, J. D. Influence of Growth Kinetics on Sn Incorporation in Direct Band Gap $Ge_{1-x}Sn_x$ Nanowires. *J. Mater. Chem. C* **2018**, *6* (32), 8738−8750.
(510) Doherty, J.; Biswas, S.; McNulty, D.; Downing, C.; Raha, S.; O'Regan, C.; Singha, A.; O'Dwyer, C.; Holmes, J. D. One-Step Fabrication of GeSn Branched Nanowires. *Chem. Mater.* **2019**, *31* (11), 4016−4024.
(511) Kennedy, T.; Brandon, M.; Ryan, K. M. Advances in the Application of Silicon and Germanium Nanowires for High-Performance Lithium-Ion Batteries. *Adv. Mater.* **2016**, *28* (27), 5696−5704.
(512) Li, X.; Yang, Z.; Fu, Y.; Qiao, L.; Li, D.; Yue, H.; He, D. Germanium Anode with Excellent Lithium Storage Performance in a Germanium/Lithium−Cobalt Oxide Lithium-Ion Battery. *ACS Nano* **2015**, *9* (2), 1858−1867.
(513) Haffner, T.; Zeghouane, M.; Bassani, F.; Gentile, P.; Gassenq, A.; Chouchane, F.; Pauc, N.; Martinez, E.; Robin, E.; David, S.; Baron, T.; Salem, B. Growth of $Ge_{1-x}Sn_x$ Nanowires by Chemical Vapor Deposition *via* Vapor−Liquid−Solid Mechanism Using GeH_4 and $SnCl_4$. *Phys. Status Solidi A* **2018**, *215* (1), 1700743.
(514) Sun, Y.-L.; Matsumura, R.; Jevasuwan, W.; Fukata, N. Au−Sn Catalyzed Growth of $Ge_{1-x}Sn_x$ Nanowires: Growth Direction, Crystallinity, and Sn Incorporation. *Nano Lett.* **2019**, *19* (9), 6270−6277.
(515) Seifner, M. S.; Dijkstra, A.; Bernardi, J.; Steiger-Thirsfeld, A.; Sistani, M.; Lugstein, A.; Haverkort, J. E. M.; Barth, S. Epitaxial $Ge_{0.81}Sn_{0.19}$ Nanowires for Nanoscale Mid-Infrared Emitters. *ACS Nano* **2019**, *13* (7), 8047−8054.
(516) Gayer, K. H.; Zajicek, O. T. The Solubility of Germanium (IV) Oxide in Aqueous NaOH Solutions at 25°C. *J. Inorg. Nucl. Chem.* **1964**, *26* (6), 951−954.
(517) Liang, X.; Kim, Y.-G.; Gebergziabiher, D. K.; Stickney, J. L. Aqueous Electrodeposition of Ge Monolayers. *Langmuir* **2010**, *26* (4), 2877−2884.
(518) Mahenderkar, N. K.; Liu, Y.-C.; Koza, J. A.; Switzer, J. A. Electrodeposited Germanium Nanowires. *ACS Nano* **2014**, *8* (9), 9524−9530.
(519) Fahrenkrug, E.; Biehl, J.; Maldonado, S. Electrochemical Liquid−Liquid−Solid Crystal Growth of Germanium Microwires on Hard and Soft Conductive Substrates at Low Temperature in Aqueous Solution. *Chem. Mater.* **2015**, *27* (9), 3389−3396.
(520) Fahrenkrug, E.; Gu, J.; Jeon, S.; Veneman, P. A.; Goldman, R. S.; Maldonado, S. Room-Temperature Epitaxial Electrodeposition of Single-Crystalline Germanium Nanowires at the Wafer Scale from an Aqueous Solution. *Nano Lett.* **2014**, *14* (2), 847−852.
(521) Acharya, S.; Ma, L.; Maldonado, S. Critical Factors in the Growth of Hyperdoped Germanium Microwires by Electrochemical Liquid−Liquid−Solid Method. *ACS Appl. Nano Mater.* **2018**, *1* (10), 5553−5561.
(522) DeMuth, J.; Ma, L.; Lancaster, M.; Acharya, S.; Cheek, Q.; Maldonado, S. Eutectic-Bismuth Indium as a Growth Solvent for the Electrochemical Liquid-Liquid-Solid Deposition of Germanium Microwires and Coiled Nanowires. *Cryst. Growth Des.* **2018**, *18* (2), 677−685.
(523) Ma, L.; Gu, J.; Fahrenkrug, E.; Maldonado, S. Electrochemical Liquid-Liquid-Solid Deposition of Crystalline Ge Nanowires as a Function of Ga Nanodroplet Size. *J. Electrochem. Soc.* **2014**, *161* (7), D3044−D3050.
(524) Carim, A. I.; Collins, S. M.; Foley, J. M.; Maldonado, S. Benchtop Electrochemical Liquid−Liquid−Solid Growth of Nanostructured Crystalline Germanium. *J. Am. Chem. Soc.* **2011**, *133* (34), 13292−13295.
(525) Sistani, M.; Seifner, M. S.; Bartmann, M. G.; Smoliner, J.; Lugstein, A.; Barth, S. Electrical Characterization and Examination of Temperature-Induced Degradation of Metastable $Ge_{0.81}Sn_{0.19}$ Nanowires. *Nanoscale* **2018**, *10* (41), 19443−19449.
(526) Aghazadeh Meshgi, M.; Biswas, S.; McNulty, D.; O'Dwyer, C.; Alessio Verni, G.; O'Connell, J.; Davitt, F.; Letofsky-Papst, I.; Poelt, P.; Holmes, J. D.; Marschner, C. Rapid, Low-Temperature Synthesis of Germanium Nanowires from Oligosilylgermane Precursors. *Chem. Mater.* **2017**, *29* (10), 4351−4360.
(527) Pertl, P.; Seifner, M. S.; Herzig, C.; Limbeck, A.; Sistani, M.; Lugstein, A.; Barth, S. Solution-Based Low-Temperature Synthesis of Germanium Nanorods and Nanowires. *Monatsh. Chem.* **2018**, *149*, 1315−1320.
(528) Seifner, M. S.; Sistani, M.; Zivadinovic, I.; Bartmann, M. G.; Lugstein, A.; Barth, S. Drastic Changes in Material Composition and Electrical Properties of Gallium-Seeded Germanium Nanowires. *Cryst. Growth Des.* **2019**, *19* (5), 2531−2536.
(529) Dalpian, G. M.; Chelikowsky, J. R. Self-Purification in Semiconductor Nanocrystals. *Phys. Rev. Lett.* **2006**, *96* (22), 226802.
(530) Chan, T. L.; Tiago, M. L.; Kaxiras, E.; Chelikowsky, J. R. Size Limits on Doping Phosphorus into Silicon Nanocrystals. *Nano Lett.* **2008**, *8* (2), 596−600.
(531) Lu, X.; Korgel, B. A. A Single-Step Reaction for Silicon and Germanium Nanorods. *Chem. - Eur. J.* **2014**, *20* (20), 5874−5879.
(532) Flynn, G.; Stokes, K.; Ryan, K. M. Low Temperature Solution Synthesis of Silicon, Germanium and Si−Ge Axial Heterostructures in Nanorod and Nanowire Form. *Chem. Commun.* **2018**, *54* (45), 5728−5731.
(533) Mullane, E.; Geaney, H.; Ryan, K. M. Synthesis of Silicon−Germanium Axial Nanowire Heterostructures in a Solvent Vapor Growth System using Indium and Tin Catalysts. *Phys. Chem. Chem. Phys.* **2015**, *17* (10), 6919−6924.

https://dx.doi.org/10.1021/acs.chemmater.9b04471
Chem. Mater. 2020, 32, 2703−2741

(534) Flynn, G.; Ramasse, Q. M.; Ryan, K. M. Solvent Vapor Growth of Axial Heterostructure Nanowires with Multiple Alternating Segments of Silicon and Germanium. *Nano Lett.* **2016**, *16*, 374.
(535) Lu, X.; de la Mata, M.; Arbiol, J.; Korgel, B. A. Colloidal Silicon−Germanium Nanorod Heterostructures. *Chem. Mater.* **2017**, *29* (22), 9786−9792.
(536) Barth, S.; Seifner, M. S.; Bernardi, J. Microwave-Assisted Solution-Liquid-Solid Growth of $Ge_{1-x}Sn_x$ Nanowires with High Tin Content. *Chem. Commun.* **2015**, *51* (61), 12282−12285.
(537) Seifner, M. S.; Biegger, F.; Lugstein, A.; Bernardi, J.; Barth, S. Microwave-Assisted $Ge_{1-x}Sn_x$ Nanowire Synthesis: Precursor Species and Growth Regimes. *Chem. Mater.* **2015**, *27* (17), 6125−6130.
(538) Mukhopadhyay, B.; Sen, G.; Basu, R.; Mukhopadhyay, S.; Basu, P. K. Prediction of Large Enhancement of Electron Mobility in Direct Gap $Ge_{1-x}Sn_x$ Alloy. *Phys. Status Solidi B* **2017**, *254* (11), 1700244.
(539) Azrak, E.; Chen, W.; Moldovan, S.; Gao, S.; Duguay, S.; Pareige, P.; Roca i Cabarrocas, P. Growth of In-Plane $Ge_{1-x}Sn_x$ Nanowires with 22 at. % Sn Using a Solid−Liquid−Solid Mechanism. *J. Phys. Chem. C* **2018**, *122* (45), 26236−26242.
(540) Groiss, H.; Glaser, M.; Schatzl, M.; Brehm, M.; Gerthsen, D.; Roth, D.; Bauer, P.; Schäffler, F. Free-Running Sn Precipitates: an Efficient Phase Separation Mechanism for Metastable $Ge_{1-x}Sn_x$ Epilayers. *Sci. Rep.* **2017**, *7* (1), 16114.
(541) Qi, Z.; Sun, H.; Luo, M.; Jung, Y.; Nam, D. Strained Germanium Nanowire Optoelectronic Devices for Photonic-Integrated Circuits. *J. Phys.: Condens. Matter* **2018**, *30* (33), 334004.
(542) Meng, A. C.; Braun, M. R.; Wang, Y.; Fenrich, C. S.; Xue, M.; Diercks, D. R.; Gorman, B. P.; Richard, M. I.; Marshall, A. F.; Cai, W.; Harris, J. S.; McIntyre, P. C. Coupling of Coherent Misfit Strain and Composition Distributions in Core−Shell $Ge/Ge_{1-x}Sn_x$ Nanowire Light Emitters. *Materials Today Nano* **2019**, *5*, 100026.
(543) Ansari, L.; Fagas, G.; Colinge, J. P.; Greer, J. C. A Proposed Confinement Modulated Gap Nanowire Transistor Based on a Metal (Tin). *Nano Lett.* **2012**, *12* (5), 2222−7.
(544) Ansari, L.; Fagas, G.; Greer, J. C. *Tin Nanowire Field Effect Transistor*; IEEE: 2012, 294−297.
(545) Ansari, L.; Fagas, G.; Greer, J. C. Semi-Metal Nanowire Transistors from First Principle Calculations. *ECS Trans.* **2013**, *53* (1), 259−267.
(546) Ansari, L.; Fagas, G.; Greer, J. C. Strain Induced Effects on Electronic Structure of Semi-Metallic and Semiconducting Tin Nanowires. *Appl. Phys. Lett.* **2014**, *105* (12), 123105.
(547) Ansari, L.; Fagas, G.; Gity, F.; Greer, J. C. A sub kBT/q Semimetal Nanowire Field Effect Transistor. *Appl. Phys. Lett.* **2016**, *109* (6), 063108.
(548) Sanchez-Soares, A.; Greer, J. C. A Semimetal Nanowire Rectifier: Balancing Quantum Confinement and Surface Electronegativity. *Nano Lett.* **2016**, *16* (12), 7639−7644.
(549) Sanchez-Soares, A.; O'Donnell, C.; Greer, J. C. Electronic Structure Tuning via Surface Modification in Semimetallic Nanowires. *Phys. Rev. B: Condens. Matter Mater. Phys.* **2016**, *94* (23), 235442.
(550) Gity, F.; Ansari, L.; König, C.; Verni, G. A.; Holmes, J. D.; Long, B.; Lanius, M.; Schüffelgen, P.; Mussler, G.; Grützmacher, D.; Greer, J. C. Metal-Semimetal Schottky Diode Relying on Quantum Confinement. *Microelectron. Eng.* **2018**, *195*, 21−25.
(551) Moontragoon, P.; Vukmirović, N.; Ikonić, Z.; Harrison, P. Electronic Structure and Optical Properties of Sn and SnGe Quantum Dots. *J. Appl. Phys.* **2008**, *103* (10), 103712.
(552) Allan, G.; Delerue, C. Optimization of Carrier Multiplication for more Effcient Solar Cells: the Case of Sn Quantum Dots. *ACS Nano* **2011**, *5* (9), 7318−23.
(553) Jensen, R. V. S.; Garm Pedersen, T.; Pedersen, K. Optical Properties and Size/Shape Dependence of α-Sn Nanocrystals by Tight Binding. *Phys. Status Solidi C* **2011**, *8* (3), 1002−1005.
(554) Kufner, S.; Furthmuller, J.; Matthes, L.; Bechstedt, F. Optical Absorption and Emission of Alpha-Sn Nanocrystals from First Principles. *Nanotechnology* **2013**, *24* (40), 405702.
(555) Küfner, S.; Furthmüller, J.; Matthes, L.; Fitzner, M.; Bechstedt, F. Structural and Electronic Properties of α-Tin Nanocrystals from First Principles. *Phys. Rev. B: Condens. Matter Mater. Phys.* **2013**, *87* (23), 235307.
(556) Fyhn, M. F.; Chevallier, J.; Larsen, A. N.; Feidenhans'l, R.; Seibt, M. α-Sn and β-Sn Precipitates in Annealed Epitaxial $Si_{0.95}Sn_{0.05}$. *Phys. Rev. B: Condens. Matter Mater. Phys.* **1999**, *60* (8), 5770−5777.
(557) Karim, A.; Hansson, G. V.; Ni, W. X.; Holtz, P. O.; Larsson, M.; Atwater, H. A. Photoluminescence Studies of Sn Quantum Dots in Si Grown by MBE. *Opt. Mater.* **2005**, *27* (5), 836−840.
(558) Roesgaard, S.; Chevallier, J.; Gaiduk, P. I.; Hansen, J. L.; Jensen, P. B.; Larsen, A. N.; Svane, A.; Balling, P.; Julsgaard, B. Light Emission From Silicon with Tin-Containing Nanocrystals. *AIP Adv.* **2015**, *5* (7), 077114.
(559) Roesgaard, S.; Talbot, E.; Hatzoglou, C.; Hansen, J. L.; Julsgaard, B. Structural Characterization of Sn Nanocrystals Embedded in Silicon by Atomic Probe Tomography. *Mater. Res. Express* **2019**, *6* (6), 065005.
(560) Huang, S.; Cho, E.-C.; Conibeer, G.; Green, M. A.; Bellet, D.; Bellet-Amalric, E.; Cheng, S. Fabrication and Characterization of Tin-Based Nanocrystals. *J. Appl. Phys.* **2007**, *102* (11), 114304.
(561) Haq, A. U.; Askari, S.; McLister, A.; Rawlinson, S.; Davis, J.; Chakrabarti, S.; Svrcek, V.; Maguire, P.; Papakonstantinou, P.; Mariotti, D. Size-Dependent Stability of Ultra-Small α-/β-Phase Tin Nanocrystals Synthesized by Microplasma. *Nat. Commun.* **2019**, *10* (1), 817.
(562) Beaulieu, L. Y.; Hewitt, K. C.; Turner, R. L.; Bonakdarpour, A.; Abdo, A. A.; Christensen, L.; Eberman, K. W.; Krause, L. J.; Dahn, J. R. The Electrochemical Reaction of Li with Amorphous Si-Sn Alloys. *J. Electrochem. Soc.* **2003**, *150* (2), A149.
(563) Tamura, N.; Ohshita, R.; Fujimoto, M.; Kamino, M.; Fujitani, S. Advanced Structures in Electrodeposited Tin Base Negative Electrodes for Lithium Secondary Batteries. *J. Electrochem. Soc.* **2003**, *150* (6), A679.
(564) Park, C. M.; Kim, J. H.; Kim, H.; Sohn, H. J. Li-Alloy Based Anode Materials for Li Secondary Batteries. *Chem. Soc. Rev.* **2010**, *39* (8), 3115−41.
(565) Xu, L.; Kim, C.; Shukla, A. K.; Dong, A.; Mattox, T. M.; Milliron, D. J.; Cabana, J. Monodisperse Sn Nanocrystals as a Platform for the Study of Mechanical Damage During Electrochemical Reactions with Li. *Nano Lett.* **2013**, *13* (4), 1800−5.
(566) Oehl, N.; Hardenberg, L.; Knipper, M.; Kolny-Olesiak, J.; Parisi, J.; Plaggenborg, T. Critical Size for the β- to α-Transformation in Tin Nanoparticles After Lithium Insertion and Extraction. *CrystEngComm* **2015**, *17* (19), 3695−3700.
(567) Wang, B.; Yang, Y. H.; Yang, G. W. Growth Mechanisms of SnO_2/Sn Nanocables. *Nanotechnology* **2006**, *17* (18), 4682−8.
(568) Farrow, R. F. C.; Robertson, D. S.; Williams, G. M.; Cullis, A. G.; Jones, G. R.; Young, I. M.; Dennis, P. N. J. The Growth of Metastable, Heteroepitaxial Films of α-Sn by Metal Beam Epitaxy. *J. Cryst. Growth* **1981**, *54* (3), 507−518.
(569) Mason, B. F.; Williams, B. R. Growth and Annealing Behaviour of α-Sn on InSb(001) Measured by LEED and He Atom Scattering. *Surf. Sci.* **1992**, *262* (1−2), 169−179.
(570) Styrkas, A. D. Mechanisms of the Allotropic Transition of Sn. *Inorg. Mater.* **2003**, *39* (8), 806−810.
(571) Maliakkal, C. B.; Martensson, E. K.; Tornberg, M. U.; Jacobsson, D.; Persson, A. R.; Johansson, J.; Wallenberg, L. R.; Dick, K. A. Independent Control of Nucleation and Layer Growth in Nanowires. *ACS Nano* **2020**, DOI: 10.1021/acsnano.9b09816.
(572) Panciera, F.; Baraissov, Z.; Patriarche, G.; Dubrovskii, V. G.; Glas, F.; Travers, L.; Mirsaidov, U.; Harmand, J. C. Phase Selection in Self-catalyzed GaAs Nanowires. *Nano Lett.* **2020**, *20*, 1669−1675.
(573) Cheek, Q.; Fahrenkrug, E.; Hlynchuk, S.; Alsem, D. H.; Salmon, N. J.; Maldonado, S. In Situ Transmission Electron Microscopy Measurements of Ge Nanowire Synthesis with Liquid Metal Nanodroplets in Water. *ACS Nano* **2020**, *14* (3), 2869−2879.
(574) Wang, Z. L. Characterization of Nanophase Materials. *Part. Part. Syst. Charact.* **2001**, *18* (3), 142.

(575) Sluydts, M.; Pieters, M.; Vanhellemont, J.; Van Speybroeck, V.; Cottenier, S. High-Throughput Screening of Extrinsic Point Defect Properties in Si and Ge: Database and Applications. *Chem. Mater.* **2017**, *29* (3), 975−984.
(576) Pilania, G.; Wang, C.; Jiang, X.; Rajasekaran, S.; Ramprasad, R. Accelerating Materials Property Predictions using Machine Learning. *Sci. Rep.* **2013**, *3*, 2810.
(577) Kalinin, S. V.; Sumpter, B. G.; Archibald, R. K. Big-Deep-Smart Data in Imaging for Guiding Materials Design. *Nat. Mater.* **2015**, *14* (10), 973−80.
(578) Schmidt, J.; Shi, J.; Borlido, P.; Chen, L.; Botti, S.; Marques, M. A. L. Predicting the Thermodynamic Stability of Solids Combining Density Functional Theory and Machine Learning. *Chem. Mater.* **2017**, *29* (12), 5090−5103.
(579) Stanev, V.; Oses, C.; Kusne, A. G.; Rodriguez, E.; Paglione, J.; Curtarolo, S.; Takeuchi, I. Machine Learning Modeling of Superconducting Critical Temperature. *npj Computational Materials* **2018**, *4* (1), 29.
(580) Schmidt, J.; Marques, M. R. G.; Botti, S.; Marques, M. A. L. Recent Advances and Applications of Machine Learning in Solid-State Materials Science. *npj Computational Materials* **2019**, *5* (1), 83.
(581) Atabaki, A. H.; Moazeni, S.; Pavanello, F.; Gevorgyan, H.; Notaros, J.; Alloatti, L.; Wade, M. T.; Sun, C.; Kruger, S. A.; Meng, H.; Al Qubaisi, K.; Wang, I.; Zhang, B.; Khilo, A.; Baiocco, C. V.; Popović, M. A.; Stojanović, V. M.; Ram, R. J. Integrating Photonics with Silicon Nanoelectronics for the Next Generation of Systems on a Chip. *Nature* **2018**, *556* (7701), 349−354.
(582) Soref, R.; Buca, D.; Yu, S.-Q. Group IV Photonics: Driving Integrated Optoelectronics. *Opt. Photonics News* **2016**, *27* (1), 32−39.
(583) Vukajlovic-Plestina, J.; Kim, W.; Ghisalberti, L.; Varnavides, G.; Tütüncuoglu, G.; Potts, H.; Friedl, M.; Güniat, L.; Carter, W. C.; Dubrovskii, V. G.; Fontcuberta i Morral, A. Fundamental Aspects to Localize Self-Catalyzed III-V Nanowires on Silicon. *Nat. Commun.* **2019**, *10* (1), 869.
(584) Güniat, L.; Martí-Sánchez, S.; Garcia, O.; Boscardin, M.; Vindice, D.; Tappy, N.; Friedl, M.; Kim, W.; Zamani, M.; Francaviglia, L.; Balgarkashi, A.; Leran, J.-B.; Arbiol, J.; Fontcuberta i Morral, A. III−V Integration on Si(100): Vertical Nanospades. *ACS Nano* **2019**, *13* (5), 5833−5840.
(585) Naik, G. V.; Shalaev, V. M.; Boltasseva, A. Alternative Plasmonic Materials: Beyond Gold and Silver. *Adv. Mater.* **2013**, *25* (24), 3264−94.
(586) Ozbay, E. Plasmonics: Merging Photonics and Electronics at Nanoscale Dimensions. *Science* **2006**, *311* (5758), 189−93.
(587) Bhattacharjee, S.; Rietjens, I. M.; Singh, M. P.; Atkins, T. M.; Purkait, T. K.; Xu, Z.; Regli, S.; Shukaliak, A.; Clark, R. J.; Mitchell, B. S.; Alink, G. M.; Marcelis, A. T.; Fink, M. J.; Veinot, J. G.; Kauzlarich, S. M.; Zuilhof, H. Cytotoxicity of Surface-Functionalized Silicon and Germanium Nanoparticles: the Dominant Role of Surface Charges. *Nanoscale* **2013**, *5* (11), 4870−83.
(588) Hemmer, E.; Benayas, A.; Légaré, F.; Vetrone, F. Exploiting the Biological Windows: Current Perspectives on Fluorescent Bioprobes Emitting Above 1000 nm. *Nanoscale Horizons* **2016**, *1* (3), 168−184.
(589) Vaughn, D. D., II; Schaak, R. E. Synthesis, Properties and Applications of Colloidal Germanium and Germanium-Based Nanomaterials. *Chem. Soc. Rev.* **2013**, *42* (7), 2861−2879.
(590) Jennings, L. E.; Long, N. J. 'Two is Better Than One'–Probes for Dual-Modality Molecular Imaging. *Chem. Commun. (Cambridge, U. K.)* **2009**, No. 24, 3511−24.
(591) Cheon, J.; Lee, J. H. Synergistically Integrated Nanoparticles as Multimodal Probes for Nanobiotechnology. *Acc. Chem. Res.* **2008**, *41* (12), 1630−40.
(592) Salata, O. V. Applications of Nanoparticles in Biology and Medicine. *J. Nanobiotechnol.* **2004**, *2* (1), 3.
(593) Baraban, L.; Ibarlucea, B.; Baek, E.; Cuniberti, G. Hybrid Silicon Nanowire Devices and Their Functional Diversity. *Advanced Science* **2019**, *6* (15), 1900522.
(594) Ambhorkar, P.; Wang, Z.; Ko, H.; Lee, S.; Koo, K.-i.; Kim, K.; Cho, D.-i. Nanowire-Based Biosensors: From Growth to Applications. *Micromachines* **2018**, *9* (12), 679.
(595) Zhang, A.; Lieber, C. M. Nano-Bioelectronics. *Chem. Rev.* **2016**, *116* (1), 215−257.
(596) Tian, B.; Lieber, C. M. Nanowired Bioelectric Interfaces. *Chem. Rev.* **2019**, *119* (15), 9136−9152.

https://dx.doi.org/10.1021/acs.chemmater.9b04471
Chem. Mater. 2020, 32, 2703−2741